Doctoral Dissertation
Doctoral Program in Physics (38th Cycle)

A printable Organic Electrochemical Transistor on paper for biochemical sensing

Martina Cicolini
* * * * * *

Supervisors:
Prof. Francesca Frascella
Dr. Simone Luigi Marasso
Dr. Bruno Torre

Politecnico di Torino
April, 2026

This doctoral thesis was written at the end of the doctoral program funded by the PNRR, Mission 4, component 2 "*Dalla Ricerca all'Impresa*" – Investment 3.3 "*Introduzione di dottorati innovativi che rispondono ai fabbisogni di innovazione delle imprese e promuovono l'assunzione dei ricercatori dalle imprese*", through Ministerial Decree No. 352 of April 9, 2022.

Summary

Cellulose-based materials hold significant promise as substrates for point-of-care diagnostic devices. Among them, lateral flow assays (LFAs) owe their widespread success to their ease of use, portability, and affordability. However, their limited sensitivity and qualitative output still represent important drawbacks for broader analytical applications.

In response to the growing need for rapid and reliable diagnostic and monitoring tools, Organic Electrochemical Transistors (OECTs) have gained attention as powerful devices for biosensing applications because of their high sensitivity, low operating voltage, and compatibility with biological environments.

PEDOT:PSS is one of the most widely employed organic mixed ionic-electronic conductors in OECTs. Its broad use originates from its solution processability, biocompatibility, and high tunability, which make it compatible with a wide range of deposition techniques and device architectures. Continuous advances in additive manufacturing are making the fabrication of high-performance organic electronic devices increasingly accessible by reducing processing steps, lowering production costs, and enabling deposition on unconventional substrates such as paper, plastics, and flexible supports. These aspects are particularly relevant for diagnostic and point-of-care (POC) applications, where low fabrication cost must be combined with high sensitivity, reliability, and scalable production.

This thesis investigates how different printing techniques influence the morphology, structural organization, and electrical performance of PEDOT:PSS films. *In situ* Raman spectroscopy was employed to monitor the evolution of PEDOT structure during OECT depending on different gating condition. Atomic force microscopy was used to compare films deposited by inkjet printing and aerosol jet printing, highlighting how differences in roughness, phase segregation, and nanoscale organization strongly affect the electrochemical performance of the devices.

With the aim of developing a printable, low cost OECT on paper for biochemical sensing, a commercial PCB printer was employed for the non-contact dispense printing of silver tracks and PEDOT:PSS channel, gate, and extended gate onto a nitrocellulose strip, a material commonly used in immunochromatographic lateral flow assays. Acting as a self-standing passive microfluidic platform, the cellulose substrate was designed to transport and interact with liquid samples while preserving a contamination-free region for the active electronic components. Within a dry area defined by a hydrophobic barrier, a solid-state

electrolyte (SSE) layer enables ionic communication between channel and gate. Outside this region, a PEDOT:PSS extended gate selectively interacts with the analyte carried by the liquid sample, preventing direct contamination of the channel and improving operational stability.

With a maximum transconductance of approximately 4 mS, the proposed system demonstrates the feasibility of integrating an easily manufacturable transistor into an affordable biochemical assay, providing quantitative information at the point-of-care site to complement and strengthen the conventional colorimetric response of LFAs. The sensing platform was validated through dopamine detection, achieving a limit of detection of 0.01 mM.

Overall, the results presented in this thesis highlight the potential of combining printed PEDOT:PSS electronics, scalable additive manufacturing, and paper-based microfluidics for the development of next-generation low-cost diagnostic technologies.

Contents

List of tables

List of figures

Chapter 1

1 Introduction

1.1 Research framework and objectives

In our ever more globalized world, mass testing constitutes a key strategy for controlling disease spreading. Nonetheless, Covid-19 pandemic has brought out how large-scale testing is not always compatible with the capacity of central laboratories of analysis. Point-of-care (POC) devices are powerful tools in the decentralization of diagnostic procedures, allowing to acquire results directly at the site of the sampling. Among them, lateral flow assays (LFAs) are commercially available POC diagnostic platforms based on cellulose, that despite their ease of use and low cost, present limitations in terms of sensitivity and signal readout. As the need for rapid and reliable diagnostic tools grows, Organic Electrochemical Transistors (OECTs) have emerged as highly sensitive sensors, characterized by low power consumption and great compatibility with biological environment. At the same time, the continuous progress of additive manufacturing techniques offers new opportunities for the fabrication of low-cost electronic devices through scalable, maskless, and efficient processes, providing an alternative to conventional microfabrication methods, which often require expensive facilities and complex multistep procedures.

Within this framework, the present thesis pursued two main and complementary objectives.

- The first objective was the characterization of printed organic conductive films, with particular focus on poly(3,4-ethylenedioxythiophene) polystyrene sulfonate (PEDOT:PSS) processed through different deposition techniques, with the aim of understanding how the fabrication method influences morphology, nanoscale organization, electrical behavior, and electrochemical response, in preparation for the optimization of printed

organic devices. The work included structural, spectroscopic, and electrical investigations of printed PEDOT:PSS films, employing atomic force microscopy and Raman spectroscopy, and including *in situ* measurements under device operation, comparing the effects on channel modulation of a bare gold gate and of a PEDOT:PSS-coated gate.

- The second objective was the development of a fully printable organic transistor on paper, conceived as a sensing platform that could be directly integrated into commercially relevant POC assays. The device was fabricated on a cellulose substrate and designed to exploit the intrinsic capillary transport properties of paper as a passive and self-sustained microfluidic system. In this architecture, liquid samples can flow through the porous membrane without external pumps, while a dedicated dry region protects the active electronic components from contamination and undesired interactions with the analyte. This separation between wet sensing areas and dry operating areas was introduced to preserve device stability while ensuring the sensing electrode interaction with the sample.

Overall, the thesis aims to demonstrate how the combination of printed organic electronics, paper microfluidics, and scalable manufacturing strategies can contribute to the development of affordable, portable, and high-performance diagnostic technologies.

1.2 Thesis outline

Part of the work on the OECT design and fabrication and on the gate electrode functionalization was conducted at the Integrated Center for Physics and Photonic Materials of the Technischen Universität Dresden (IAPP – TU Dresden), during a six-month research period. A nine-month collaboration with the company Informatica System s.r.l. led to the development of an integrated sensing platform on paper.

This work is divided into five main chapters, including this introduction (**Chapter 1**).

Chapter 2 will be dedicated to the outlining of the research background. The concept of Point-of-care device will be introduced, discussing strategies to achieve fluid management via microfluidic platforms and capillarity-driven devices. Then, the working principles of OECTs and their application as biosensors will be described, introducing organic semiconductors and their mixed ionic-electronic conduction. An overview of flexible materials employed as OECTs

substrates will be presented, introducing how paper can be a potential candidate for biosensors fabrication.

The **Chapter 3** will be dedicated to the characterization techniques of printed films of the active material poly(3,4-ethylenedioxythiophene) polystyrene sulfonate (PEDOT:PSS). Atomic force microscopy (AFM) will be adopted to investigate surface morphology depending on the deposition technique, and the analysis of *in situ*, *in operando* Raman spectra will support the study of the doping-dedoping mechanism.

The **Chapter 4** will focus on the engineering and fabrication process of a printable OECT on paper. The chosen substrate is nitrocellulose, an amine-rich paper commonly employed in biochemistry and in commercial rapid tests for its ability to immobilize biomolecules. Thanks to its porosity, cellulose can act as a microfluidic platform that doesn't need external pumps. The OECT components consist of printed silver electrodes and PEDOT:PSS channel and gate. Underneath an insulating layer that preserves the electrodes and the solid-state electrolyte (SSE) from the liquid phase, the porous substrate allows the capillarity-driven transportation of the analyte towards the sensing region. An extended gate constitutes the sensing region located in the hydrophilic area, where the liquid sample will be able to soak and interact with the sensing electrode.

Chapter 5 briefly describes potential future developments of this work, concluding with some final considerations.

Chapter 2

2 Research background

This chapter will be dedicated to the outlining of the scientific and technological background underlying the research activity developed in this thesis. It will first introduce the concept of point-of-care devices, highlighting their growing importance in decentralized healthcare, rapid diagnostics, and on-site analytical testing.

Subsequently, the chapter will discuss the main strategies adopted for fluid handling in miniaturized analytical platforms. In this context, microfluidic technologies will be presented as powerful tools for controlling small liquid volumes with high precision, enabling reduced reagent consumption and rapid analysis. Alongside conventional microfluidic systems, capillarity-driven platforms will also be examined.

The working principles of Organic Electrochemical Transistors will then be described, with emphasis on their operation mechanism. The role of organic semiconductors as active materials will be introduced, focusing on their ability to support mixed ionic-electronic conduction, which allows efficient coupling between ionic signals in the electrolyte and electronic currents in the device.

Finally, an overview of different strategies for biosensing using Organic Electrochemical Transistors will be provided, describing functionalization steps and techniques for the integration of sensors into microfluidic platforms.

2.1 Point-of-care diagnostic devices

2.1.1 Overview

The emergence and evolution of biosensors have played a pivotal role in decentralizing healthcare, bringing diagnostic testing closer to the patient. As technological advancements continue to enhance analytical performance and reliability, many clinical analyses are no longer confined to laboratories but can be performed directly at the point of care.

In 2003, the World Health Organization (WHO) defined a set of criteria that could be applied to perform diagnostic tests at all levels of care, summarized by the acronym ASSURED: affordable, sensitive, specific, user-friendly, rapid, equipment-free, delivered[1]. These criteria have since guided the development of point-of-care tests, which aim to be widely affordable, accessible, and accurate [2].

Point-of-care (POC) diagnostic devices are compact, portable platforms that enable rapid, on-site detection of biomarkers or contaminants, enabling quick decision-making. In healthcare, POC biosensors have been shown to accelerate diagnosis and treatment, reducing hospital stays, and lowering costs[3–5]. In agriculture and livestock management, on-farm POC diagnostics help detect pesticides or infectious diseases, minimizing morbidity and economic losses while reducing the misuse of antibiotics[6–8]. Similarly, in food safety, POC platforms such as paper-based assays and lab-on-chip systems allow for real-time screening of contaminants, allergens, and toxins throughout the supply chain, enabling the early detection of irregular batches and preventing further contamination throughout the production chain[9,10]. Moreover, these solutions are critical in low- and middle-income settings, where access to laboratory infrastructure is limited or health services are insufficient.

Overall, the introduction of POC diagnostics may enable affordable, decentralized, and fast testing that can control disease outbreaks and guide effective treatment strategies, making health and food systems equitable and responsive.

2.1.2 Sensors for diagnostic applications

A **chemical sensor** can be defined as an analytical device capable of producing a measurable signal correlated to the concentration of a target chemical species. Building upon this concept, a biosensor integrates a biological recognition element with a transducer to detect specific analytes, so that the consequent biological interaction or catalytic event is converted into a quantifiable electrical, optical, or mechanical signal. These concepts, which emerged during the first decades of the 1900s, already reflected an urge for increased autonomy, speed, and decentralization of chemical assays and diagnostic tools.

One of the earliest documented references to the concept of decentralized, rapid diagnostic testing appears in a 1945 article by R. M. Tovar, who described a bedside agglutination test for the rapid diagnosis of tularemia, an infectious bacterial disease, based on mixing a concentrated suspension of antigen with whole blood obtained from a finger puncture[11]. In the years that followed, various studies have reported the development of **bedside diagnostic tests**, mainly consisting of agglutination assays and body fluids evaluations, highlighting a growing demand for quick testing performed near the patient[12–18]. In the

early 1980s, Dr. Gerald Kost is often credited with coining the term "point-of-care testing" while performing real-time biosensor measurements of ionized calcium in whole blood at the patient's side in operating rooms, demonstrating the benefit of immediate feedback in critical care settings[19]. Since then, the terms "point-of-care" (POC) and "point-of-need" occurrence in the scientific literature progressively increased, and interest in POC diagnostics has continued to expand, driven by the need for faster clinical decision-making and broader access to healthcare (Figure 2.1).

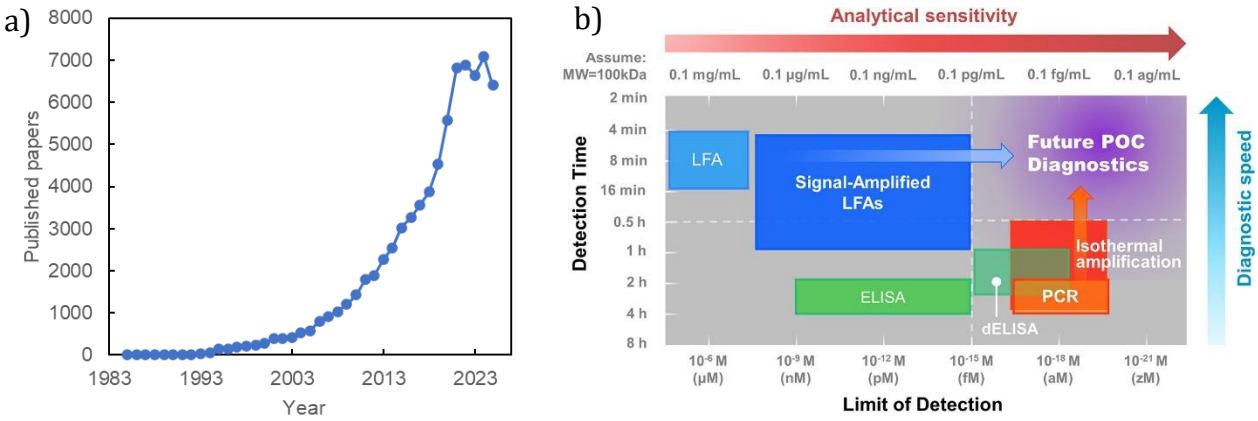

Figure 2.1 Evolution of point-of-care research and development by number of publications (Source: Scopus, September 2025). b) Comparison between different diagnostic strategies in terms of analytical sensitivity and diagnostic speed. Reprinted from [65].

In recent years, POC testing has been successfully adopted across a broad range of settings, also thanks to advances in electrochemical sensing, microfluidics, and immunoassays. Currently, POC solutions reduce the burden of repeated laboratory visits for chronic patients requiring frequent monitoring, such as individuals with diabetes, accelerating diagnostic feedback[20,21]. They are also increasingly employed in industrial settings to support routine safety monitoring, thereby reducing waste and costs associated with laboratory analysis[22]. In addition, POC devices are valuable tools not only in research and drug-discovery workflows, where rapid, low-volume analyses are essential, but also in many low- and middle-income countries, where limited access to centralized laboratories, the high cost or long turnaround time (from sample collection to communication of the result) of conventional diagnostics can significantly restrict access to healthcare[23–25].

For these reasons, early rapid POC devices consisted of cheap, capillarity-driven dipstick tests allowing equipment-free readouts. Over subsequent

decades, improvements in detection chemistry expanded the range of biomarkers measurable at point-of-care, while enhancing the sensitivity of the tests.

For their recognition element, POC platforms make extensive use of antibodies, whose high affinity and specificity support the capturing of analytes in most rapid diagnostic tests. Recent advancements in nucleic acid engineering allowed to introduce DNA probes and aptamers into POC tests, broadening the range of detectable biomarkers and enhancing target selectivity[26–30]. Enzymes are particularly employed in electrochemical POC devices, where their catalytic activity generates measurable reaction products, as exemplified by glucose oxidase-based glucose meters[31,32]. More recently, synthetic receptors such as molecularly imprinted polymers (MIPs) and engineered protein scaffolds have emerged as potential alternatives to biological components, providing improved stability under harsh environmental conditions[33–36].

The transducer plays a crucial role in the sensitivity of the sensing system. Indeed, the **transduction element** converts the energy of the biorecognition events into a qualitative or quantitative output, according to the chosen technique:

- **electrochemical transduction** involves the presence of enzymes able to catalyze redox reactions; applying different operational strategies, like amperometric, potentiometric, and impedimetric modes, it allows to achieve high sensitivity with low power consumption.
- depending on the device architecture, **electrical transduction** allows to finely detect biological interactions via changes in conductivity or capacitance of the electrodes.
- fluorescence, chemiluminescence, or Raman scattering are **optical transduction** strategies that enable detection with high specificity through appropriate optical readers.

Overall, the choice of the technologies at the base of each POC solution must balance miniaturization, cost, ease-of-use, and sensitivity. The ongoing innovations in nanomaterials, printed electronics, and microfluidics have enabled enhanced sensitivity and multiplexing capability, pushing POC testing toward more demanding diagnostic applications.

2.1.3 Microfluidic platforms

A significant challenge in the development of POC diagnostic devices involves managing liquid-based samples. Ensuring precise control over fluid dynamics is essential for delivering reliable and consistent results and minimizing sample

volume. For these reasons, microfluidic platforms have been drawing attention in many fields of applications, such as environmental monitoring, health management, and medical diagnosis[28,37–40].

Microfluidic devices rely on channels with dimensions from tens to hundreds of micrometers, where fluid transport adheres to laminar flow dynamics due to the low Reynolds number[37,41,42]. The suppression of turbulence and the use of minimal fluid volumes reduce operational costs compared to standard laboratory analysis techniques, while reproducibility and operational speed benefit from the precise and systematic control over fluid flow. When microfluidic platforms are integrated with analytical devices, they can be identified as **"lab-on-a-chip" (LoC)**, supporting high-throughput testing, batch processing, and control over the experimental reaction[43–45]. In view of these advantages, microfluidic devices are important enabling technologies for POC applications.

Polydimethylsiloxane (PDMS) is a well-established material for microfluidics fabrication. Consisting of a silicon-based organic elastomer composed of repeating Si-O units with methyl side groups, PDMS has been heavily employed in biomedical research thanks to its biocompatibility, chemical inertness, gas permeability, and optical transparency, which makes it compatible with optical detection techniques[37]. Its elasticity allows for valving and actuation, resulting in precise sample delivery and possibility of applying mechanical stimuli through liquid flow control[46]. PDMS mechanical properties also allow for easy fabrication procedures, that typically consist of pre-polymer casting onto a mold, followed by thermal curing, and peeling off after crosslinking. The molds are generally produced through photolithography, and the final microfluidic device is then obtained through micro-replica molding, by casting PDMS onto the master pattern. The cured PDMS structures are bonded to glass substrates or to additional PDMS layers patterned with complementary microchannels. More recently, alternative fabrication strategies have been explored for the rapid production of master molds used in microfluidic device fabrication. Recent advances in additive manufacturing technologies, such as fused deposition modeling (FDM), stereolithography (SLA), and PolyJet printing, have enabled the **rapid prototyping** of complex three-dimensional structures directly from computer-aided design (CAD) models[47,48]. These approaches allow the fabrication of molds with high design flexibility and significantly reduced process time compared to conventional photolithographic methods.

Despite their optical transparency and biocompatibility, PDMS-based platforms have relatively high cost and limited scalability for large-area production. Moreover, PDMS vapor permeability implies risks of early evaporation of the sample, due to the small volume handled by each device. In recent years, alternative substrates have been explored to overcome these limitations, and

thermoplastics such as PMMA and COC have been proposed for their robustness and compatibility with injection molding[42].

While thermoplastics offer great advantages in the industrialization scale up, efforts have been focusing lately on optimizing microfluidic solutions based on cost-sustainable and low-impact materials. Paper and cellulose-based platforms have gained particular attention due to their extremely low cost, capillary-driven fluid transport, and ease of functionalization. Cellulose-based microfluidics have the potential to eliminate the need for external pumps, reduce

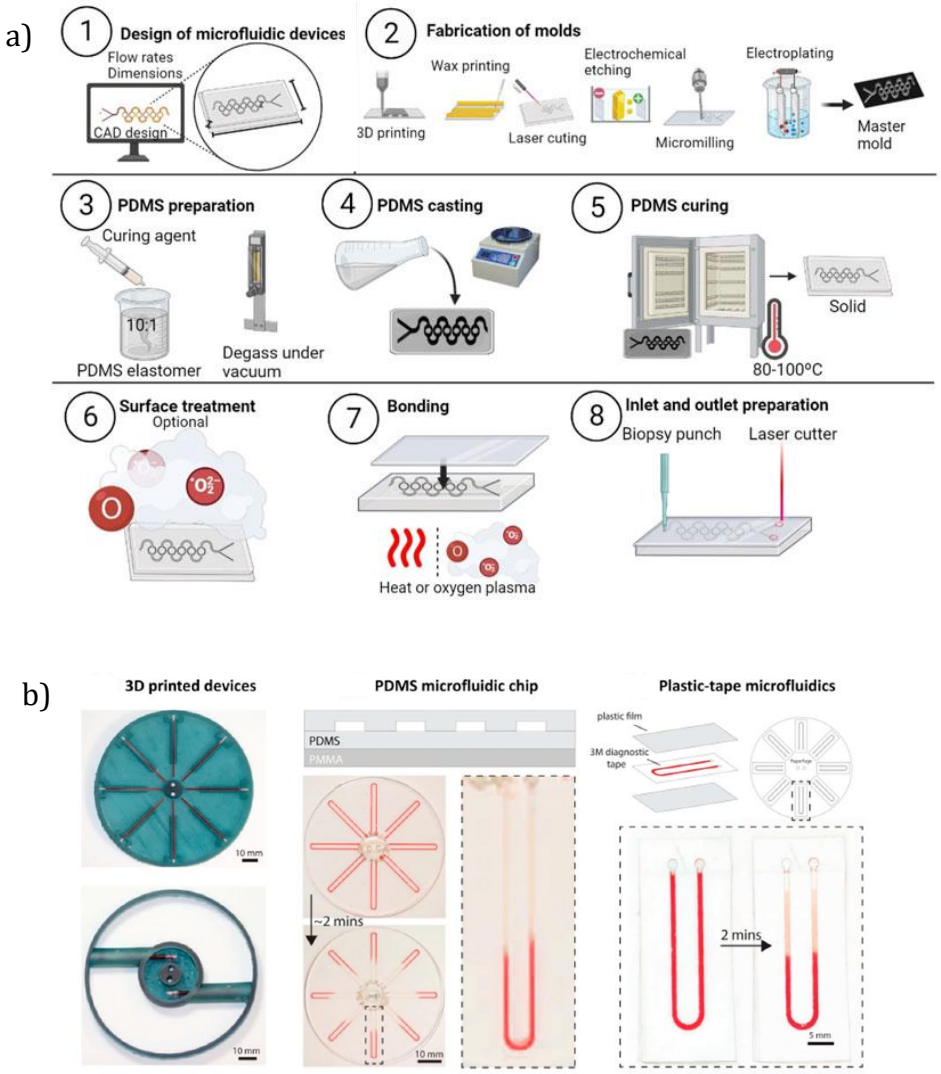

Figure 2.2 a) Fabrication process of PDMS microfluidic devices via soft lithography. Reprinted with permission from [264]. b) Types of handheld microfluidic centrifuge, useful for preparation of blood samples and separation of its solid and liquid components[39]. Shown in order: handheld microfluidic centrifuge made with 3D printing technology; PDMS handheld microfluidic centrifuge; plastic handheld microfluidic centrifuge [39,265]

fabrication complexity, and offer sustainable and disposable sensor formats[39,49].

2.1.4 Paper-based devices

Paper has been employed as a substrate for capillary-driven tests since the early development of POC diagnostic tools [15,17,50]. Although cellulose became the leading material for POC tests in the 1970s thanks to LFAs, its prominence was partly overshadowed in the following decades by advances in manufacturing technologies and the emergence of new materials that attracted increasing attention for sensing applications. The COVID-19 pandemic renewed interest in cellulose-based diagnostics: the need for large-scale, rapid testing to reduce hospital burden and monitor viral transmission highlighted the value of LFAs as accessible tools for decentralized diagnosis. In this context, cellulose has been reappraised as a promising material for lightweight, sustainable, and cost-effective diagnostic devices.

Cellulose is the most abundant biopolymer on earth[51]. It is a water-insoluble polysaccharide (Figure 2.3) found in plants cell walls and in other organisms, such as fungi, bacteria, and some marine invertebrates, forming microfibrils with great mechanical properties and chemical stability[52]. Cellulose is characterized by a microporous architecture and exceptional hydrophilicity that enable autonomous fluid transport. Non-toxic, biocompatible, renewable, and low-cost, cellulose constitutes a valid alternative to polymers based on fossil fuels[52].

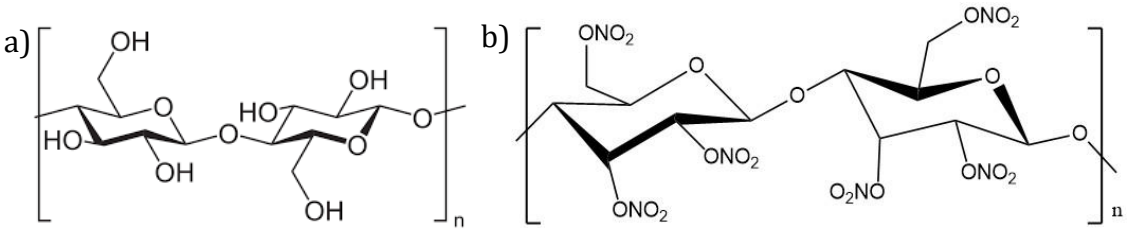

Figure 2.3 Schematic representation of the structure of (a) cellulose and (b) nitrocellulose.

Nitrocellulose, or cellulose nitrate, is the term that identifies the group of nitric esters of cellulose. It consists in a chemically modified form of cellulose, where nitro groups replace hydroxyl groups after direct reaction of cellulose with HNO_3, resulting in various degrees of substitution, expressed as degree of nitration (DoN) (Figure 2.3) [53]. The synthesis parameters, like temperature,

humidity and evaporation speed, influence porosity and pore size, which are tunable according to the application. Nitrocellulose is a well-established material in biochemistry and has been used as a blotting membrane for the immobilization and transfer of biomolecules since the 1960s, owing to its three-dimensional, wettable microporous structure[54]. Its application in Southern, Northern, and Western blotting laid the foundation for its adoption in flow-based assays, as the membrane's ability to immobilize target-specific antibodies while supporting capillary-driven sample transport made it an ideal substrate for the widespread diffusion of LFAs[55].

2.1.4.1 Lateral Flow Assays (LFAs)

The first major commercial application of LFAs, or lateral flow tests (LFTs) was the urine-based pregnancy test, which became widely available around 1984 [56]. Over subsequent decades, LFAs have matured into a central diagnostic tool, gaining widespread use in clinical, veterinary, environmental and food safety settings, also thanks to its simple use and fast colorimetric readout.

Characterized by high shelf stability, commercial LFAs are constituted by four overlapping pads of cellulose of various grades of porosity: a sample pad, a conjugate pad, a nitrocellulose strip, and an absorbent pad, all placed on a plastic backing card[57]. Pad materials, reaction buffers, overlap between the pads, and travel distances are optimized to ensure that the flow travels across the whole strip at the proper rate, allowing the sample to interact properly with each component of the assay.

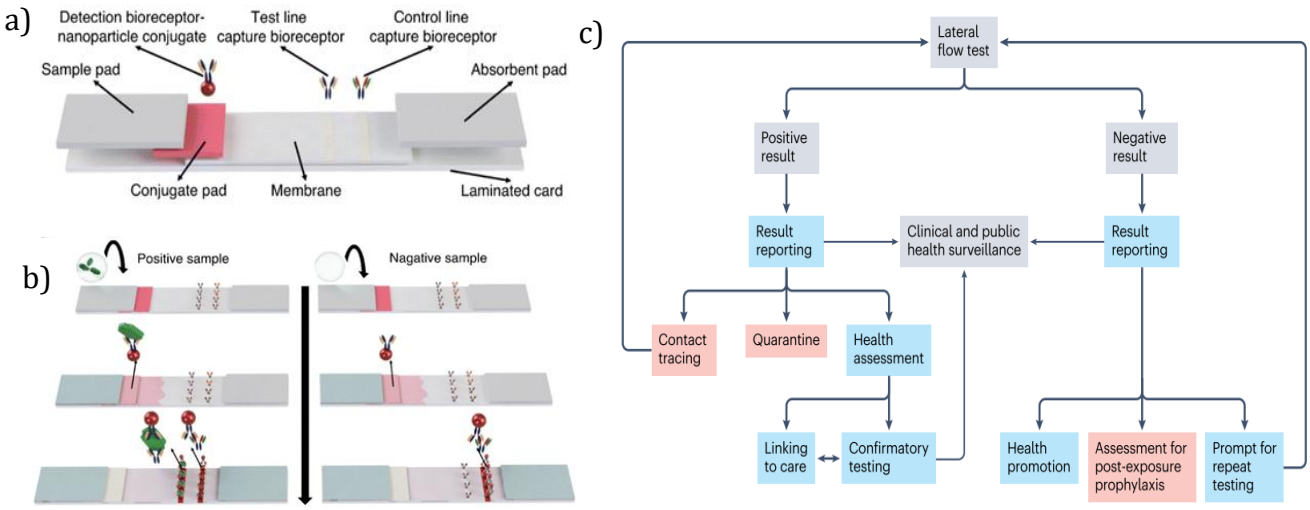

Figure 2.4 Schematic representation of the (a) structure and (b) running process of LFAs. Reprinted with permission from [266]. c) Schematic representation of clinical user journeys following a lateral flow test in a variety of settings. Reprinted with permission from [58].

The sample pad acts as the entry point and must rapidly accept and distribute the sample fluid, which so begins its path across the assay strip. The role of the conjugate pad is to retain dried gold nanoparticles (NPs) conjugated with a biorecognition element, usually antibodies, specific to the target analyte researched in the sample. Once the sample drop reaches and soaks the conjugate pad, the NPs are released in the liquid flow. If present, the analytes in the sample interact and bind to the antibodies on the NPs. At this point, the liquid travels across the nitrocellulose strip, the core of the assay, dragged by **capillarity**. The nitrocellulose strip hosts the test and control lines, constituted by two different types of antibodies; while the test line provides the diagnostic output, the control line serves as a checkbox for the correct execution of the assay. Lastly, the sample reaches the absorbent pad, which functions as a sponge and drives fluid through the end of the strip. By maintaining continuous wicking, the absorbent pad ensures complete sample migration and proper termination of the assay[58].

The **colorimetric signal** produced in 5-15 minutes from the sample dropping in correspondence of the two lines is based on the localized surface plasmon resonance (LSPR) phenomenon, which is the collective oscillation of the conductive electrons of the gold atoms triggered by incident electromagnetic waves, i.e., light[5,59]. When binding events happen at the test and control lines

between the conjugates on the gold NP and the antibodies on the nitrocellulose strip, NPs aggregate on the lines: the intensity of the color generated by LSPR is proportional to the number of NPs stuck on the line, that is correlated to the number of binding events and the amount of target molecules present in the sample.

The interpretation of the colorimetric output in LFAs is not always univocal, as test lines may appear faint or nearly invisible at low concentrations, especially for low-abundance biomarkers. **Limited sensitivity**, subjective visual assessment, and uncertainty in borderline results represent major weaknesses of conventional LFAs.

To address these limitations and enhance sensitivity, recent works have leveraged nanomaterials, optical labels, and alternative readout approaches [60–65]. Magnetic nanoparticles (MNPs) have been employed to preconcentrate analytes (Figure 2.5) and enhance signal intensity. By applying an external magnetic field, MNP-labeled targets can be accumulated at the test line, increasing local analyte density. In addition, magnetic detection offers low background noise, enabling high-contrast outputs. SERS (Surface Enhanced Raman Spectroscopy) tags, fluorescence labels and fluorescent nanoparticles (quantum dots, dye-doped silica nanoparticles) provide stronger, more stable signal compared to traditional gold NP, and allow quantitative reading when coupled with specific readers (Figure 2.5).

Nevertheless, each enhancement strategy carries drawbacks. Introduction of pre-concentration steps and use of specific nanomaterials increase assay complexity and cost. At the same time, highly sensitive detection methods often depend on bulky or costly equipment, which weakens the accessibility and simplicity that make LFAs attractive. Using smartphone cameras as detectors allows LFAs to become semi-quantitative and more accessible, reducing reliance on expensive readers, although inconsistency and unreliability may be introduced by variations in light conditions and camera performance[66,67].

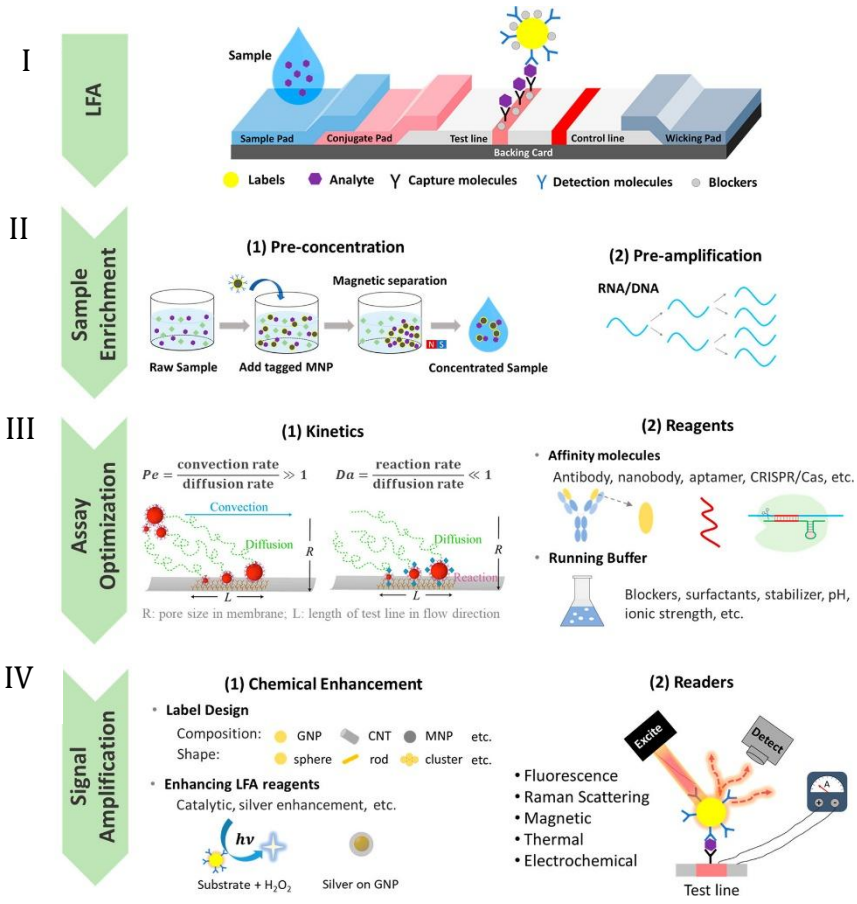

Figure 2.5 Summary of strategies to enhance sensitivity in LFAs. I) Structure and components of a LFA strip. II) The analyte can be pre-concentrated using magnetic NPs, for example, or pre-amplified via sample enrichment techniques. III) Optimization of assay kinetics is crucial in defining the test sensitivity since the interaction dynamics between the reagents and the strip influences the binding events at the test and control lines. IV) Label design, enhancing reagents and the use of specific readers for non-colorimetric detection mechanisms can contribute to the amplification of output signals. MNP: magnetic nanoparticle; GNP: gold nanoparticle; CNT: carbon nanotube. Reprint from [65].

Recently, research has been focusing on integrating analytical devices into LFAs, answering the need for high sensitivity without increasing the costs and complexity of the assay, which are often associated with the use of specific nanomaterials. **Electrochemical LFAs** (eLFAs) emerged as a practical solution to obtain sensitive and quantifiable results[31,32,68–70]. Electrochemical LFAs usually involve the integration of three electrodes on the assay strip, serving as working, reference, and counter electrode, printed or deposited along the strip. The

sensing mechanism relies on redox reactions occurring as the sample flows through the nitrocellulose pad, enabling electron transfer between the reaction products and the electrode surfaces: this transduced electrical signal is then measured to quantify target concentration. Despite its advantages in terms of sensitivity and quantification capabilities, electrochemical detection often requires supplemental reagents such as redox mediators and conductive tracks made of materials like gold, carbon, or platinum, which can increase fabrication cost and assay complexity.

2.1.4.2 Paperfluidics and papertronics

Because capillary flow is a passive phenomenon dependent on porous medium properties, like pore size distribution, tortuosity, and wettability, fluid transport can be inherently variable and difficult to control precisely. However, once paper substrates began to be successfully patterned to direct, confine, or separate fluid flow, they emerged as practical and robust alternatives to conventional PDMS-based microfluidic systems.

By adopting specific surface treatments, flow channels can be defined through hydrophobic barriers, allowing precise control of capillary-driven transport. Since the pioneering introduction of microfluidic **paper-based analytical devices (µPADs)** by Martinez *et al*. in 2007, wax printing became one of the most widely adopted methods for rapidly producing hydrophobic boundaries by depositing wax on paper[71]. However, the discontinuation of solid-ink printers induced researchers to explore alternative strategies to replicate or improve the barrier quality offered by wax-printed channels[72,73]. Koivunen *et al*. demonstrated the use of inkjet printing to obtain precise and digitally defined features with hydrophobic polymers[74]. Screen-printing of hydrophobic inks has been used to achieve thicker, more chemically robust barriers suitable for assays involving surfactants or organic solvents[75,76]. Other approaches such as laser ablation[4], parylene deposition[6], and silane-based surface modification[7] offer different advantages depending on the application, desired throughput, and required chemical stability.

Exploiting these fabrication strategies, paper-based microfluidic devices are especially attractive because they are low-cost, lightweight, disposable, and compatible with mass manufacture[77]. Considering these advantages, µPADs have been increasingly integrating not only fluid handling, but also electronic components, seeking to develop quantitative and objective POC platforms adherent to the ASSURE criteria. Early works coupled paper microfluidics with electrochemical detection via printed or laminated electrodes on paper[78–80]. Origami-style paper devices extended this idea by folding a single patterned sheet to implement multistep electrochemical detection[81–83]. Lately referred to as "**papertronics**", these architectures combine printed conductors, electrodes,

or transistors with paperfluidics, constituting high-performance sensing platforms that remain competitive in POC applications[84].

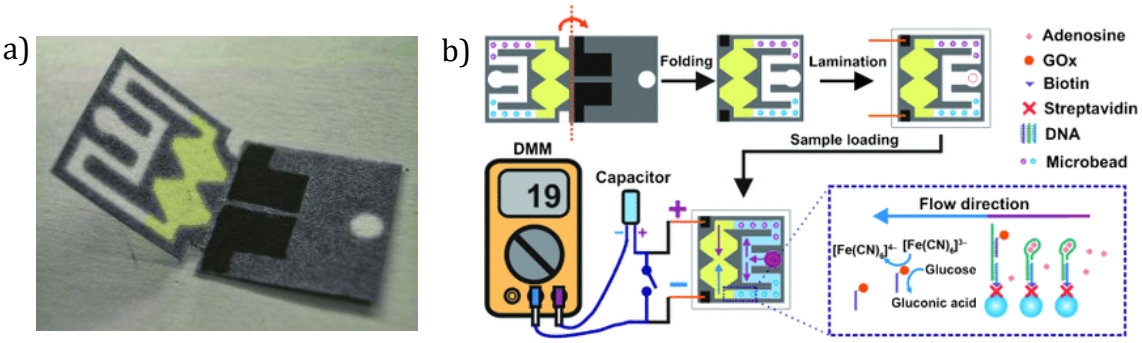

Figure 2.6 a) A paper-based electrochemical sensor for the detection of adenosine via immobilization of an enzyme on the fluidic channel, displaying an origami-like architecture. b) The device is printed on a piece of paper, which constitutes a self- standing microfluidic device thanks to the applied folds. Reprinted with permission from [82].

2.2 Organic Transistors

Until the late 1970s, polymers were widely assumed to be electrical insulators. Marking a pivotal shift in the understanding of organic materials, the work of Shirakawa, Heeger, and MacDiarmid demonstrated that certain conjugated polymers could exhibit metallic-level conductivity when appropriately doped[85].

The discovery of conducting polymers enabled the emergence of versatile, low-power, and highly sensitive alternatives to conventional inorganic semiconductor devices. Thanks to the versatility and chemical tunability of organic conductors, organic transistors can exhibit mechanical flexibility, good compatibility with soft and liquid environments, and potential for cost-effective and lightweight electronics, making them attractive components for chemical sensing, point-of-care diagnostics, electrochromic applications, neuromorphic devices, and logic circuits.

2.2.1 Organic conductors

After discovering that polyacetylene was able to conduct electricity when doped with halogens such as iodine, the collaborative work among Shirakawa,

MacDiarmid, and Heeger soon confirmed that the conductivity arose from the conjugated π-electron backbone of the polymer.

The term **conjugated polymers** refers to polymers characterized by a backbone with alternating single and double covalent bonds.

When carbon bonds with neighboring atoms, the atomic orbitals can combine to form new hybrid orbitals. Hybridization can involve different combinations of the one 2s and three 2p orbitals. When all four orbitals participate, four equivalent sp^3 **hybrid orbitals** are produced, which are oriented toward the vertices of a tetrahedral geometry, with mutual angles of approximately 109.5°, assuming a configuration characteristic of saturated carbon systems such as ethane. If the 2s orbital combines with only two of the 2p orbitals, typically 2px and 2py, three equivalent sp^2 hybrid orbitals are generated. These orbitals lie in a single plane and are separated by angles of 120°, while the remaining unhybridized 2pz orbital remains perpendicular to this plane, as found in unsaturated molecules such as ethene. Finally, hybridization between the 2s orbital and a single 2p orbital produces two sp hybrid orbitals aligned linearly at 180° with respect to each other. The two remaining p orbitals remain unhybridized and are available for π bonding, as observed in linear carbon systems and molecules containing triple bonds[86].

While the sp or sp^2 orbitals form σ bonds along the polymer backbone, the remaining non-hybridized 2p orbitals overlap to generate π and π* bonding and antibonding molecular orbitals, as approximated by the linear combination of atomic orbitals (LCAO) method.

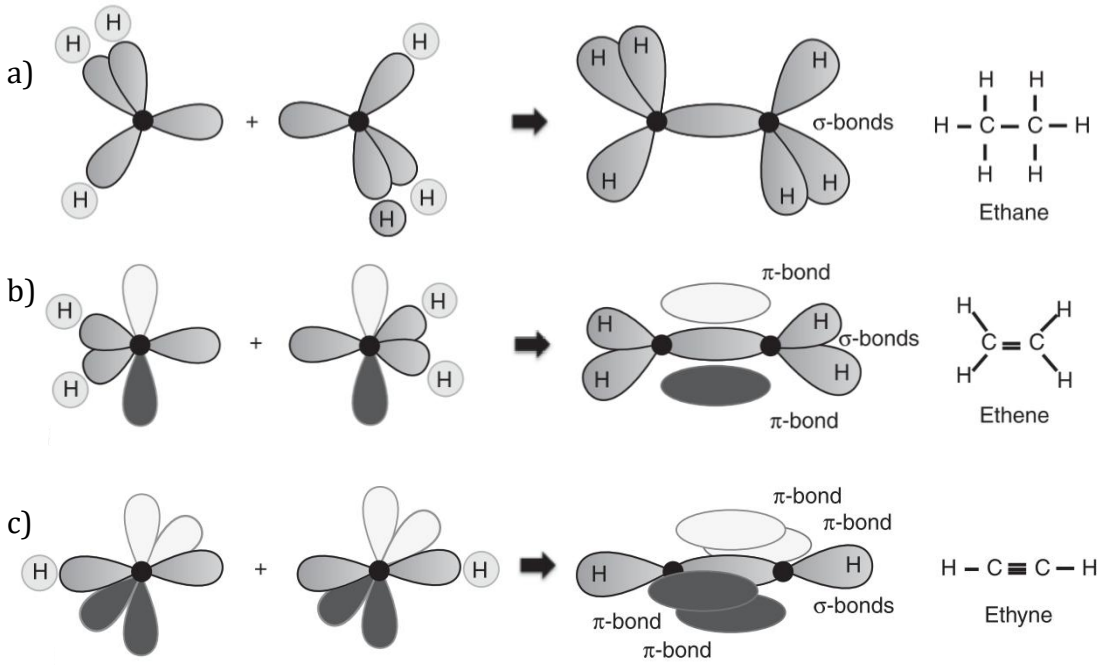

Figure 2.7 Schematic representation of molecular structures formed by carbon atoms with different hybridization states: (a) ethane, consisting of two sp^3-hybridized carbon atoms bonded to six hydrogen atoms; (b) ethene (ethylene), composed of two sp^2-hybridized carbon atoms bonded to four hydrogen atoms; and (c) ethyne (acetylene), formed by two sp-hybridized carbon atoms bonded to two hydrogen atoms. Reprinted with permission from [86].

Electrons occupy the available molecular orbitals starting from the lowest energy levels, such that the highest occupied molecular orbital (HOMO) and the lowest unoccupied molecular orbital (LUMO) are constituted by the π and π* orbitals, respectively. The energy separation between bonding and antibonding molecular orbitals is primarily governed by the interaction between the nuclei and the overlap of the participating atomic orbitals[86]. Since the overlap of the 2p unhybridized orbitals occurs farther from the nuclei, the resulting energy splitting between the π and π* orbitals is smaller than that between σ and σ* orbitals, **making conjugated polymers eligible for electron conduction**. This energy difference, known as the **HOMO-LUMO gap**, is analogous to the band gap in inorganic semiconductors.

The formed delocalized π-electron system extends perpendicular to the molecular plane across many repeating units, allowing intramolecular charge transport according to the entity of the band gap. Typical conjugated polymers exhibit band gaps between 1.5 and 3 eV, placing them in the semiconducting range [87].

In inorganic semiconductors and in highly ordered molecular crystals at sufficiently low temperatures, charge transport is dominated by band-like motion of charge carriers. In molecular crystals at temperatures above 0 K, however,

when intramolecular vibrations become comparable in magnitude to intermolecular motions, charge carriers are scattered at each site[88,89]. Under these conditions, lattice disorder and thermal vibrations perturb carrier motion, and transport can no longer be described by coherent band-like motion. Instead, charge carriers undergo incoherent, thermally assisted transitions between localized states. This process, also influenced by local electron-phonon interactions (vibronic coupling), is known as **hopping transport**. When coupling between electronic excitations and molecular vibrations become dominant, leading to polaronic effects associated with dynamic diagonal and off-diagonal disorder, charge transport occurs via a polaron-mediated mechanism. Instead, when static energetic disorder prevails, transport is primarily governed by disorder-controlled processes. In both cases, charge motion proceeds through thermally activated hopping between localized states rather than through coherent band-like transport[86].

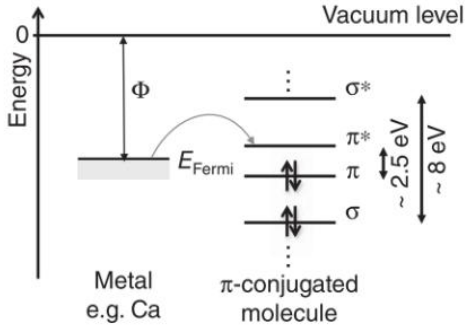

Figure 2.8 Schematic of typical energetic positions of the frontiers orbitals (HOMO and LUMO) in organic molecules relative to metal work functions. Reprinted with permission from [86].

2.2.1.1 Polaronic transport

In their pristine state, most conjugated polymers are only weakly conductive, as there are very few intrinsic charge carriers. Doping, which in conducting polymers can be referred to as electrochemical doping, implying oxidation or reduction and corresponding incorporation of counter ions to maintain charge neutrality[89], introduces mobile charge carriers and new energy states in the band gap. Acceptor doping (p-doping) removes electrons (oxidation), creating holes, while n-doping adds electrons (reduction), creating negative carriers. At the same time, ions from the dopant species enter the polymer matrix (e.g., ClO_4^-, PF_6^-, Na^+), stabilizing the newly formed charge carriers [89].

In contrast to inorganic materials, whose atoms are arranged in rigid, periodic lattices, polymers consist of **flexible macromolecular chains** held together by weak van der Waals interactions and electrostatic forces. As a result, the coupling of a charged molecule to the surrounding molecules alters the van der Waals interactions: doping induces localized distortions of the polymer backbone and electronic polarization, leading to the formation of polarons.

Polarons are hopping quasi-particles coupled with local lattice deformation, having charge e and spin ½.[89] Transport via inter-site polaron hopping is therefore associated with molecules distortion and environment reorganization, requiring a reorganization energy λ:

$$\lambda = \lambda_{innner} + \lambda_{outer} \tag{2.1}$$

where $\lambda_{inner} = \lambda_A + \lambda_B$ accounts for the intramolecular distortion of molecule A and B during the charge transfer process from A to B. In contrast, the outer reorganization energy λ_{outer} arises from intermolecular rearrangements and polarization effects. In rigid organic solids, charge transfer is primarily governed by intramolecular contributions, making λ_{inner} the dominant term, while in aqueous or highly polar media strong solvation leads to a larger environmental response, causing λ_{outer} to play a more significant role. The reorganization energy λ represents the change in potential energy associated with structural and environmental rearrangements when the system reaches its final configuration following charge transfer from molecule A to molecule B. The energy difference between the non-distorted molecule and the molecule distorted upon addition of a charge ($\lambda_{A,B}$) constitutes the polaron binding energy $E_{pol} = \lambda/2$ [86].

Charge transfer occurs through a thermally activated process, requiring the system to overcome an energy barrier of $\lambda/4$, at which the potential energy curves of the initial and final states intersect[86]. Under conditions of weak electronic coupling and when the characteristic phonon energies are small compared to the thermal energy, charge transport mediated by polarons can be described within a thermally activated hopping regime. In this limit, the polaron hopping rate is given by [90]:

$$k_{ET} = \frac{J^2}{\hbar}\sqrt{\frac{\pi}{2E_{pol}kT}}\,exp\left(-\frac{E_{pol}}{2kT}\right) \tag{2.2}$$

where J is the electronic transfer integral between neighboring sites, incorporating both the attempt frequency and the probability of successful charge transfer. From this hopping rate, the charge carrier mobility associated with polaronic transport can be derived as:

$$\mu_{pol} = \frac{ea^2J^2}{6\hbar(kT)^{3/2}}\sqrt{\frac{\pi}{2E_{pol}}}exp\left(-\frac{E_{pol}}{2kT}\right) \quad (2.3)$$

where a represents the distance between adjacent lattice sites. Expression 2.3 highlights the strong dependence on temperature and electron-phonon coupling strength of polaron transport. In highly ordered molecular crystals characterized by strong electron-phonon interactions, mobility dependance on temperature typically exhibits three different regimes. At low temperatures (below 300 K), charge carriers remain delocalized, and transport is dominated by band-like motion. In this regime, mobility decreases with increasing temperature as $\mu \propto T^{-n}$ due to enhanced phonon scattering. As the temperature increases, band transport progressively weakens while thermally activated hopping becomes relevant. This coexistence of transport mechanisms results in a minimum in the mobility curve, marking the crossover between band-like and hopping-dominated regimes. At higher temperatures, hopping transport dominates, and the mobility follows a characteristic temperature dependence approaching $\mu \propto T^{-3/2}$. In this high-temperature regime, thermal energy becomes sufficient to disrupt coherent polaron motion, and charge carriers experience frequent scattering by phonons, with consequent mobility decrease as lattice vibrations intensify.

Benzoid and quinoid configurations

The electronic structure of the backbone of aromatic conjugated polymers like polythiophenes and polyaniline can be found in two resonance forms: the benzoid (aromatic), which assumes a coil conformation and exhibits low conductivity, and the quinoid, which exhibits a linear structure with high conductivity[91]. In the neutral state, the benzoid form is energetically favored and the backbone shows bond-length alternation, with longer single bonds and shorter double bonds. Upon oxidation, the removal of an electron from the π-conjugated system destabilizes the aromatic structure locally. To accommodate the injected positive charge, the polymer backbone undergoes a local geometric relaxation, transitioning toward a quinoid-like structure and giving rise to a polaron. In this quinoid configuration, bond-length alternation is less pronounced, and the π-electron density becomes more delocalized along the chain. At higher doping levels, when two polarons are formed in proximity along the polymer chain, they can merge into a bipolaron, whose formation is associated with further reduction of bond-length alternation and leads to deeper electronic states within the band gap.

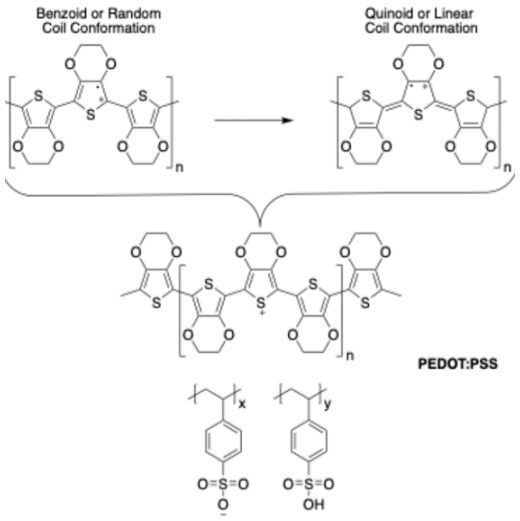

Figure 2.9 PEDOT:PSS benzoid and quinoid configurations. Reprint from [224].

2.2.1.2 Disorder-based transport

Most organic semiconductors relevant to the applications treated in this dissertation are noncrystalline, implying that the hopping transport happens between neighboring states that are spatially and energetically irregularly distributed, requiring different activation energies E_a, which reflect the energetic cost associated with molecular reorganization during charge transfer, for forward and backward hopping. The occupation probability of a site by a charge carrier in a disordered material can be described by a general master equation for hopping transport [92]:

$$\frac{\mathrm{d}p_i(t)}{\mathrm{d}t} = \sum_{j\neq i}\left[-w_{ij}p_i(t)\left(1-p_j(t)\right) + w_{ji}p_j(t)(1-p_i(t))\right] \qquad (2.4)$$

where $w_{ij,ji}$ are the hopping rate between different sites. The first term accounts for charge carriers leaving site i, while the second term describes incoming hops from neighboring sites. In the Miller-Abrahams model[93], the hopping rate includes an exponential decay with distance and an energetic selection rule: while hops toward energetically higher empty sites require thermal activation, hops toward lower-energy sites are always energetically allowed.

Charge transport occurs within a distribution of localized states whose energetic disorder is commonly described by a Gaussian density of states (DOS):

$$g(\epsilon) = \frac{1}{\sqrt{2\pi}\sigma} exp\left(-\frac{(\epsilon-\epsilon_0)^2}{2\sigma^2}\right) \qquad (2.5)$$

where the standard deviation σ is the width of the distribution and represents the disorder parameter[86]. At low carrier concentrations, a charge injected into the system at an arbitrary energy within the Gaussian DOS will preferentially hop toward sites of lower energy following Miller-Abrahams rates[86]. This process results in an energetic relaxation of the charge carrier toward the tail of the DOS. Over sufficiently long times, a quasi-equilibrium with mean energy $\epsilon_\infty = -\frac{\sigma^2}{kT}$ is established[86], characterized by a balance between downhill hops and thermally activated uphill hops. This relaxation leads to the formation of a Gaussian occupational density of states (ODOS) centered at ϵ_∞. Only a subset of states effectively contributes to conduction. Macroscopic charge transport happens when carriers are thermally promoted from deep occupied tail states to an energy region from which a network of energetically and spatially favorable hops becomes available, at the so-called transport energy, from which long-range hopping becomes more probable. In this regime, occupation probabilities are small, and Boltzmann statistics provide a good approximation. In the absence of an applied electric field, within the Gaussian disorder model, mobility depends on temperature as[90]:

$$\mu(T) = \mu_0 exp\left[-\left(\frac{2\sigma}{3kT}\right)^2\right] = \mu_0 exp\left[-\left(\frac{T_0}{T}\right)^2\right] \tag{2.6}$$

In realistic organic semiconductors, charge transport is often influenced by both static energetic disorder and polaronic effects arising from electron-phonon coupling. These two mechanisms can be considered simultaneously by introducing static disorder into a polaron-based hopping framework. In such models, the ratio between the disorder parameter σ and the polaron activation energy E_a reflects the contribution of disorder-dominated and polaron-dominated transport in the material, and mobility dependance on temperature, in the absence of an applied electric field, can be expressed as:

$$\mu \propto exp\left[-\frac{E_a}{kT}\right] - C\left(\frac{\sigma}{kT}\right)^2 \tag{2.7}$$

with C being a scaling parameter that increases with the ratio σ/Ea. Defining a critical temperature T_c by equating the energetic contributions of disorder and polaronic reorganization as:

$$kT_c = C\frac{\sigma^2}{E_a} \tag{2.8}$$

it can be observed that above T_c transport is governed by polaron dynamics and lattice reorganization effects, while below T_c static disorder dominates, and carrier motion is controlled by hopping through the disordered DOS.

In case of high carrier density, a significant fraction of available localized states becomes occupied, and the Pauli exclusion principle must be taken into account. Therefore, the occupation of electronic states follows a Fermi-Dirac distribution rather than a Boltzmann distribution, and a quasi-Fermi level is established at energy higher than ϵ_∞, filling progressively higher-energy states in the DOS. As a result, the average energy of occupied states increases, meaning that charge carriers reside closer to the transport energy, and the activation energy required for thermally assisted hopping is reduced, because carriers no longer need to be excited from deep tail states but instead hop from higher-energy states. As the activation barrier for hopping decreases, the hopping rate increases, leading to an enhancement of charge carrier mobility, as observed in the organic semiconductor channel in Field Effect Transistors (FETs) and Organic Electrochemical Transistors (OECTs).

Thanks to its flexibility, the polymer backbone can adopt various conformations and pack in semi-crystalline or amorphous domains. On a microscopic level, the π-π stacking between adjacent chains, mediated by overlapping p-orbitals and chain planarity, can facilitate interchain charge hopping (Figure 2.10 d) while crystallinity enhances intrachain hopping [94]. On the other hand, the grain boundaries of the different domains or crystallites act as defects and can trap charge carriers, reducing their mobility. By increasing the degree of crystallinity and the crystallites size and orientation, secondary dopants, also

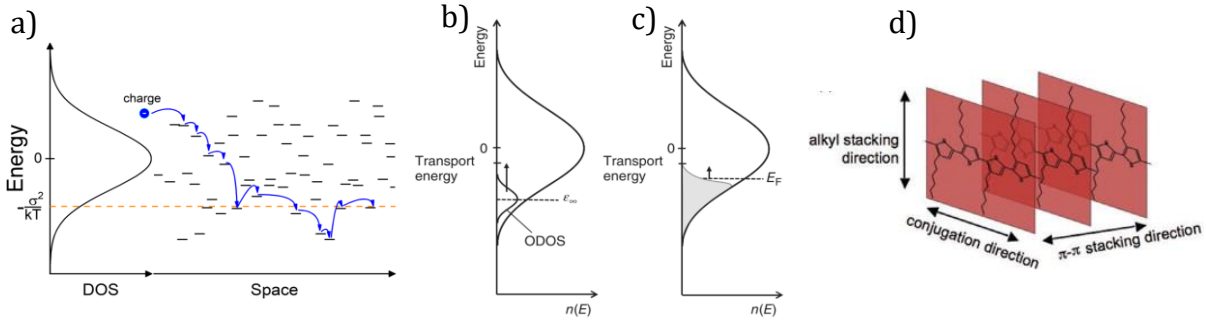

Figure 2.10 a) A Gaussian distribution with standard deviation σ describes the density of states of disordered semiconductors. b) Low carrier density regime, in which the activation energy necessary for charge transport depends on ϵ_∞. c) High carrier density regime, where the activation energy is reduced due to the arising of a quasi-Fermi level at $E > \epsilon_\infty$. (a), (b), and (c) were reprinted with permission from [86]. d) In polythiophenes crystallites, the conjugation direction (along the polymer backbone) and the π-π stacking direction support fast charge transport, while charge transport in the insulating alkyl stacking direction is slower. Reprinted with permission from [94].

referred to as **conductivity enhancing agents** (CEAs), can improve carriers mobility and reduce the slowing effect of crystallite hopping on transport[95]. CEAs are typically introduced as additives into the organic conductor dispersion prior to film deposition or used in post-deposition treatments. Commonly used CEAs include high-boiling-point polar solvents such as dimethyl sulfoxide (DMSO) and ethylene glycol (EG), as well as inorganic salts like copper(II) chloride. Small percentages of CEAs are usually sufficient to induce large conductivity enhancements, while further increases in additive concentration can lead to excessive phase separation that isolates the single crystalline domains, reducing conductivity[96,97].

As previously mentioned, the van der Waals interactions holding molecules together in organic conductors allow polymer chains to reorganize in response to mild heat or solvent exposure, making them easy to process and allowing for a wide range of **solution processing strategies**, as opposed to the high-temperature and vacuum-based processes required for traditional inorganic semiconductors. Moreover, additives can contribute to improve film processability and stability. Molecular surfactants such as 4-dodecylbenzenesulfonic acid (DBSA) are commonly added in small amounts to improve wetting, adhesion, and film uniformity, while cross-linking agents such as 3-glycidoxypropyltrimethoxysilane (GOPS) are used to promote the formation of covalent bonds within the polymer network and to mitigate delamination in aqueous environments.

Modern molecular design and chemical engineering provide powerful tools to **tune a wide range of material properties** other than electronic behavior, including optical characteristics, mechanical compliance, surface chemistry, and the incorporation of biologically relevant functionalities.

This versatility is particularly appealing for **applications at the biological interface**, also considering that organic conductors, in contrast to their inorganic counterparts, typically do not form native oxide layers at their surfaces. This enables more direct and efficient interaction with biological fluids and to establish intimate ionic and electronic coupling with electrolytes, cells, and tissues, facilitating efficient signal transduction, like in **organic mixed ionic-electronic conductors (OMIECs)**. Moreover, their softness and compatibility with aqueous environments reduce mechanical mismatch with biological systems, making organic conductors especially well-suited for bioelectronics, biosensing, and implantable or wearable devices. In these systems, the tunability of the hydrophilic or amphiphilic character of the polymers influences the swelling in aqueous environments, that enhances ions transport in the bulk of the material (Figure 2.11). This property is particularly significant for applications in OECTs, where efficient bulk ion transport is essential for high performance device operation.

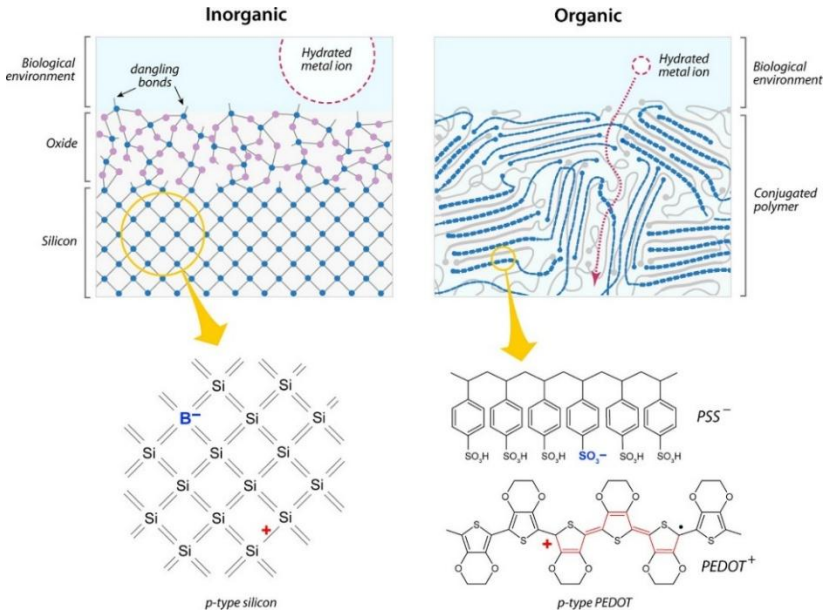

Figure 2.11 Schematics representations of silicon and PEDOT:PSS at the interface with an electrolyte, showing a typical interaction of p-doped inorganic and organic semiconductors, respectively, with the liquid environment. Reprinted with permission from [267].

2.2.1.3 Organic mixed ionic-electronic conductors

The concept of organic mixed ionic-electronic conductors (OMIECs) emerged during the 1980s to describe materials that combine features of conjugated polymers, polymer electrolytes, and polyelectrolytes, able to simultaneously support the transport of both electronic and ionic charge carriers and therefore of interest in electrochemical applications. In these systems, mixed ionic-electronic conduction arises from the presence of ion-permeable regions, often enabled by hydration, polymer swelling, or the presence of charged functional groups, which allow ionic motion to be coupled with electronic transport. Thanks to their ability to transduce ionic inputs into electronic output, and vice versa, OMIECs are particularly attractive for applications in ion pumps[98], organic transistors-based biosensors and neuromorphic devices[99–101], and as battery electrodes[102–104].

I. Polymer electrolytes

Polymer electrolytes are polymeric materials that dissolve and transport ions originating from an added salt. In these systems, the polymer backbone is electrically neutral, and ionic conductivity arises from the coordination of ions to polar functional groups along the polymer chain, like in poly(ethylene oxide) (PEO) and related polyethers.

II. Polyelectrolytes

Polyelectrolytes are polymers in which ionic charges are covalently bound to the polymer backbone, making the polymer itself a component of the salt. Oppositely charged mobile counterions provide ionic conductivity and balance the charges fixed to the backbone. For example, PSS presents negatively charged sulfonate groups attached to the polymer backbone and paired with cations such as Na^+ or H^+.

III. Classes of OMIECs

In OMIECs, while conjugated polymers provide electronic conduction, polymer electrolytes offer solvating environments for mobile ions, and polyelectrolytes supply fixed charges and counterions that facilitate volumetric electrochemical doping. The integration of these functionalities, either through blending, copolymerization, or side-chain engineering, allows OMIECs to support reversible, bulk ionic-electronic coupling.

Over time, OMIECs have been classified into distinct categories based on their chemical composition and morphology, reflecting different strategies for combining ionic and electronic transport (Figure 2.12)[105–107].

A first class of OMIECs consists of heterogeneous blends of conjugated polymers and polyelectrolytes, in which electronic and ionic charges are provided by different components. Part of this class is PEDOT:PSS, where the conjugated polymer PEDOT supports electronic conduction, while the PSS provides fixed ionic charges. In these systems, mixed conduction arises from phase separation and percolation between electronic and ionic domains.

Block copolymers and polymer-polyelectrolyte copolymers compose the second class, in which conjugated and ion-conducting segments are covalently linked within the same macromolecule. By adjusting block length, composition, and morphology, these materials allow fine control over swelling behavior, ionic mobility, and electronic transport.

Homogeneous conjugated polyelectrolytes constitute the third class, where ionic charges are incorporated into the conjugated backbone or side chains constituting an intrinsic part of the polymer structure, like in conjugated polymers bearing sulfonate, ammonium, or glycolated side chains.

In each of these classes, two different types of OMIECs can be identified: those in which ions are chemically linked to the molecule (types I, III, and V, respectively), and those in which ions are present as free species (types II, IV, and VI, respectively) (Figure 2.12). In case of OMIECs where one type of ionic species is covalently bound to the polymer backbone or side chains, while the opposite charge is mobile, unipolar ionic transport is observed in dry conditions. In contrast, other OMIEC classes allow both cations and anions to remain mobile, particularly in blended or neutral polymer systems. When OMIECs are brought into contact with a liquid electrolyte, polymer swelling facilitates the entrance of additional ions from the external solution, such that both positive and negative ionic species can participate in charge transport regardless of their mobility in the dry state.

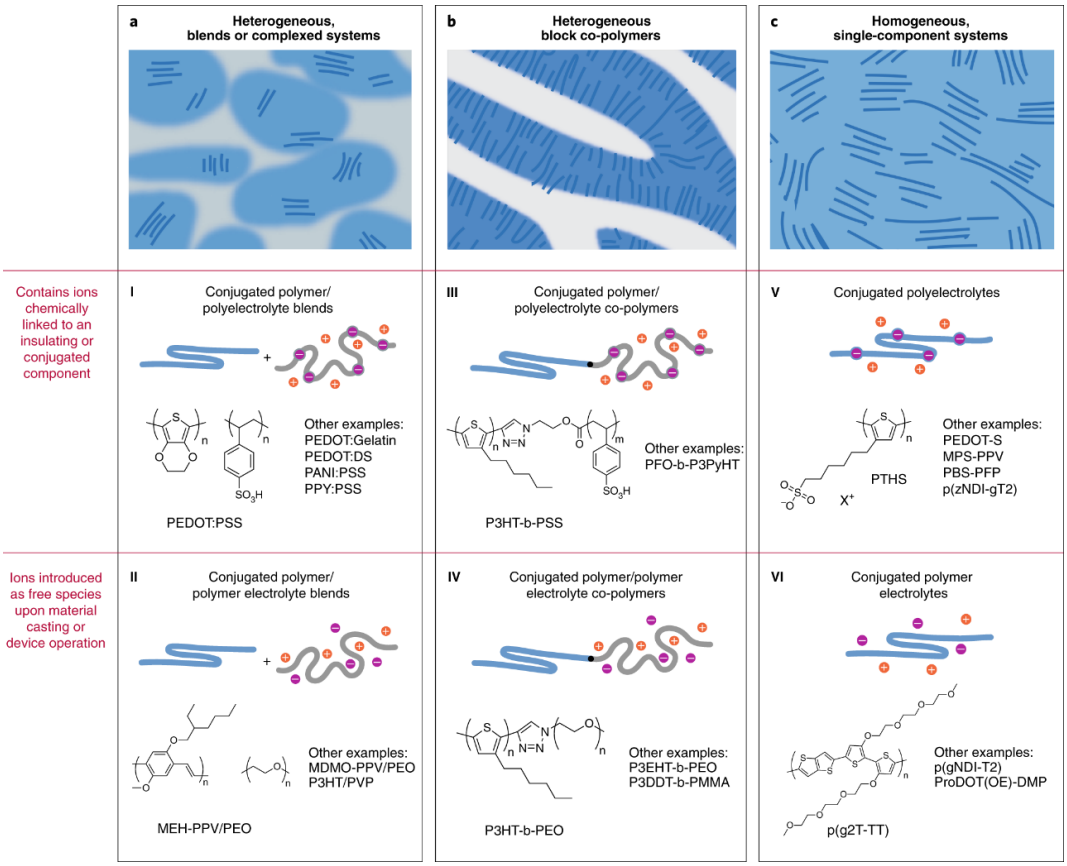

Figure 2.12 Classes and types of OMIECs. a) Heterogeneous blends of a conjugated polymer with (I) a polyelectrolyte or (II) an ion solvating polymer electrolyte. b) Heterogeneous block copolymers of a conjugated polymer with (III) a polyelectrolyte or (IV) an ion solvating polymer electrolyte. c) Fully conjugated (V) ionic charge bearing polyelectrolytes and (VI) ion solvating polymer electrolytes. Ionic transport components are represented in grey, electronic transport component in blue, cations in orange, anions in magenta. Reprinted with permission from [105].

2.2.1.3.1 Ionic transport mechanisms

The dominant mechanism of ion transport in OMIECs depends critically on the hydration state of the polymer film[105]. In dry or weakly hydrated materials, ionic motion occurs primarily through hopping processes assisted by segmental motion of polymer side chains or backbones. In this regime, extended rigid backbones tend to impede ionic mobility, while the introduction of ion-coordinating side chains enhances transport. In the presence of water, polymer chain mobility increases and ions are partially solvated, weakening ion-polymer interactions: the ionic transport transitions from hopping-dominated to vehicle transport, where ions migrate together with their solvation shells. At extreme hydration or electrolyte-swollen conditions, OMIECs are best described as conductive hydrogels, where continuous liquid pathways decouple ionic transport from polymer dynamics, and ionic conductivity approaches that of liquid electrolytes.

Ionic-electronic coupling

As previously discussed, every electronic charge introduced into the conjugated backbone of OMIECs must be stabilized by an oppositely charged ionic species, a process referred to as electrochemical doping. Depending on the OMIEC class, this stabilization may involve either mobile ions supplied from the electrolyte or fixed ionic groups intrinsic to the polymer structure. In materials containing fixed dopant charges, de-doping can only occur via the incorporation of mobile counterions of opposite sign. When an electric field is applied to an OMIEC under operation, electronic charge carriers, e.g., holes in p-type materials, locally disturb electroneutrality by creating regions of excess positive charge. To restore charge balance, mobile ions of opposite sign are driven to follow the charge carriers, giving rise to compensating ionic fluxes. Ionic motion in this context is not governed solely by concentration gradients, as would be expected for passive diffusion. Instead, the spatial redistribution of electronic charge drives ions via electromigration. This coupled transport mechanism can be described as a leader-follower dynamic, in which electronic carriers act as leaders and ions respond as followers to maintain local electroneutrality [108].

2.2.1.3.2 PEDOT:PSS

Since its formulation in 1988[109], aimed at overcoming the poor environmental stability and processability of earlier conducting polymers such as polyacetylene and polypyrrole[110], PEDOT has constituted a key material for a wide range of electronic and electrochemical applications. Consisting of a 3,4-disubstituted polythiophene conducting polymer, PEDOT combination with the polyelectrolyte PSS led to the commercial PEDOT:PSS formulation, in which the negatively charged PSS chains stabilize the positively doped PEDOT backbone in water, enabling solution processing from aqueous dispersions and making PEDOT:PSS one of the most widely used organic conductors in research and industry. Thanks to its high electrical conductivity, optical transparency in the visible range, mechanical flexibility, and chemical stability under ambient conditions, PEDOT:PSS has been successfully adopted for antistatic coatings, transparent electrodes for organic photovoltaics and light-emitting diodes, electrochromic displays, and energy-storage devices[111].

Owing to the presence of its stabilizing polyelectrolyte, PEDOT:PSS can be classified as **a type I organic mixed ionic-electronic conductor**, which makes it particularly suitable for operation in aqueous and biological environments, where ionic species play a functional role and mediate the reversible electrochemical doping and dedoping of the PEDOT backbone:

$$PEDOT^+PSS^- + M^+ + e^- = PEDOT^0 + PSS^-M^+$$

Indeed, PEDOT:PSS has become the benchmark channel material for OECTs thanks to its low operating voltage, volumetric capacitance, and biocompatibility. The conductivity of PEDOT:PSS can be tuned for specific applications by adding high-boiling-point solvents, surfactants, or cross-linking agents. Together with the wide availability of commercial solution processable blends, this versatility and tunability allow to experiment with various deposition techniques, from conventional thin-film processing to additive manufacturing approaches. Drop casting, spin coating, and electrospinning are common deposition techniques to obtain coatings and films with tunable thickness. Electrochemical polymerization can be performed in presence of inorganic or biological molecules, providing a deposition route to include functional elements in the polymerized film. More recently, screen printing, inkjet printing and aerosol-jet printing have attracted interest as rapid prototyping techniques enabling fast and high-throughput fabrication, with interesting outcomes in terms of film characteristics and morphology, which will be explored in the following chapter.

In PEDOT:PSS, conductive PEDOT chains randomly interact to organize in flattened aggregates into a PSS-rich, insulating matrix (Figure 2.13)[112–114]. This nanoscale **phase separation** contributes to limiting charge transport, as excess

PSS increases hopping barriers between PEDOT domains. Secondary doping or post deposition treatments with organic solvents, like ethylene glycol or DMSO, act on the distribution of PEDOT and PSS phases, enhancing conductivity by segregating the electronically insulating PSS. Highly polar CEAs interact with both PEDOT+ and PSS- chains, weakening their electrostatic coupling and enabling PEDOT domains to aggregate and form crystallites while segregating the electronically insulating PSS, which results in improved conductivity (Figure 2.13). Grazing-incidence wide-angle X-ray scattering (GIWAXS) and atomic force microscopy studies have shown that such treatments increase crystallite size, enhance interdomain connectivity, and reduce the thickness of the insulating PSS barrier between conductive regions, leading to orders-of-magnitude increases in electrical conductivity[115]. However, at sufficiently high concentrations of secondary dopants, large PEDOT-rich aggregates may become spatially isolated by PSS-rich regions, increasing morphological heterogeneity, and resulting in a saturation or a reduction of conductivity [116]. Several works identified an optimal dopant concentration at which the balance between PEDOT ordering, domain connectivity, and PSS redistribution maximizes electronic conductivity[117–122].

Relative humidity (rH) is the main parameter influencing PEDOT:PSS mechanical properties. Tensile tests proved that the Young's modulus of films increases from 0.9 GPa at 55% rH to 2.8 GPa at 23% rH, exhibiting plastic fracture behavior at 55% rH and brittle fracture behavior at rH = 23%[123], making PEDOT:PSS a great candidate for flexible electronics in ambient conditions or in biological environments.

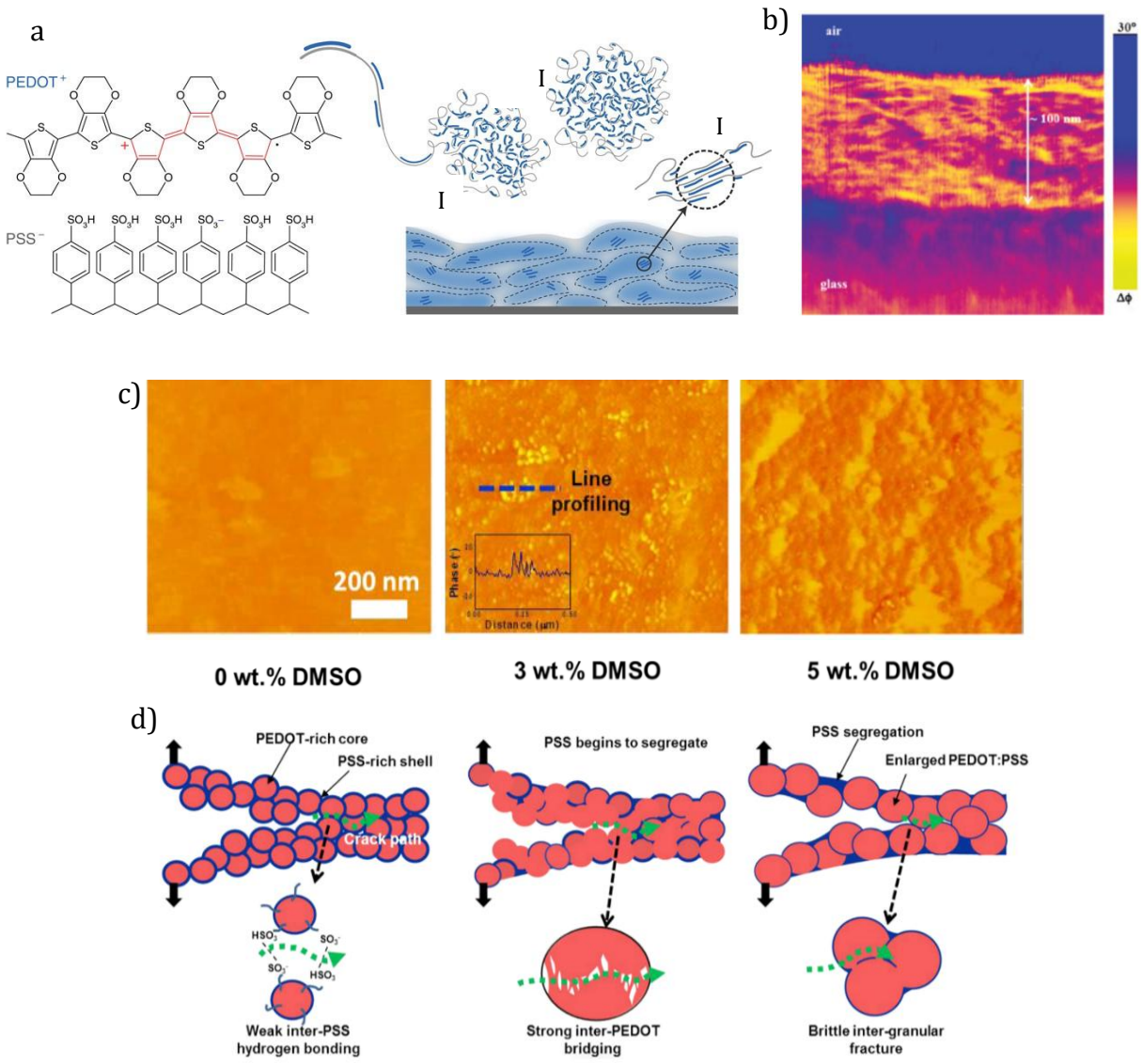

Figure 2.13 a) Chemical structure of PEDOT:PSS, where PEDOT positive charges are stabilized by the polyelectrolyte PSS. I) Microstructure of the type I OMIEC blend, which end up constituting PEDOT:PSS colloidal gel particles in dispersion (II). After film deposition, PEDOT:PSS-rich (blue) and PSS-rich (grey) phases can be observed (III), where PEDOT aggregates favor electronic transport (IV) (modified from [114]) b) AFM phase image of a cross-section of cleaved PEDOT:PSS film on glass, obtained from an aqueous dispersion containing 2.5 wt % sorbitol. Bright areas are interpreted as the PSS matrix, and the dark areas as PEDOT-rich aggregates [122]. c) AFM phase images of PEDOT:PSS surfaces mixed with 0, 3, and 5 wt % DMSO, respectively (modified from [117]). d) Schematics of PEDOT:PSS behavior after mixing with 0, 3, and 5 wt % DMSO (modified from [117]).

2.2.2 Organic Electrochemical Transistors (OECTs)

After the discovery of electrical conductivity in conjugated polymers, organic semiconducting materials rapidly attracted attention for a broad range of applications, like antistatic coatings, hole-conducting interlayers in optoelectronic devices, and components for energy storage[111,124]. With the progressive understanding of charge transport and electrochemical doping mechanisms in electrolyte environments, conjugated polymers were recognized as suitable active materials for transistor architectures, marking the emergence of organic electronics.

The first reports of Organic Field-Effect Transistors (OFETs) based on conjugated polymers began to appear in the 1980s, but a major leap occurred with the pioneering work of Mark S. Wrighton and co-workers, who observed the potential of organic conductors in electrolytes to achieve transistor operation at low voltages[125]. Wrighton and colleagues demonstrated that conducting polymers such as polypyrrole could function as the active channel of a transistor when immersed in an **electrolyte**, where small applied gate voltages modulated the oxidation state of the polymer and, consequently, its electrical conductivity, establishing the foundation for the study of electrolyte-gated organic transistors as powerful platforms for chemical and biochemical sensing.

Electrolyte-gated organic transistors are three-terminal devices composed of source, drain, and gate electrodes, where the source and drain are electrically connected by an organic semiconducting channel. The channel and the gate electrode are in contact with an electrolyte, which provides mobile ions that mediate device operation upon application of a gate voltage. Depending on the device architecture and the nature of the active material, two main classes of electrolyte-gated organic transistors can be distinguished: electrolyte-gated organic field-effect transistors (EGOFETs) and OECTs.

In EGOFETs, transistor operation is governed by the formation of electrical double layers at the interfaces between the electrolyte and the gate electrode and between the electrolyte and the organic semiconductor (Figure 2.13). Charge transport in EGOFETs is confined near the semiconductor-electrolyte interface, similarly to conventional field-effect transistors.

In contrast, OECTs operation mechanism is based on the **volumetric capacitance** of the organic mixed ionic-electronic conductor forming the channel (Figure 2.14). Upon application of a gate voltage, ions from the electrolyte penetrate the bulk of the organic semiconductor, inducing reversible electrochemical doping or dedoping throughout the entire channel volume. This bulk interaction between ionic and electronic charge carriers leads to high transconductance and sensitivity, making OECTs particularly attractive for sensing applications in aqueous and biological environments.

The physics and applications of OECTs will be discussed in this section, with focus on the use of PEDOT:PSS as the active channel material.

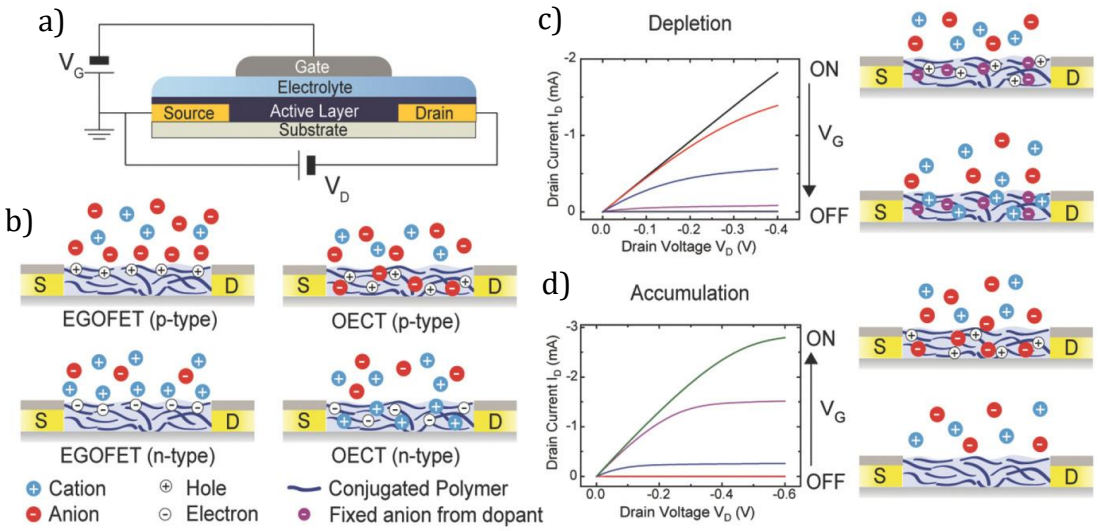

Figure 2.14 a) Schematic representation of an electrolyte-gated organic transistor. b) Types of electrolyte-gated organic transistor: field-effect (left) and electro-chemical (right) regime, with p- (top) or n-type (bottom) operation, dependent on the active material. c,d) Output characteristics and schematic illustration of the ion motion between the active layer and the electrolyte for OECTs working in depletion (c) and accumulation (d) mode. Reprinted with permission from [268].

2.2.2.1 Device physics

According to the Bernards and Malliaras model[126] for the description of the operation of OECTs, each device can be viewed as the superposition of two coupled subcircuits (Figure 2.15 e):

- an **electronic circuit**, governing hole (or electron) transport between source and drain through the OMIEC channel;
- an **ionic circuit**, describing ion motion between the gate electrode, the electrolyte, and the channel bulk.

The OECT is operated via application of a gate voltage that drives ions from the electrolyte into the bulk of the channel material, while a voltage applied between source and drain allows electronic transport along the channel, generating the drain current (Figure 2.15). Reversing the gate bias expels ions and restores the initial oxidation state. The channel conductivity depends on the local

doping level, which is controlled by the gate potential via ion penetration. Under steady-state conditions, the drain current of a p-type, depletion mode OECT can be expressed using MOSFET-like equations, where the interfacial gate capacitance is replaced by the volumetric capacitance of the OMIEC:

$$I_D = \mu C^* \frac{Wd}{L}\left[1 - \frac{V_{GS} - \frac{1}{2}V_{DS}}{V_{TH}}\right]V_{DS} \qquad \text{for} \quad V_{DS} > V_{GS} - V_{TH} \qquad (2.9)$$

$$I_D = -\mu C^* \frac{Wd}{L}\left|\frac{V_{GS} - V_{TH}}{2V_{TH}}\right|^2 V_{DS} \qquad \text{for} \quad V_{DS} < V_{GS} - V_{TH} \qquad (2.10)$$

in linear and saturation regime respectively. μ, the charge carrier mobility, and C^*, the volumetric capacitance of the channel, depend on the active material chosen for the device, while W, d, and L are width, thickness, and length of the channel, respectively. V_{GS} and V_{DS} are the gate and drain voltages, and V_{TH} is the threshold voltage of the device, which is the voltage at which the transistor switches off, dependent on the gate electrode material and electrochemical potential, on the concentration of ions in the electrolyte and their penetration in the channel, and on the architecture of the device [127].

The transconductance $g_m = \partial I_{DS}/\partial V_{DS}$ quantifies the ability of the device to convert small gate voltage variations into large drain current changes[127]:

$$g_m = \mu C^* \frac{Wd}{L} V_{DS} \qquad \text{for} \quad V_{DS} > V_{GS} - V_{TH} \qquad (2.11)$$

$$g_m = \mu C^* \frac{Wd}{L}[V_{GS} - V_{TH}] \qquad \text{for} \quad V_{DS} < V_{GS} - V_{TH} \qquad (2.12)$$

and represents a relevant figure of merit in the characterization of OECTs, providing a measure of the amplification capabilities of the device and allowing to compare different devices with the same geometric factors, or, when normalized with the device dimensions, to compare devices with different geometries. Moreover, its dependency on μ and C^* highlights the direct link between channel material properties and device performance. The prediction of transconductance given by the Bernards-Maillaras model, however, is not sufficient to describe the observed g_m of real devices, which usually displays a bell-shaped dependance from V_{GS}. This non-monotonic behavior was described by Friedlein *et al*. as effect of DOS filling and disorder-limited charge transport[128]. As previously mentioned in this chapter, in disordered organic semiconductors a Gaussian DOS can be assumed to describe the electronic states. Starting from a dedoped channel, increasingly negative V_{GS} introduce holes into the DOS, resulting in an increase in the carrier concentration and mobility, and leading to a rise in transconductance. As the Fermi gets closer to the center of the Gaussian DOS,

however, the increase in mobility slows down because additional carriers occupy less favorable transport states, and transconductance reaches a maximum. Upon further hole injection, when the DOS becomes more than half filled, additional carriers populate higher-energy states where energetic disorder reduces mobility, causing a decline in transconductance, which becomes negative.

The ionic circuit describes ion motion between the gate electrode and the channel through the electrolyte. Assuming that source and drain electrodes do not participate in Faradaic reactions (which generate currents via redox reactions at the electrode surface) and the gate current is purely capacitive, ionic transport is governed by charging and discharging of the channel capacitance through the finite resistance of the electrolyte. The ionic circuit can be represented as a resistor-capacitor (RC), where the electrolyte resistance limits ion flux and the channel volumetric capacitance stores ionic charge that compensates electronic carriers in the polymer backbone. When the gate voltage changes, the RC time constant of the ionic circuit determines the current response:

$$I_D(t, V_{GS}) = I_S(V_{GS}) + \Delta I_{SS}\left(1 - f\frac{\tau_e}{\tau_i}\right)e^{-\left(\frac{t}{\tau_i}\right)} \tag{2.13}$$

with $I_S(V_{GS})$ steady-state drain current at gate voltage V_{GS}, and $\Delta I_{SS} = I_S(V_{GS} = 0) - I_S(V_{GS})$. $\tau_e = \frac{L^2}{\mu V_{DS}}$ is the electronic time of flight along the channel and τ_i is the RC time constant of ionic transport in the electrolyte, while f is a geometric parameter accounting for spatial inhomogeneity of the dedoping process[129]. Depending on the ratio between τ_e and τ_i, two regimes can be observed: a monotonic relaxation when electronic transport is faster than ionic motion, and a non-monotonic response when ion motion dominates. Under large gate-voltage sweeps or high scan rates, these effects become evident in a hysteresis in OECT transfer characteristics, which is also influenced by ion trapping, swelling-induced morphological changes, and redox kinetics within the OMIEC.

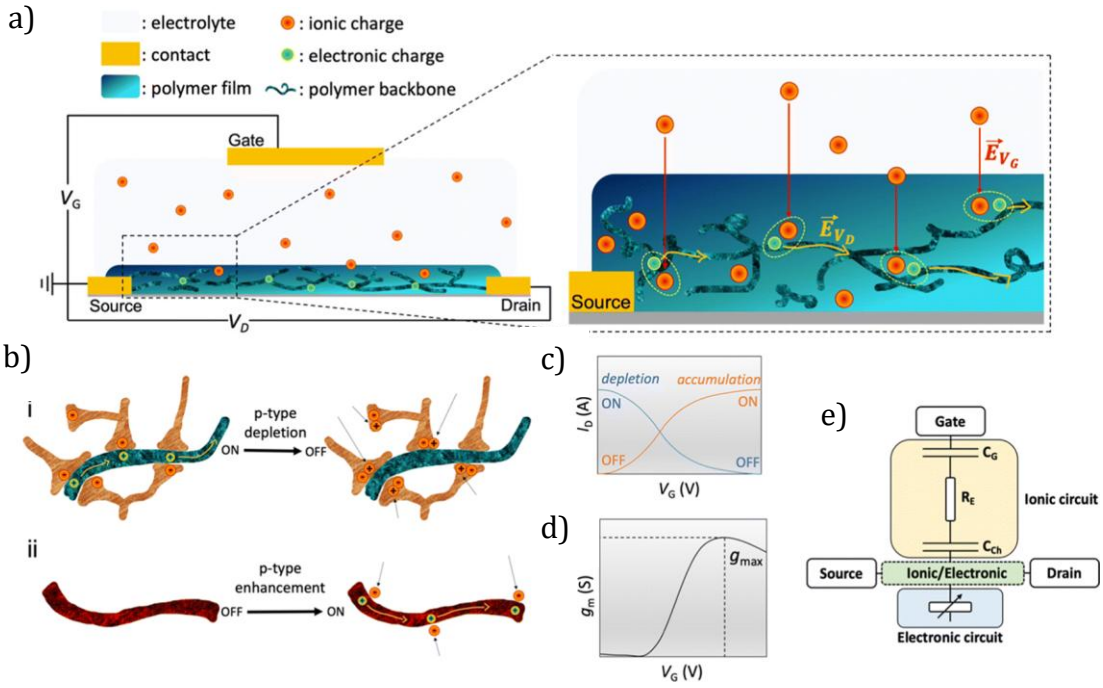

Figure 2.15 a) Illustration of the operating principle of an OECT. An electric field applied at the gate (E_{VG}) drives ions from the electrolyte into the OMIEC channel, while an electric field applied between source and drain (E_{VD}) induces electronic transport along the channel. b) Schematic representation of two operating regimes for p-type OECTs: (i) depletion-mode, in which cation penetration into the channel compensates negatively charged dopants and reduces the hole concentration; and (ii) enhancement-mode, where entering anions stabilize additional holes, increasing channel conductivity. c) Representative transfer characteristics for depletion and enhancement-mode OECTs. d) Corresponding transconductance. e) Equivalent electrical circuit model used to describe OECT operation, where R_E represents the ionic resistance of the electrolyte, and C_G and C_{Ch} indicate the gate and channel capacitances, respectively. Reprint from [127].

In real devices, when a polarizable metal gate like Au or Pt is used, not all the applied gate voltage drops across the channel. In this condition, the ionic circuit contains two capacitive elements in series: the electrical double layer capacitance at the gate-electrolyte interface and the volumetric capacitance of the channel. The effective capacitance is therefore:

$$C_{eq} = \left(\frac{1}{C_G} + \frac{1}{C_{CH}}\right)^{-1} \tag{2.14}$$

and **efficient channel modulation requires C_G>>C_{CH}**. This condition can be achieved by using large-area gates, thick conducting-polymer gate electrodes, or nonpolarizable reference electrodes such as Ag/AgCl, which minimize voltage loss at the gate interface. Gate geometry and material choice thus play a central role in determining the effective gate bias experienced by the channel.

2.2.2.2 Ionic liquids and solid electrolytes

OECTs are traditionally operated in liquid electrolytes, which are used as representatives of the biological environment or biological fluids. However, the reliance on mobile ions in an aqueous environment leads to comparatively slow device dynamics, as ionic motion is several orders of magnitude slower than electronic transport, resulting in long charging and discharging time constants. Moreover, prolonged operation in aqueous electrolytes may trigger unintended redox processes, leading to drift in device baseline, reduced transconductance, and long-term instability. Ionic liquids (IL) are salts that remain liquid at or near room temperature and are characterized by high ionic conductivity, wide electrochemical stability windows, negligible vapor pressure, and excellent thermal stability[130,131]. When incorporated into polymer matrices to form solid or gel electrolytes, ILs can enable faster OECT switching compared to aqueous electrolytes, with response times closer to those limited by ion drift rather than diffusion[132–134]. Moreover, solid-state IL electrolytes can be finely patterned, allowing the creation of locally gated OECTs in which the electrolyte is confined to the vicinity of a single device, eliminating ionic crosstalk between adjacent transistors, and reducing leakage. Overall, solid electrolytes reduce evaporation and instability, enabling prolonged operation under ambient conditions.

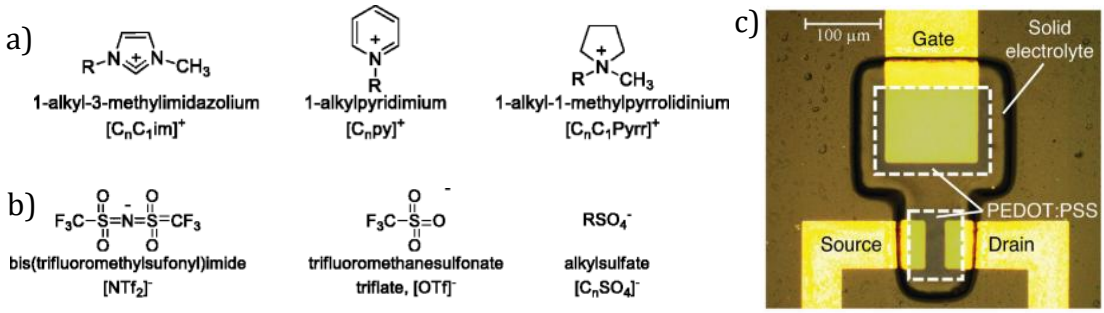

Figure 2.16 Some frequently used cations (a) and anions (b) for ionic liquids. Reprint from [269]. c) A photopatterned solid electrolyte on an OECT. Reprint from [131].

2.2.2.3 Fabrication of OECTs

Traditional OECTs are usually produced via **microfabrication** protocols adapted from silicon-based electronics. Typically, devices are fabricated on rigid substrates such as silicon wafers with a thermally grown SiO_2 layer or on glass, and metallic source, drain, and gate electrodes are defined through photolithography. The metal deposited via thermal or electron-beam evaporation is usually gold, preceded by an adhesion layer of titanium. Parylene-C, SU-8, or Al_2O_3 are then deposited and patterned to create a passivation layer, leaving only the channel region and electrode contacts exposed to the electrolyte[127]. The OMIEC is then deposited to connect the source and drain electrodes, typically by spin coating, drop casting, or inkjet printing, followed by thermal annealing or solvent treatments to optimize film morphology and electrical performance.

Beyond thin films, scaffolds and fibers can also be integrated into OECTs to realize 3D or 1D channels, respectively (Figure 2.17). Fiber-based channels can be obtained either by coating commercial fibers with an OMIEC solution[135,136], via electrospinning of the semiconducting fiber[137,138], or via electro-polymerization[139]. 3D channels can be obtained via freeze drying to create porous tridimensional structures, or by formulating swellable gels [127].

While these fabrication routes enable precise control over device geometry and high reproducibility, they are often cost-intensive, time-consuming, and poorly suited for disposable applications. Recently, increasing attention has been devoted to additive manufacturing techniques as alternatives to conventional microfabrication. Methods such as **inkjet printing, screen printing, aerosol jet printing, and dispense printing** allow direct patterning of electrodes, OMIEC layers, and solid electrolytes under ambient conditions, reducing material waste and process complexity[140–145]. These approaches are compatible with flexible and paper-based substrates and support rapid prototyping and scalable production, making them particularly attractive for low-cost, wearable, and point-of-care OECT platforms.

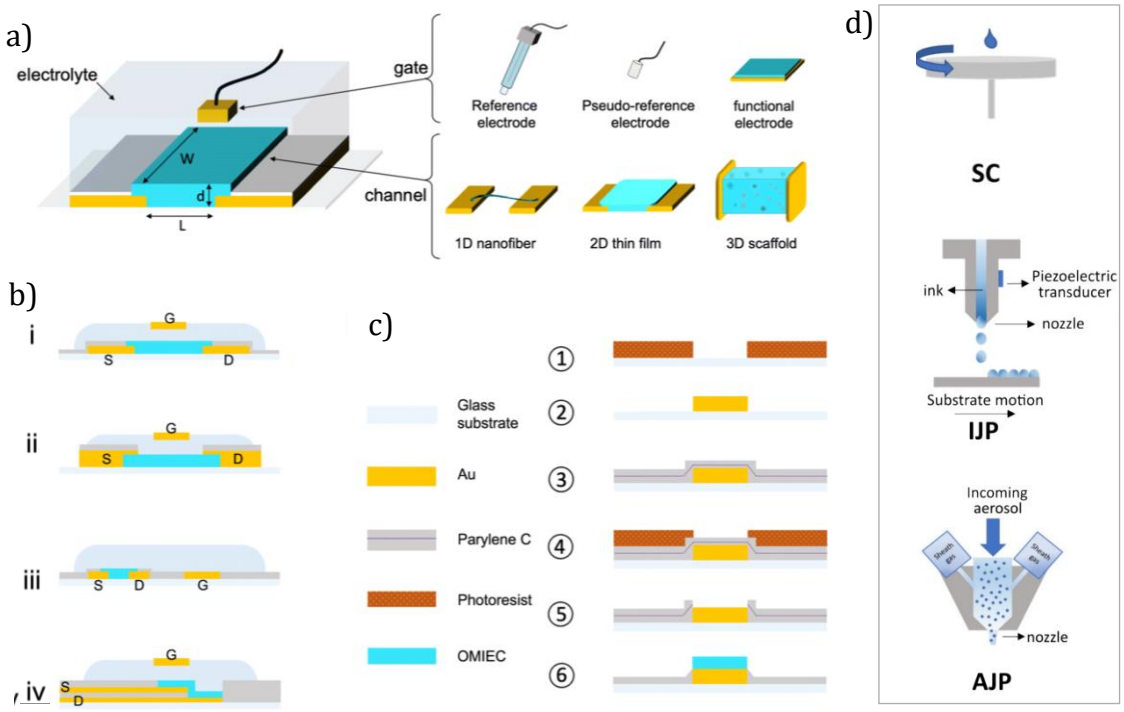

Figure 2.17 a) Schematic of a traditional OECT architecture, with the channel key geometrical parameters and different gate and channel configurations. b) Common OECT architectures: bottom contact (i), top contact (ii), coplanar (iii), and vertical (iv). c) A typical photolithographic process for the microfabrication of OECTs. Reprint from [127]. d) Schematic representation of some of the most common deposition techniques for OMIECs thin films: spin coating (SC), Inkjet printing (IJP), Aerosol-jet printing (AJP) (modified from [140]).

2.2.2.4 OECTs for chemical and biochemical sensing

Their signal amplification capabilities and their great performances in aqueous environments have brought OECTs to stand out as powerful platforms for chemical and biochemical sensing. Moreover, their architectural versatility allows them to adapt to various applications, from flexible, wearable devices to complex microfluidic systems [146–150].

When used in ion sensing, pH sensing, and electrolyte monitoring in physiological fluids and environmental samples, exploiting their intrinsic sensitivity to ionic fluxes and electrochemical doping processes, OECTs gate electrode or channel can be functionalized with an ion-selective membrane (ISM) that

transports or excludes specific ionic species[148,151,152]. Materials such as Nafion, a sulfonated fluoropolymer with high cation conductivity, are frequently employed to impart selectivity toward protons, alkali metal ions, or other cations while rejecting anions[153,154]. When an ion-selective membrane is integrated into the OECT architecture, changes in the concentration of the target ion modulate the effective gate potential or the ionic penetration into the channel, altering the drain current.

When used in a biosensor configuration, OECTs gate electrode is typically functionalized with a **biomolecular recognition layer** that selectively interacts with the target analyte[155–159]. When binding events occur at the gate-electrolyte interface, the capacitance and interfacial potential of the gate are altered, varying the effective gate voltage dropping across the channel-electrolyte interface. This modulation leads to a change in the channel doping level and in the resulting drain current, which can be correlated to the number of binding events at the gate interface, and therefore, to the analyte concentration in the sample. This amplification mechanism, through which small interfacial changes at the gate are converted into large variations in drain current, supports the high sensitivity of OECT-based biosensors and stimulates the exploration of various surface functionalization strategies for both gate electrodes and channel materials.

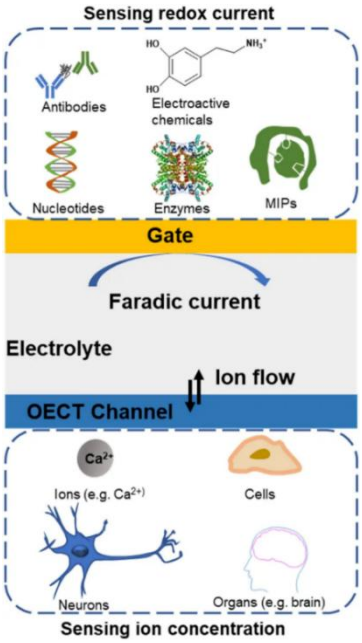

Figure 2.18 Schematic representation of the interaction between biological systems and OECTs. Reprint from [270].

Functionalization techniques

Functionalization refers to a preparatory step aiming to impart chemical or **biological selectivity** to the sensor. In the case of OECTs, functional recognition elements can be implemented either at the gate electrode or directly within the channel material, depending on the sensing mechanism and target analyte. Chemisorption and physisorption are common functionalization strategies with different trade-offs in stability, sensitivity, and fabrication complexity.

The most widely used **chemisorption** strategy for the functionalization of gold gate electrodes relies on thiol chemistry, where alkanethiols or functional thiols chemisorb onto gold surfaces to form self-assembled monolayers (SAMs). SAMs can be terminated with functional groups, like carboxyl or amine groups, that are then activated using EDC/NHS chemistry to covalently immobilize biomolecules. This approach grants robust biolayers with long-term stability under continuous operation and repeated measurements, although the multistep functionalization process increases fabrication time and complexity.

In contrast, **physisorption**-based functionalization exploits non-covalent interactions to immobilize recognition elements. Electrostatic forces or hydrogen bonding allow enzymes or antibodies to be directly adsorbed onto gate electrodes or polymeric surfaces with minimal surface preparation. In case of channel functionalization[160–162], recognition elements such as enzymes, DNA strands, or molecular receptors are incorporated directly into the OMIEC, either by blending them into the polymer matrix or by post-deposition adsorption. This strategy has been widely applied in enzymatic OECT sensors, where enzymatic reactions generate ions or redox species that locally alter the channel's doping state. Including biomolecules into ion gels is also adopted as an easy strategy to obtain selective sensors (Figure 2.19)[163–168]. Ion gels, typically composed of polymer matrices incorporating ILs, provide a hydrating and ionically conductive environment that preserves biomolecular activity while ensuring efficient coupling with the OECT channel. Enzymes immobilized in ion gels have been shown to retain catalytic activity and to transduce biochemical reactions into ionic fluxes that modulate the OECT current, also thanks to the reduced evaporation, even under ambient or elevated temperatures, that contributes to prevent denaturation[169].

While these strategies are attractive for low-cost fabrication, they generally result in weaker binding and poorer long-term stability, with biomolecules being more susceptible to desorption, denaturation, or displacement during device operation[170].

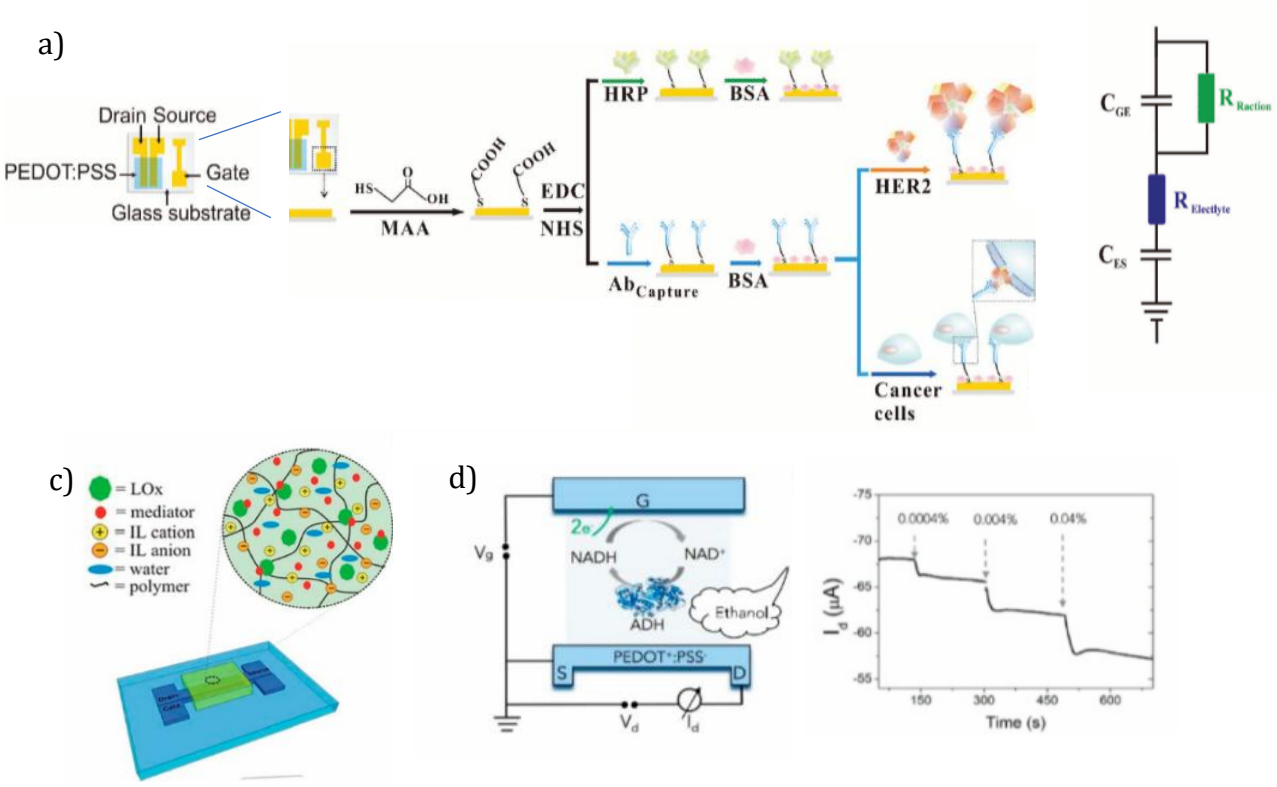

Figure 2.19 a) Schematic representation of an OECT-based biosensing platform for the detection of the cancer biomarker HER2. Gate functionalization strategies used for sensing the HER2 protein and HER2-expressing cancer cells include the formation of a self-assembled monolayer and its chemical activation for the exposition of functional groups; the covalent binding of horseradish peroxidase (HRP), HER2 protein, or cancer cells; the passivation of unreacted sites with bovine serum albumin (BSA). Right: Equivalent electrical circuit for the gate-channel coupling in an OECT operating in an electrolyte, with CGE and CEC denoting the electric double-layer capacitances at the gate/electrolyte interface and electrolyte/channel interface, respectively. Reprinted with permission from [271]. c) Schematic description of components of an enzyme-containing ion-gel electrolyte. Reprinted with permission from [168]. d) Schematic of the enzymatic reaction of ethanol and alcohol dehydrogenase in an enzyme-containing ion-gel on a disposable alcohol sensing OECT; below, the variation in drain current when adding 0.0004%, 0.004%, and 0.04% ethanol solutions to the sensor. Reprint from [169].

OECTs integration in microfluidic platforms

The integration of OECTs into microfluidic platforms has emerged as an effective strategy to enhance device reliability and improve long-term stability. By confining liquids in microchannels, microfluidic set ups prevent direct exposure of the OMIEC channel to complex biological samples containing proteins, cells, or fouling agents, which can alter the current response in a non-predictable way and degrade device performance. In these configurations, the channel is often isolated from the analyte flow, while sensing reactions are confined to the gate (Figure 2.20)[45,48]. Moreover, microfluidics can enhance reproducibility and improve the measure outcome, enabling precise handling of small volumes, automated delivery of samples and reagents, and controlled flow rates. Overall, coupling OECTs with microfluidics facilitates multiplexed sensing and dynamic measurements such as real-time monitoring of enzymatic reactions or cell-secreted metabolites within a single lab-on-a-chip system, resulting particularly suited for point-of-care diagnostics, organ-on-chip systems, and long-term monitoring in complex biological media[37,40,46,171,172].

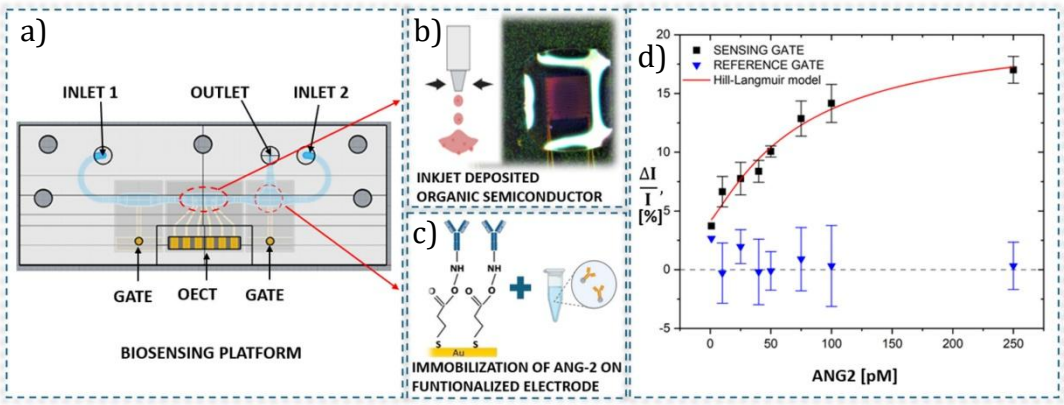

Figure 2.20 a) Microfluidic platform integrating an organic transistor-based biosensor for the detection of Angiopoietin-2. b) Deposition of the organic semiconductor via inkjet-printing. c) Functionalization scheme of the gold gate electrode via SAM of thiols and EDC/NHS chemistry. d) Sensor response at varying concentrations of analyte. Reprint from [48].

Chapter 3

3 Characterization of printed PEDOT:PSS films

3.1 Overview

3.1.1 PEDOT:PSS printing

While early PEDOT:PSS patterning often relied on spin coating and photolithography steps, printing techniques have recently emerged as scalable, low-cost, and versatile solutions for the fabrication of organic electronic devices, enabling direct deposition of PEDOT:PSS only where needed and reducing process complexity, fabrication time, and material waste. Among these approaches and compared to contact printing techniques, inkjet printing and aerosol jet printing are particularly attractive for organic electronics, as they are non-contact, mask-free, high-resolution deposition techniques that enable direct patterning of functional materials on a great variety of substrates.

3.1.1.1 Inkjet printing

Inkjet printing technology is based on the dispensing of picoliter droplets from small nozzles, ranging from tens of microns to a few hundred microns, via periodic excitation of a piezoelectric element in the printhead (Figure 3.1 a). An electric field then orients the ejected droplets on the substrate according to the given digital pattern, allowing maskless fabrication of features with micrometer-scale resolution. This technique enables rapid design iteration and customization, and it is especially suited for flexible electronics and substrates that are incompatible with photolithographic chemicals or high-temperature processing.

Fluids rheological characteristics determine their behavior during jetting and droplet formation. Properties such as viscosity, surface tension, and density influence the liquid breakout into droplets and the formation of undesired effects, such as satellite droplets or nozzle clogging. Dimensionless numbers are commonly employed to explain the interplay between different rheological variables and to define criteria for printability.

The Reynolds number (N_{Re}) is the ratio between inertial forces and viscous forces in a flowing fluid:

$$N_{Re} = \frac{va\rho}{\eta} \qquad 3.1$$

where v is the average travel velocity, a is the radius of the nozzle orifice, ρ is the fluid density, and η its viscosity. The Weber number (N_{We}) is the ratio between inertial and capillary forces:

$$N_{We} = \frac{v^2 a\rho}{\gamma} \qquad 3.2$$

where γ is the fluid surface tension. From these dimensionless parameters, the Ohnesorge number, Oh, can be defined as:

$$Oh = \frac{\sqrt{N_{We}}}{N_{Re}} = \frac{\eta}{\sqrt{a\rho\gamma}} \qquad 3.3$$

which does not depend on the fluid velocity[173]. Based on numerical simulations of incompressible free-surface flows, studies identified an optimal printability window for $Z = 1/Oh$ higher than 1 and 14: when close to the lower limit of the range, the pressure pulse is hindered by excessive viscous damping, while satellite droplets start forming when close to the upper limit [174,175] (Figure 3.1 b, c).

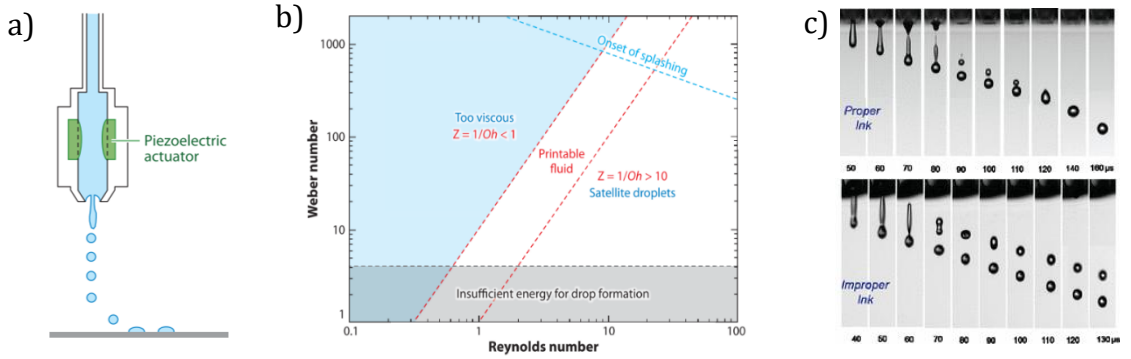

Figure 3.1 a) Schematic representation of the working principle of an inkjet printing head. Reprinted with permission from [175]. b) Schematic diagram illustrating the operating regimes of inkjet printers as a function of ink properties. Reprinted with permission from [175]. c) Photo sequence of a drop ejected form a nozzle, for fluids with values of Z = 13.68 (top image) and Z = 17.32 (bottom image). Reprinted with permission from [174].

In microelectronics, inkjet printing is particularly attractive thanks to its compatibility with a wide range of substrates, including plastics, paper, and textiles[176–179]. Since the 2000, inkjet printing has been employed to pattern conductive tracks based on silver, gold, or carbon inks, and to finely print semiconducting polymers like poly(3-hexylthiophene) (P3HT) and PEDOT:PSS, and dielectric layers for capacitors and transistors like polyimides, fluoropolymers, or inorganic dielectrics based on silica or alumina[178,180,181].

Compared to the optimal window for drop on demand inkjet printing, commercial PEDOT:PSS dispersions are characterized by relatively high surface tensions, above 60 mN/m, and viscosities close to that of water, that often lead to poor drop formation and satellite droplets[182]. The addition of organic solvents and surfactants can tune viscosity, surface tension, and wetting behavior of the printed ink on the substrate. High boiling point polar solvents such as ethylene glycol, dimethyl sulfoxide, glycerol, or sorbitol are typically added in small volume fractions to increase viscosity and lower surface tension, while also acting as secondary dopants that enhance film conductivity after drying and annealing; surfactants can be incorporated at low concentrations to further reduce surface tension and improve definition of the printed features (Figure 3.2)[183–185].

Overall, great processability, tunable rheology, and conductivity enhancement through ink formulation has made PEDOT:PSS one of the most widely inkjet-printed organic conductors.

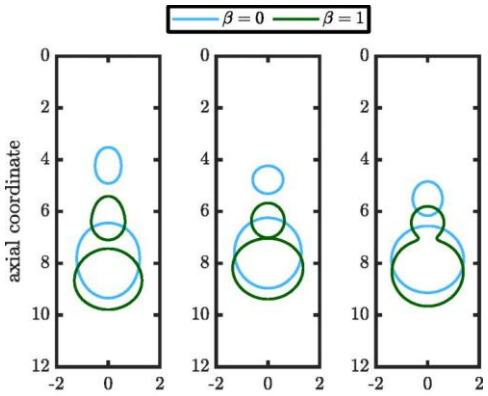

Figure 3.2 Effect of viscosity and surfactant concentration on droplet shape: an increase in viscosity and introduction of a surfactant (β = 1) reduce the formation of satellite drops. From left to right: Oh = 0.05, 0.09, 0.16, N_{Re} = 17.5, 8.75, 5, and N_{We} = 0.68 Reprint from [185].

3.1.1.2 Aerosol jet printing

In aerosol jet printing, inks formulated as solutions or nanoparticle suspensions of metals, ceramics, polymers, or biomolecules are introduced into an atomizer, where they are converted into an aerosol composed of liquid droplets with diameters typically ranging from tens of nanometers to a few micrometers[186]. A nitrogen flux then focuses and delivers the aerosol to the substrate, allowing precise patterning of fine features. (Figure 3.3)

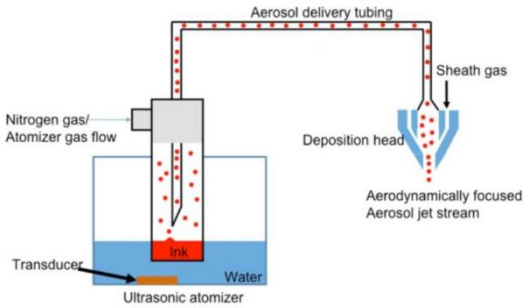

Figure 3.3 Representation of the aerosol jet printing process. Reprint from [272].

Aerosol jet printing allows to deposit features with lateral dimensions down to approximately 10 to 20 µm, on rigid and flexible substrates with minimal material waste, and it has been applied to the fabrication of printed interconnects, antennas, thin film transistors, sensors, stretchable electronics, and biointerfaces[187,188]

Compared with inkjet printing, aerosol jet printing accepts inks with a broader viscosity range, from about 1 to 1000 mPa*s depending on the atomization method[189,190]. Nevertheless, in case of colloidal dispersions, inks must exhibit stability and controlled volatility to prevent premature drying in the nozzle. Therefore, similarly to inkjet-printable inks, additives are often incorporated to adjust viscosity and surface tension, ensuring high line definition[140,191]. However, defects related to the techniques, like edge profile instability (often referred as overspray) continues to be a challenge in aerosol jet printed features[192].

Droplet size distribution, solvent evaporation rate, and substrate temperature affect film microstructure and phase segregation[193]. For PEDOT:PSS, printed films often exhibit differences in grain size, roughness, and PEDOT to PSS phase distribution compared to spin coated films[192].

3.1.2 Characterization techniques

3.1.2.1 Electrical characterization

The standard measurements to assess charge transport, stability, and material properties in OECTs include output characteristics, transfer characteristics, and transconductance, which, in the saturation regime, is proportional to the product of electronic mobility and volumetric capacitance, denoted as μC*.

Output characteristics are obtained by recording the drain current I_D as a function of the drain voltage V_{DS} while keeping the gate voltage V_{GS} constant (Figure 3.4). In p-type depletion-mode devices based on PEDOT:PSS, increasing the magnitude of V_{DS} at a fixed V_{GS} leads to an initial quasi-linear increase of I_D, followed by current saturation when the channel approaches the pinch-off voltage, corresponding to the condition where conductive channel becomes locally depleted near the drain electrode, leading to no further increase in current.

Transfer characteristics are measured by sweeping V_{GS} at a fixed V_{DS} and recording I_D (Figure 3.4). From these curves, the ON current, typically defined as the maximum I_D in the conductive state, and the OFF current, corresponding to the minimum I_D in the dedoped state, can be extracted, and their ratio I_{ON}/I_{OFF} can be evaluated as a performance parameter representative of the dynamic range of the device. By sweeping V_{GS} forward and backward, hysteresis can be commonly observed in the transfer curve of PEDOT:PSS-based devices (Figure 3.4), indicating slow ionic motion, charge trapping, or structural rearrangements within the hydrated polymer film, and providing information on

reversibility of electrochemical doping and suitability for sensing or logic applications[127].

In PEDOT:PSS-based devices, the transfer curve often exhibits a non-monotonic transconductance g_m due to density-of-states effects and doping-dependent mobility. In the saturation regime, the transconductance g_m is linearly dependent on the channel geometry factor Wd/L, where W is the width, d the thickness, and L the length of the channel, and on the biasing conditions. The slope of this line gives the μC* product (Figure 3.4), which reflects the mixed conduction performance of the printed PEDOT:PSS film independently of geometry, and is therefore used to compare materials, formulations, and post-treatment strategies in the literature[127].

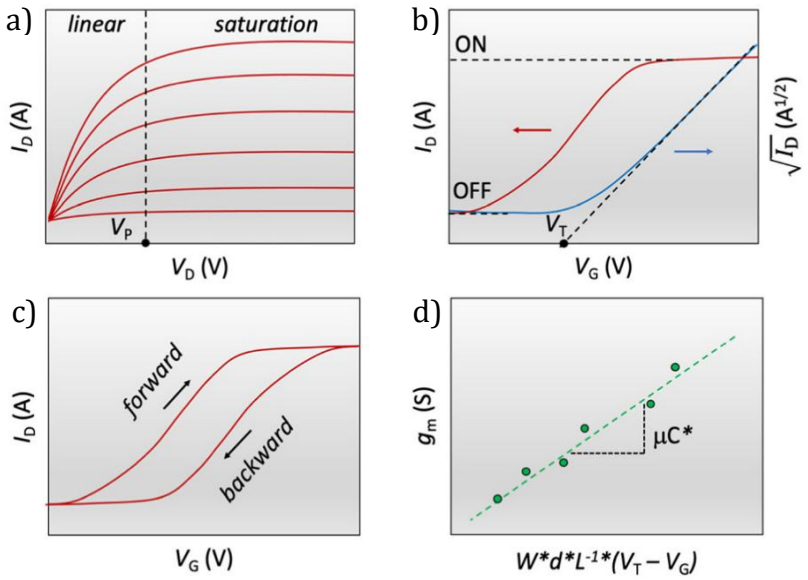

Figure 3.4 Schematics of the key figures of merit of an OECT in the steady-state. a) Output characteristics; b) I_D (red) and $\sqrt{I_D}$ (blue) as a function of gate voltage, with V_T obtained from the x-axis intercept; c) transfer curve hysteresis; d) the g_m as a function of channel geometry and biasing conditions, where the μC* product is the slope of the linear relationship between the plotted g_m points. Reprint from [127].

3.1.2.2 Raman spectroscopy

Raman spectroscopy is a vibrational spectroscopic technique based on Raman scattering, that is the inelastic scattering of light by matter[194]. When incident photons excite the system, a small fraction is scattered with an energy shift corresponding to molecules vibrational modes, giving information on bonding,

conformation, and electronic structure. In PEDOT:PSS, Raman bands associated with the PEDOT backbone are sensitive to oxidation state and chain conformation. The technique is therefore frequently used to observe the effects of conductivity-enhancing treatments on the molecular structure, and to correlate spectra with optical or electronic behavior[195–197].

In Raman spectroscopy, the excitation wavelength is generally chosen away from electronic absorption bands, so to minimize fluorescence and ensure that photons are scattered rather than absorbed[198]. When monochromatic light interacts with matter, most photons are scattered elastically, retaining the same energy as the incident radiation, in a process known as Rayleigh scattering. Typically, only one photon out of 10^6 to 10^8 goes through inelastic scattering, which is known with the name of Raman scattering[194].

The physical origin of Raman scattering lies in the interaction between the oscillating electric field of the incident light and the electronic cloud of the material. If a diatomic molecule is irradiated, the electric field induces a dipole moment μ in the molecule, which is proportional to the electric field E and the polarizability α of the system, as $\mu = \alpha E$[194]. For a vibrational mode to be Raman-active, it must involve a variation in polarizability during the vibration. If the polarizability changes as atoms vibrate along a given normal mode, the induced dipole will oscillate at the incident frequency and at frequencies shifted by the vibrational energy of the mode[199]. These additional frequency components correspond to the Raman-shift observed in the spectrum.

The Raman spectrum consists of a central elastic peak at the excitation frequency and two sets of inelastic features, called Stokes and anti-Stokes lines. Stokes lines are observed when the incident photon transfers part of its energy to the material, promoting it from the vibrational ground state to an excited vibrational level, and emerging with lower energy after the scattering. In anti-Stokes scattering, the molecule is originally in an excited vibrational state and transfers energy to the photon, resulting in a higher-energy scattered photon (Figure 3.5)[199].

In conjugated polymers, high wavenumbers are typically associated with stretching vibrations due to periodic changes in bond length, while bending modes, involving variations in bond angles, are associated with lower wavenumbers. In polythiophenes, symmetric C=C stretching along the conjugated backbone, observed in the 1420 to 1450 cm^{-1} region, inter-ring C-C stretching, found near 1250 to 1270 cm^{-1}, and ring deformation modes are particularly sensitive to oxidation state, conjugation length, and molecular ordering[196,200–202].

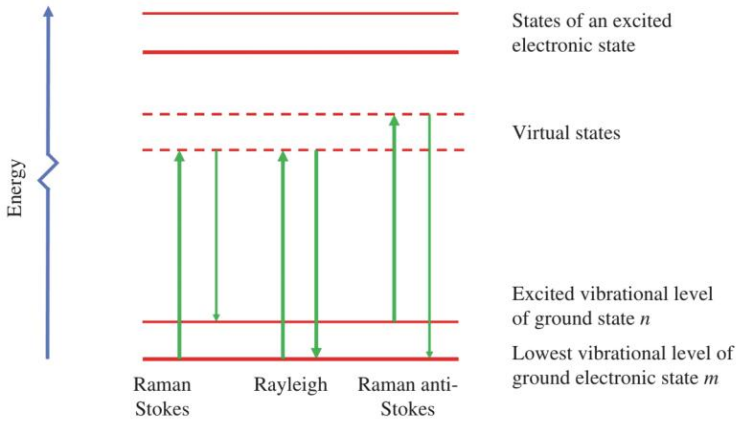

Figure 3.5 Diagram of the elastic and inelastic components of the scattering process. The upward arrows represent the excitation energy, the downward arrows represent the scattered energy. Reprint from [199].

3.1.2.3 Atomic force microscopy

Atomic force microscopy (AFM) is classified among the scanning probe microscopy (SPM) techniques, in which a sharp probe, by locally interacting with the sample, scans a surface providing an output with nanometer or sub-nanometer resolution. In AFM, interatomic forces between a nanoscale tip and the sample surface are measured to obtain samples topography, or to extract information about the surface electrical or mechanical properties.

In material science, AFM is frequently employed to evaluate films roughness, domain structure, and phase segregation, which in organic conductors strongly influence electronic and ionic transport. Beyond roughness, AFM phase can be exploited to distinguish mechanically and chemically different domains, like in PEDOT:PSS, whose microstructure is often described as stiff PEDOT-rich conducting regions embedded in softer insulating PSS-rich matrix[113,203–205].

Operating modes

The scanning head of an AFM hosts a microfabricated cantilever, typically tens to hundreds of micrometers long, bearing a sharp tip at its free end, with an apex radius of a few to tens of nanometers. As the tip scans across the sample surface, forces between atoms at the tip apex and those at the sample surface deflect the cantilever. Through an optical lever method, a laser beam focused on

the back of the cantilever is reflected on a photodiode, allowing to detect its displacement and to transduce it into measurable variables.

The operating mode depends on the tip-sample distance, and consequently on the resulting interaction regime and on nature of the forces between them [206](Figure 3.6).

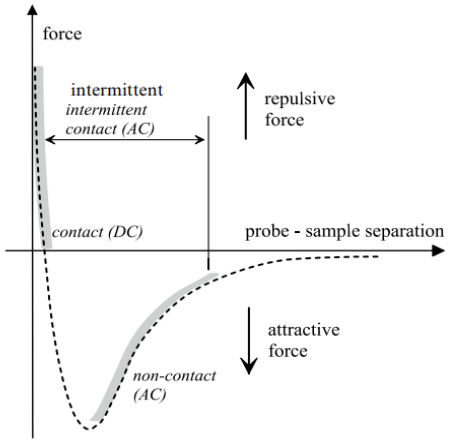

Figure 3.6 Representative plot of the force between tip and sample in function of their distance, indicating the typical ranges for the principal AFM operating modes. Reprint from [206].

Contact mode

In contact mode, the tip is close enough to the surface so that short-range Pauli repulsion dominates (Figure 3.7 a). The tip remains in contact with the surface, and surface topography is reconstructed by maintaining constant deflection (constant force mode). While providing high-resolution topography, this mode may induce lateral forces that can damage soft samples. Recently, the availability of soft silicon nitride cantilevers has allowed to adopt contact mode imaging even on biological samples, thanks to the small spring constant that results in reduced shear forces on the samples[206].

Non-contact mode

In non-contact mode, the tip oscillates at or near its resonance frequency at a small distance above the surface, where long-range attractive forces such as van der Waals interactions dominate (Figure 3.7 b). Changes in oscillation amplitude, frequency, or phase are used to reconstruct the surface characteristics, while reducing mechanical damage of the sample.

Tapping mode

In tapping mode, or intermittent contact mode, the cantilever oscillates allowing the tip to periodically contact the surface, and the tip-sample interaction modifies the oscillation amplitude. The height image is obtained by adjusting the z-position to keep the oscillation amplitude constant during scanning (Figure 3.7 c). This mode is often used in polymer and biological samples characterization, since it allows to reduce lateral shear forces on the sample while maintaining good spatial resolution.

If operated in advanced modes, AFM can be used to probe mechanical, electrical, or magnetic. For example, force-distance spectroscopy enables the measurement of adhesion and elastic modulus, while conductive AFM and Kelvin probe force microscopy provide local electrical information.

For printed organic films such as PEDOT:PSS, AFM is frequently employed to evaluate roughness, domain structure, phase segregation, and film continuity, seen their importance in defining the material electronic and ionic transport properties.

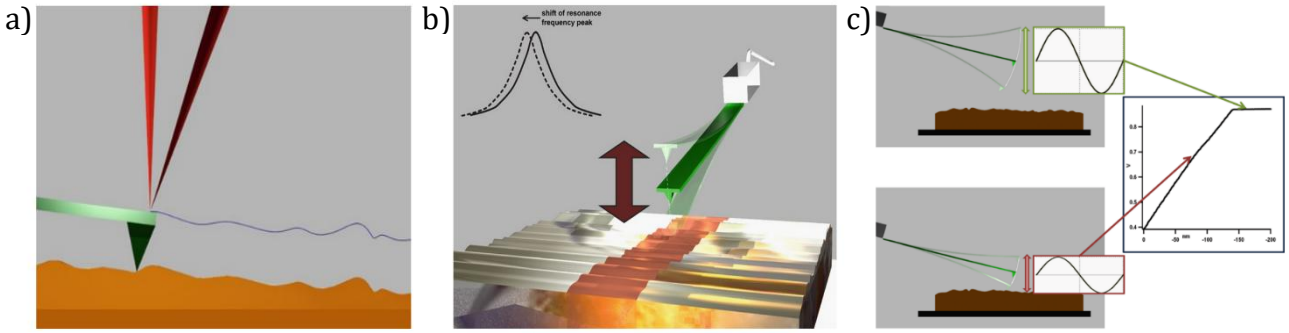

Figure 3.7 a) Schematic representation of the contact mode. Reprint from [206]. b) Schematic representation of the non-contact mode. The vibrating cantilever is close to the sample enough to sense the attractive forces from the surface. The feedback depends on the frequency shift in the resonance peak of the cantilever caused by the attractive forces acting on the tip. Reprint from [206]. c) Schematic representation of a cantilever operated in intermittent contact mode. The free oscillation amplitude decreases when the tip touches the sample surface at each cycle. Reprint from [206].

According to Hooke's law, the force F acting on the cantilever is proportional to its deflection δ through the spring constant *k*, as $F = k\delta$. For every operating mode, the cantilever spring constant must be known to obtain a quantitative output[207].

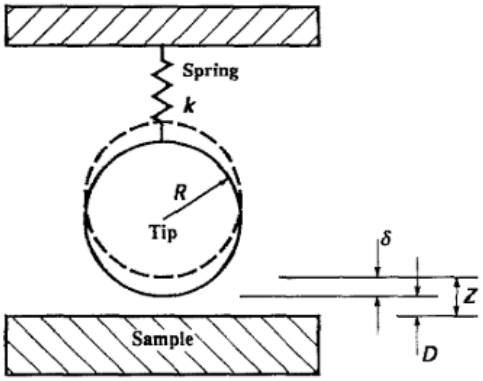

Figure 3.8 Model of an AFM cantilever-tip-sample system, where the tip is idealized as a sphere of radius *R*, held at a distance *D* from a sample by a spring of force constant *k*, modeling the cantilever. In case of interactions with the sample, the system experiences a deflection of *δ*. Reprint from [207].

Knowing that a harmonic oscillator in equilibrium with its surroundings will fluctuate in response to thermal noise, estimates of the spring constant can be extracted by thermally exciting the cantilever far from the sample, where its motion is due only to thermal fluctuations, and measuring the motion at frequencies near its resonant frequency[207]. Considering an oscillator with mass *m*, the Hamiltonian of such system, schematized in Figure 3.8, is

$$H = \frac{p^2}{2m} + \frac{1}{2} m {\omega_0}^2 q^2 \qquad 3.4$$

where *q* is the displacement of the oscillator, *p* is its momentum, and ω_0 is the resonant angular frequency of the system. According to the equipartition theorem, the average value of each quadratic term in the Hamiltonian is $k_B T/2$, where k_B is Boltzmann's constant and *T* is the temperature[207]. Being $\omega_0^2 = k/m$, the spring constant may be obtained from the mean-square spring displacement as

$$k = k_B T / \langle q^2 \rangle. \qquad 3.5$$

3.2 *In situ* characterization of inkjet-printed films

To study the relationship between electrical biasing and structural evolution in inkjet-printed PEDOT:PSS films, *in situ* Raman spectroscopy was performed during electrical operation of OECTs integrating inkjet-printed channel and gold gate.

Raman spectroscopy is a well-established tool for probing the vibrational fingerprints of conjugated polymers, providing information on backbone conformation and oxidation state In PEDOT:PSS, the most intense Raman bands are typically associated with the symmetric C=C stretching mode of the thiophene rings, usually observed around 1420-1450 cm^{-1}, and with the C-C inter-ring stretching. Previous works showed Raman peak shifts as a function of properties variations in polythiophene derivatives[196,197,200,208–212]. *In situ* Raman spectroscopy extends this approach by enabling real-time monitoring of vibrational changes under applied bias.

By analyzing inkjet-printed PEDOT:PSS integrated in OECTs, *in situ* Raman spectroscopy was used as a comparative tool with respect to literature studies and as a characterization technique to study the intrinsic structural and electrochemical behavior of inkjet-printed films. While previous studies mainly focused on the real-time evolution of PEDOT under bias, the present work examined in real time how channel modulation is affected by gates with different capacitance, as well as how the overlap of the channel with the source and drain electrodes influences the PEDOT electronic states.

3.2.1 Experimental

Following an established protocol for electrodes photolithographic patterning[212], 10 nm titanium adhesion layer and a 100 nm gold layer were deposited by electron beam evaporation (ULVAC EBX-14D) onto a microscopy glass slide. AZ® 1518 positive photoresist was spin coated on the wafer and exposed with a NEUTRONIX QUINTEL NXQ-4006 mask aligner. Development in AZ® 400 K developer diluted 1:3 in DI water was followed by wet chemical etching for titanium removal and for gold removal, so to obtain devices with channel length L = 100 μm and channel width W = 1 mm, and with gate diameter of 2.5 mm.

PEDOT:PSS films were deposited via inkjet printing on the channel, for the first device, and on channel and gate, for the second device, after filtering through a 0.22 μm syringe filter. The ink was prepared using 76% v/v Clevios PH1000, 19% v/v ethylene glycol, 4% v/v dodecylbenzenesulfonic acid (DBSA), and 1% v/v GOPS. Inkjet printing was performed using a Jetlab® 4 piezoelectric drop-on-demand system (MicroFab Technologies) equipped with a 50 μm

nozzle and setting a stage velocity of 25 mm/s, 1 μm distance from feature borders, and 40 μm drop spacing. Two layers were printed for each feature.

After printing, samples were annealed in an oven at 150 °C for 30 min.

PDMS chambers to be positioned on the devices to contain the electrolyte were fabricated via replica molding. A master mold was 3D printed using the OBJET30 Stratasys, and then cured in oven at 120°C overnight. PDMS precursors were mixed and poured in the mold. After degassing and baking at 90°C for 20 minutes, the replica was removed from the mold and washed in isopropanol.

A 3D printed holder for the glass slide was realized with the OBJET30 Stratasys. Spring probes were inserted into the holder, so to stably connect the gold tracks during the measure, creating a compact set up compatible with the Raman chamber and objectives (Figure 3.9).

Electrical characterization

Electrical measurements were carried out using a Keysight B2912A Precision Source/Measure Unit, after immersing channel and gate in an aqueous 0.1 M NaCl electrolyte solution. Transfer measurements were performed by sweeping the gate voltage between -0.6 V and 0.8 V at a constant drain voltage of -0.6 V.

Physical characterization

Raman spectroscopy was performed using a Renishaw inVia™ confocal Raman microscope using a 5X objective and an excitation wavelength of 785 nm. Each Raman spectrum was obtained by averaging four consecutive acquisitions of 20 s each, with the spectrometer grating centered at 1200 cm^{-1}. The Raman spectrum of a silicon sample was acquired as a reference. All spectra are offset with the reported silicon Raman peak (520 cm^{-1}).

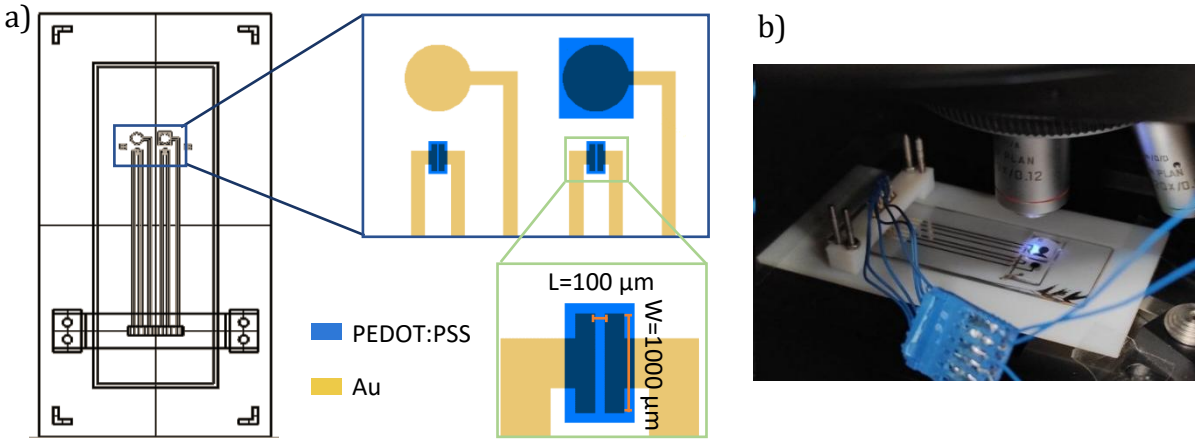

Figure 3.9 a) Schematic of the top view of the *in situ* Raman spectroscopy set up, comprising a 3D printed holder hosting the glass slide used as substrate for the analyzed devices. In the blue box, a magnification on channel and gate of the two devices. In the green box, a magnification on the channel. b) Picture of the measurement set up in the Raman microscope chamber.

3.2.2 Results

Figure 3.10b shows the *in situ* Raman spectra of the inkjet-printed PEDOT:PSS channel during OECT operation, with a bare gold gate electrode, acquired on the center of the channel.

Prior to the application of a gate potential, the Raman spectrum of the pristine PEDOT:PSS channel acquired in the center of the channel exhibits a dominant C_α=C_β symmetric stretching band centered around 1427 cm^{-1} (Figure 3.10 b) and a C_α-$C_{\alpha'}$ stretching band[213] of 1259 cm^{-1}. Upon application of a V_{DS} of -0.6 V and a potential of 0.5 V between source and the bare gold gate, the device starts to switch off due to cations injection in the channel and the drain current decreases in absolute value: in the Raman spectrum, the C_α=C_β band shifts to 1415 cm^{-1}. During 0.8 V application, the center of the peak reaches 1408 cm^{-1}, while the C_α-$C_{\alpha'}$ band center can be found at 1251 cm^{-1}, coherently with an increase in the neutral PEDOT fraction due to progressive entering of compensating ions. Upon application of negative bias (blue dotted line on the backward curve of the transfer plot in Figure 3.10 a), the main band shifts back to 1427 cm^{-1}, proving the reversibility of PEDOT:PSS oxidation state modulation.

To compare the modulation capabilities of the two types of gates, the Raman spectra of the channel modulated by a PEDOT:PSS-coated gate were also acquired. Considering that the printed PEDOT:PSS layer, having a thickness of about 800 nm, completely covers the gold gate, the final gate capacitance can be

assumed to be the capacitance of the printed PEDOT:PSS layer, while the underlying gold electrode mainly acts as a current collector. Considering a volumetric capacitance for PEDOT:PSS of 50 F/cm^3, taken as an intermediate value in the range of the estimated capacitance for PEDOT:PSS[214], and an area of the printed layer of 0.063 cm^2, the estimated gate capacitance for the coated gate is about 250 μF, far greater than the bare gold gate capacitance, estimated to be approximately 1.5 μF (0.05 cm^2 * 30 μF/cm^2). In OECTs, higher gate capacitance reduces voltage loss at the gate/electrolyte interface and enables more charge transfer to the channel, resulting in stronger electrochemical doping/dedoping[215].

Figure 3.10d shows how a PEDOT:PSS-coated gate is indeed more efficient in the electrochemical modulation of the channel: the center of the C_α=C_β stretching band during the application of a gate bias of 0.5 V is much closer to the band relative to the 0.8 V bias condition compared to the device with bare gold gate (Figure 3.10c). This is confirmed by the peak full width at half maximum (FWHM) values, whose narrowing is associated with the dominance of the neutral species upon dedoping, and vice versa, whose broadening depends on the presence of different charged states [216]. As reported in Table 3.2, the FWHM at the 0.5 V biasing condition of an OECT with a PEDOT:PSS-coated gate is smaller than the corresponding value in a bare gold gated OECT (Table 3.1), indicating faster and improved channel modulation. The drain current registered at the 0.5 V gate bias condition in the PEDOT:PSS-coated gate device had a magnitude of about 7.8 mA, while the corresponding current in the bare gate device was about 8.6 mA in magnitude, closer to its ON condition.

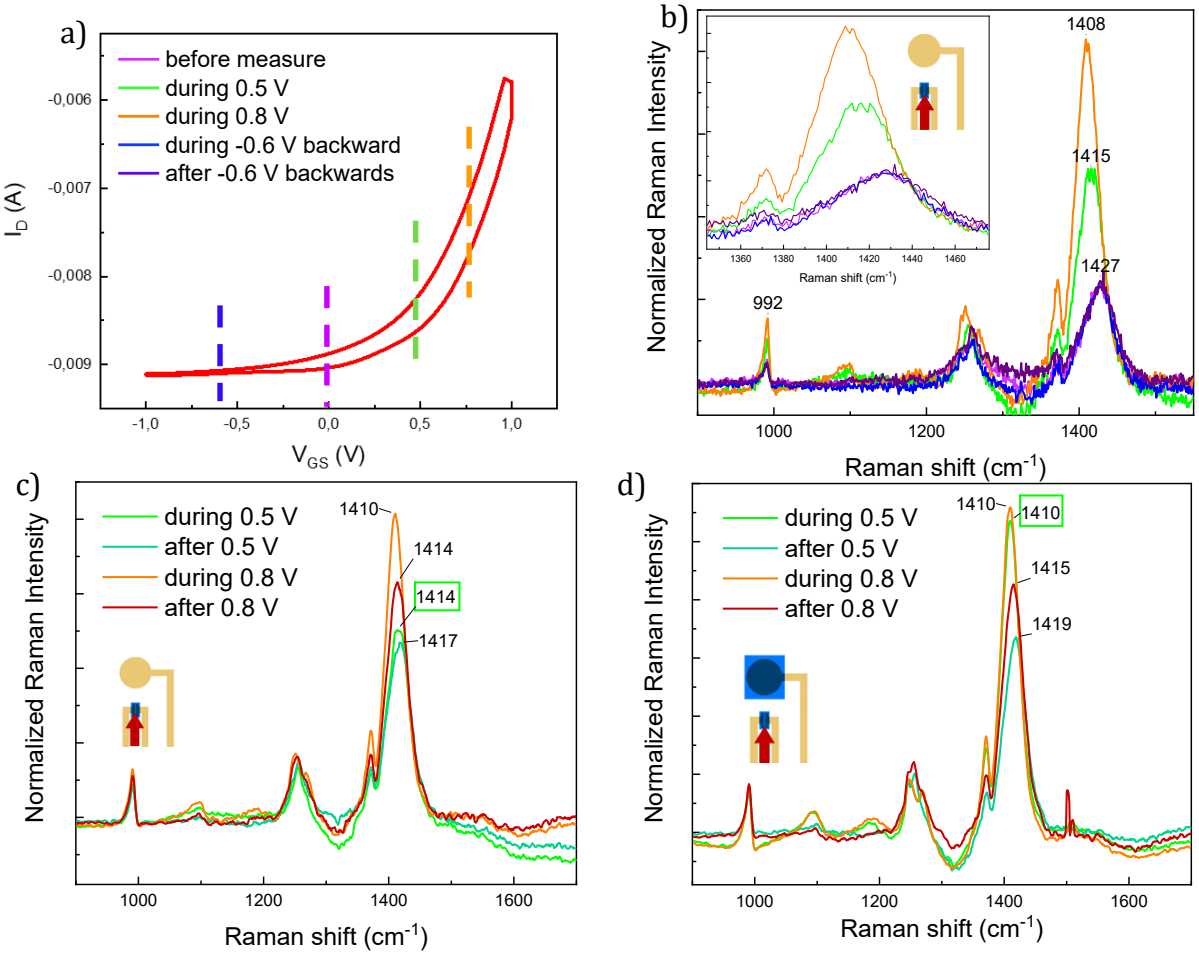

Figure 3.10 a) Transfer characteristics and b) Raman spectra of inkjet-printed PEDOT:PSS acquired at the center of the OECT channel on the glass substrate during operation of the device with bare gold gate. The inset (top left) shows an enlargement of the 1350-1480 cm^{-1} region. c) Raman spectra of inkjet-printed PEDOT:PSS acquired at the center of the OECT channel on the glass substrate during operation of the device with bare gold gate. d) Raman spectra of inkjet-printed PEDOT:PSS acquired at the center of the OECT channel on the glass substrate during operation of the device with PEDOT:PSS-coated gate.

Table 3.1 Peak position and FWHM values for different operation conditions of a device with bare gold gate.

Operation condition	Peak (cm^{-1})	FWHM (cm^{-1})
before measure	1427	45.5
during –0.6 V	1427	46.9
during 0.5 V	1414	46.7
during 0.8 V	1410	40.9

Table 3.2 Peak position and FWHM values for different operation conditions of a device with PEDOT:PSS-coated gate.

Operation condition	Peak (cm^{-1})	FWHM (cm^{-1})
before measure	1430	46.6
during –0.6 V	1445	48.7
during 0.5 V	1410	39.0
during 0.8 V	1410	38.2

Figures 3.11 a, b, c, d show the transfer curves and Raman spectra acquired on the source and drain electrodes of the device having PEDOT:PSS channel and PEDOT:PSS-covered gold gate. In the Raman spectrum of the pristine PEDOT:PSS channel acquired on the overlapping portion between PEDOT:PSS and source electrode (Figure 3.11 b), prior to the application of a gate potential, the C_α=C_β symmetric stretching band is centered around 1431 cm^{-1}. Upon application of a negative gate voltage, a clear shift of the C_α=C_β stretching band toward higher wavenumbers is observed. This is consistent with an increase in the fraction of oxidized PEDOT chains, as higher wavenumber positions are commonly associated with oxidized states [195], reflecting a bias-induced increase in the doped species population. When a positive gate voltage is applied, the C_α=C_β stretching band shifts toward lower wavenumbers, reaching approximately 1411 cm^{-1}, corresponding to an increase in the reduced PEDOT fraction. It can be observed how the initial peak position at 1431 cm^{-1}, when compared with the peaks that followed electrical bias, can indicate that both oxidized and neutral PEDOT species coexist within the pristine channel. [211,217]. The Raman spectra of the PEDOT:PSS channel acquired on the drain electrode during the 0.5 V and the 0.8 V gate bias (Figure 3.11 d) show bands centered on slightly lower wavenumbers compared to the ones acquired on source. This could be explained by the fact that the negative drain-source voltage drives both holes and cations toward the drain electrode[218]. Holes are collected by the drain, giving rise to the drain current, while cations accumulate capacitively at the interface,

creating localized enhanced dedoping conditions for the PEDOT overlapped with the drain electrode.

Other significant bands are found around 699 cm^{-1}, which can be associated with the C-S-C thiophene ring deformation, and at 990 cm^{-1}, usually attributed to the oxyethylene ring deformation[208,210,219].

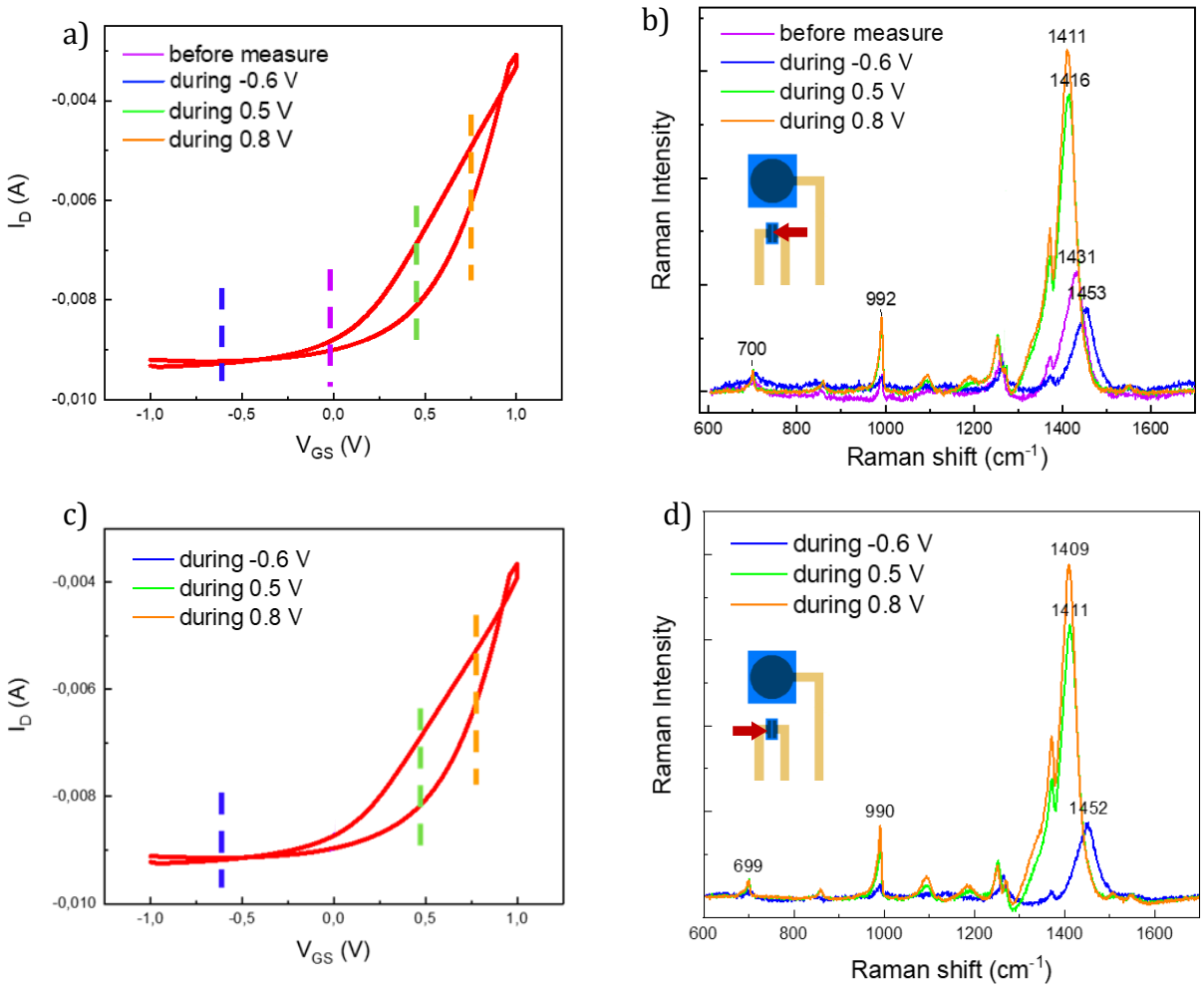

Figure 3.11 a) Transfer characteristics and b) Raman spectra of inkjet-printed PEDOT:PSS acquired on the gold source electrode of the OECT, acquired during operation of the device with PEDOT:PSS-coated gate. c) Transfer characteristics and d) Raman spectra of inkjet-printed PEDOT:PSS acquired on the gold drain electrode of the OECT, acquired during operation of the device with PEDOT:PSS-coated gate.

In Figure 3.12, the Raman spectra of the printed conducting polymer on the gate electrode can be observed. While metal gates such as gold and Ag/AgCl can be assumed as ideally polarizable, with no faradaic reactions occurring at their surface, PEDOT:PSS gates are subjected to redox reactions as well as the channel. However, thanks to its volumetric capacitance, the PEDOT:PSS coating on the gate also contributes to device operation by increasing the capacitance of the electrode, causing increased drain current modulation. As observed in Figure 3.12a, the transconductance obtained from the transfer characteristics of the device with PEDOT:PSS on the gate reaches indeed a higher maximum value compared to the bare-gate-device, and its peak corresponds to a lower gate potential, indicating a more efficient gating by means of the printed PEDOT:PSS. Nonetheless, bias application at the gate electrode causes reduction or oxidation[220] of the conducting polymer layer on top, which can be observed in Figure 3.12b. Upon application of bias at the gate, the C_α=C_β stretching band shifts in the opposite direction compared to what was observed on the channel. While negative gate potentials cause a red shift, due to PEDOT reduction, positive bias determines a small but progressive blue shift caused by the increase of oxidized PEDOT fraction, characterized by shorter effective conjugation length[211,220].

The reported results share a common tendency in the reduction of band intensity in correspondence of shifts towards higher wavenumbers. In conjugated polymers, vibrations along the backbone, especially C=C symmetric stretching modes, are typically intense because they strongly affect the delocalized π-electron density. Assuming laser power, focusing conditions, and detector sensitivity to be constant during the experiment, reductions in bands intensity can be in part attributed to benzoid-to-quinoid transitions and to changes in electronic structure that affect polarizability, as previously reported[211].

For PEDOT, the oxidized state is commonly associated with increased quinoid character, while the neutral state tends to recover a more benzoid-like configuration[221–223]. However, the interpretation of Raman shifts in PEDOT:PSS is not entirely uniform across the literature. Several studies report that increased oxidation, and therefore greater fraction of quinoid species, lead to shifts of the main C=C stretching band toward higher wavenumbers[202,211]. Other works instead observe shifts toward lower wavenumbers with changes from benzoid to quinoid form due to loss in π-conjugation, assigning shifts to the blue to the ground state of PEDOT[224,225]. These apparently contradictory results arise from the complex interplay between oxidation state, chain-chain interactions, resonance effects under different excitation wavelengths, and other mechanisms that shorten the conjugation length[195]. Overall, it should be considered that the benzoid-quinoid transition is not the sole phenomenon giving rise to Raman shifts.

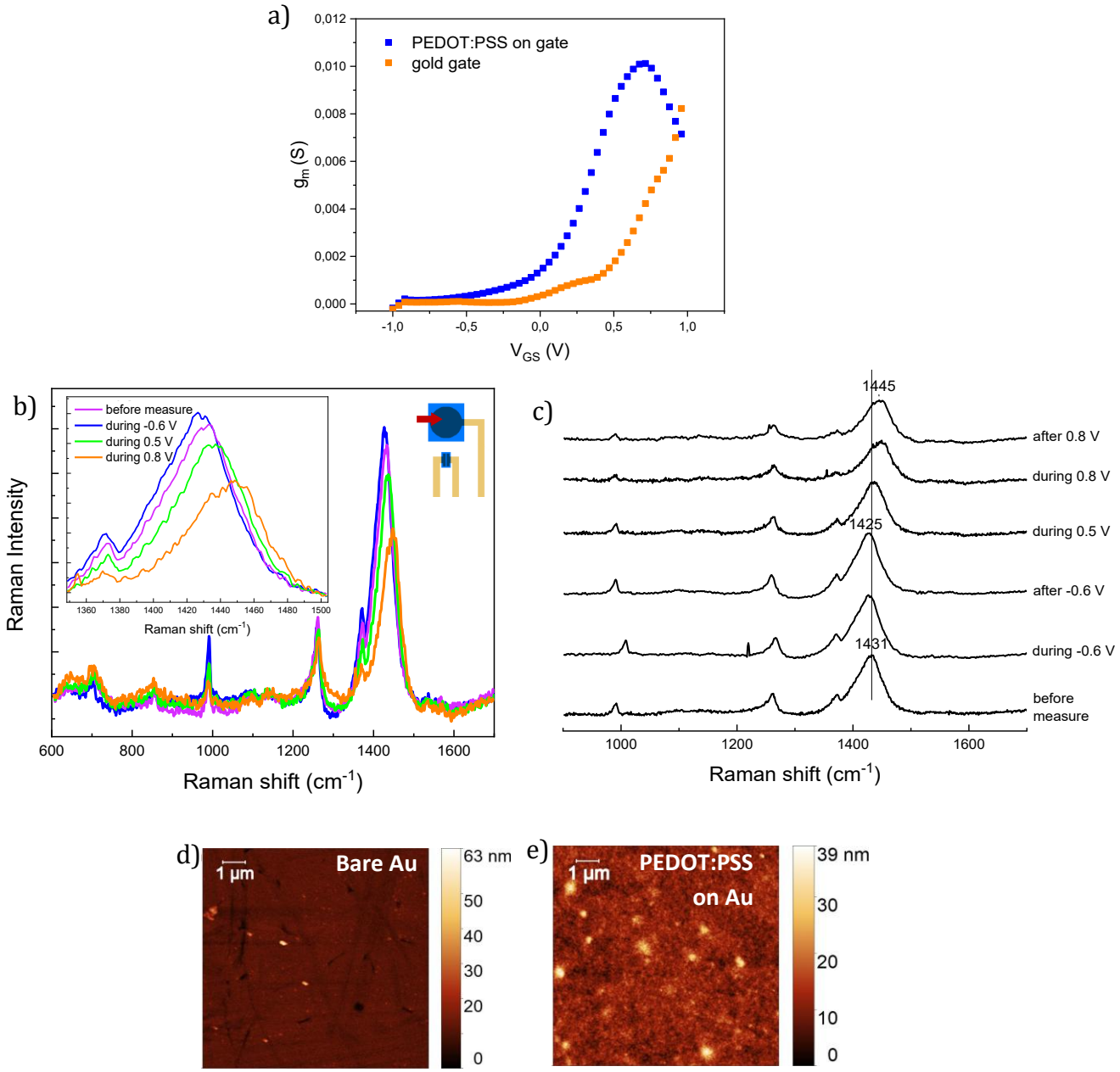

Figure 3.12 a) Transconductance obtained from the transfer curves of the OECT with a bare gold gate electrode (orange points) and with PEDOT:PSS deposited on the gate electrode (blue points). b) Raman spectra of inkjet-printed PEDOT:PSS deposited on the gold gate electrode of the OECT, acquired during device operation. The inset (top left) shows an enlargement of the 1380-1500 cm^{-1} region. c) Stacked Raman spectra of the PEDOT:PSS layer on the gold gate, comparing acquisitions performed during and after electrical bias. d, e) AFM topography images of the bare gold gate (d) and of the gate after inkjet printing of two PEDOT:PSS layers (e).

In figure 3.13, the Raman spectra of inkjet-printed PEDOT:PSS channels on cellulose are reported. While the Raman spectrum of pristine PEDOT:PSS exhibits a C=C symmetric stretching band around 1430 cm^{-1}, consistent with the position of pristine PEDOT C=C band observed on a glass substrate, the spectrum recorded from the channel after several OECT operating cycles displays the main band at approximately 1412 cm^{-1}, accompanied by a reduction of intensity. Shifts toward lower wavenumbers and decrease in the intensity of the characteristic C=C symmetric stretching band of the thiophene ring have been previously associated with increased structural disorder, partial loss of conjugation, and reduced effective conjugation length along the backbone[91,211,226]. The band relative to the "after measure" condition can therefore be interpreted as an indication of residual dedoping or as a sign of degradation of PEDOT:PSS after several cycles of measure. Moreover, the porous paper substrate may contribute to residual dedoping, as its structure can facilitate ions access while hindering their extraction from the PEDOT:PSS infiltrated within the pores, thus affecting the fraction of dedoped PEDOT.

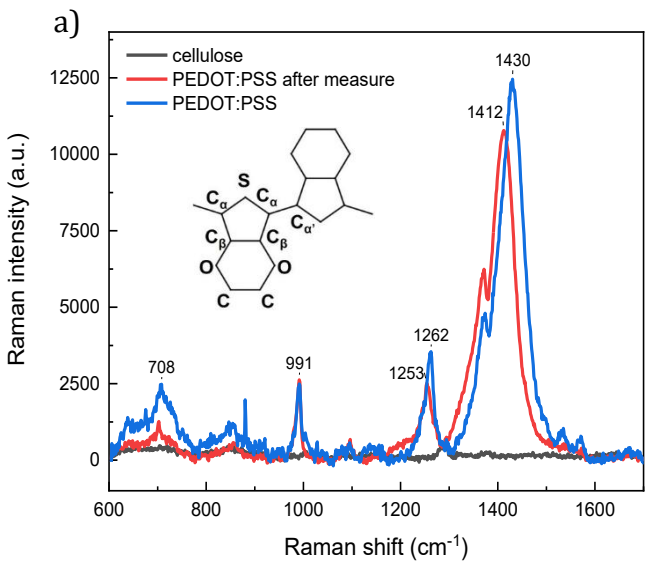

Figure 3.13 a) Raman spectra of inkjet-printed PEDOT:PSS channel deposited on nitrocellulose. The blue curve corresponds to pristine printed film, while the red curve corresponds to the PEDOT:PSS channel after several operation cycles of the cellulose-based OECT. The inset showing PEDOT structure was reproduced from [208].

3.3 Morphological comparison of printed films

In this section, a comparison of organic films deposited by different techniques is presented, with the aim of studying how morphological variations affect the electrical behavior of the material and the performance of the devices in which the films are integrated[140].

Inkjet printing and aerosol jet printing are investigated as alternative rapid prototyping approaches for the fabrication of PEDOT:PSS-based OECT channels. These techniques have gained increasing relevance in organic electronics due to their maskless workflow, compatibility with various substrates, and potential scalability. However, their different droplet formation mechanisms can lead to variations in roughness, thickness uniformity, and domain distribution, which in turn affect material performances by influencing charge transport pathways and film percolation [227–229]. To assess these morphological differences, atomic force microscopy was employed to analyze surface topography, which, together with electrical characterization of the fabricated devices, confirmed a dependence of OECT performance on the channel deposition technique.

3.3.1 Experimental

Following an established protocol for electrodes photolithographic patterning[212], 10 nm titanium adhesion layer and a 100 nm gold layer were deposited by electron beam evaporation (ULVAC EBX-14D) onto Si/SiO_2. Wafers. AZ® 1518 positive photoresist was spin coated on the wafer and exposed with a NEUTRONIX QUINTEL NXQ-4006 mask aligner. Development in AZ® 400 K developer diluted 1:3 in DI water was followed by wet chemical etching for titanium removal and for gold removal, so to obtain devices with channel length L = 10 μm and channel width W = 300 μm. An Al_2O_3 passivation layer (150 μm) was patterned using a lift-off process via exposure of AZ® 5214 image-reversal photoresist and development in AZ® 726 MIF developer. Lift-off was completed in dimethyl sulfoxide (DMSO)[140].

To promote adhesion of the PEDOT:PSS channel layer, a 22 mM GOPS solution in toluene:acetic acid (200:1 v/v) was spin-coated onto the chips at 4000 rpm for 60 s and thermally treated at 120 °C for 30 s.

PEDOT:PSS films were deposited on the fabricated channel, after filtering through a 0.22 μm syringe filter, either via inkjet printing (IJP), aerosol jet printing (AJP), or spin coating (SC). The ink consisted of 76% v/v Clevios PH1000,

19% v/v ethylene glycol, 4% v/v dodecylbenzenesulfonic acid (DBSA), and 1% v/v GOPS.

SC was performed at 1000 rpm for 30 s, and the deposition was repeated ten times to reach the desired thickness of 1.5 µm.

Inkjet printing was performed using a Jetlab® 4 piezoelectric drop-on-demand system (MicroFab Technologies) equipped with a 50 µm nozzle. Printing parameters were set to have a stage velocity of 25 mm/s, 1 µm distance from feature borders, and 40 µm drop spacing.

Aerosol jet printing was carried out using an Aerosol Jet® 200 Series system (Optomec) equipped with a 200 µm nozzle and ultrasonic atomizer. The deposition parameters were: stage velocity 2 mm/s, line overlap 20-30%, focusing ratio 1.4, sheath gas flow 35 sccm, and carrier gas flow 25 sccm. The substrate temperature during deposition was maintained at 60 °C, and the ultrasonic current was set to 0.5 mA. For AJP, the PEDOT:PSS ink was diluted 1:1 v/v with deionized water to obtain a viscosity within the range required for ultrasonic atomization (1-10 cP).

Printed samples were first dried on a hot plate at 120 °C for 15 min to remove residual solvents. All samples were subsequently annealed in an oven at 150 °C for 30 min.

Electrical characterization

Electrical measurements were carried out using a Keysight B2912A Precision Source/Measure Unit, employing an Ag/AgCl electrode as the gate reference immersed in an aqueous 0.1 M NaCl electrolyte solution. Transfer measurements were performed by sweeping the gate voltage between -0.2 V and 0.6 V at a constant drain voltage of VD = -0.2 V, recording three cycles for each measure.

Physical characterization

Surface topography was examined by atomic force microscopy using an Oxford Instruments MFP-3D Origin system. AFM imaging was conducted in tapping mode with AC160 cantilevers to obtain high-resolution height maps of the film surfaces.

3.3.2 Results

Comparing the transfer characteristics of the three types of samples, it can be observed how AJP devices exhibit the fastest switching behavior (Figure 3.14 b). Together with a high ON current, this results in the highest I_{ON}/I_{OFF} ratio

(3576.6 ± 921.2), which is approximately 6.5 times greater than that of IJP devices (542.4 ± 45.3)[140]. In contrast, spin-coated devices exhibited a considerably lower switching ratio of 55.2 ± 45.0[140] (Figure 3. 14 c).

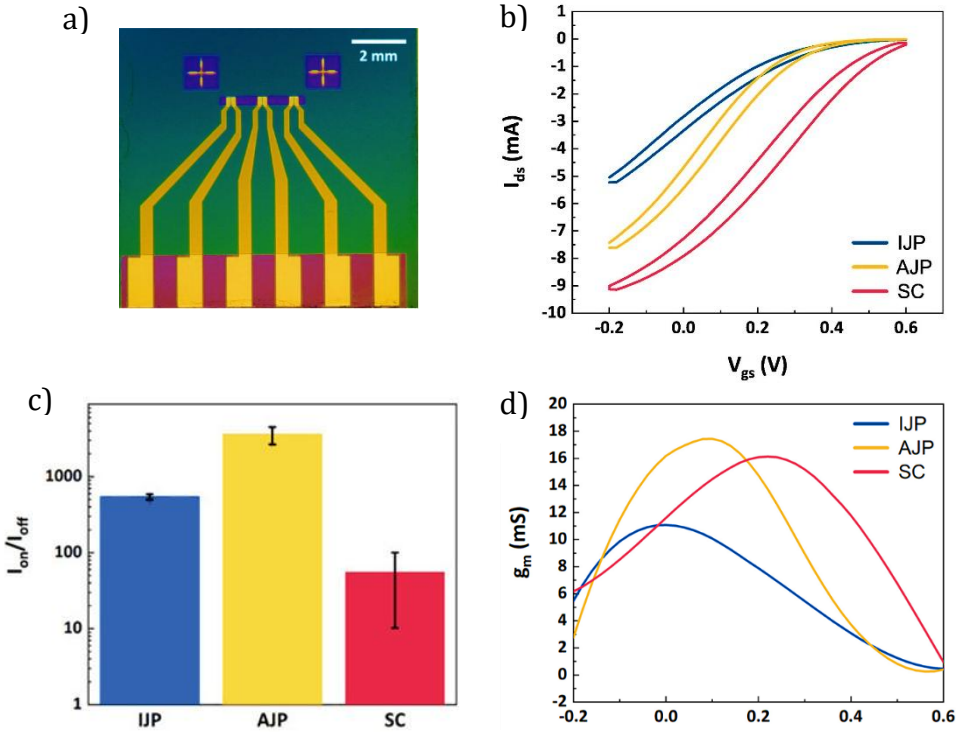

Figure 3.14 a) Optical microscopy image of the fabricated chip, comprising three pairs of source-drain electrodes, each constituting a device. b) Transfer characteristics for the three types of devices: with inkjet-printed PEDOT:PSS channel (IJP), with aerosol-jet-printed PEDOT:PSS channel (AJP), and with spin coated PEDOT:PSS channel (SC). Drain voltage was fixed at V_{DS} = -0.2 V. c) Plot of the calculated I_{on}/I_{off} ratios for the three types of devices. d) Transconductance curves obtained from the transfer characteristics. Reprinted from [140].

Transconductance was extrapolated from the transfer curves (Figure 3.14 d), and its maximum value, $g_{m,max}$, was normalized by the geometrical factor Wd/L, where d represents the film thickness and W and L correspond to the channel width and length, respectively. This normalization allowed to compare different channels independently form their geometrical variability. Among the investigated deposition methods, AJP devices exhibited the highest normalized transconductance, reaching 885.1 ± 51.5 S·nm, followed by SC devices (740.9 ± 79.6

S·nm)[140]. IJP devices displayed the lowest normalized peak transconductance, measured at 433.0 ± 36.7 S·nm[140]. In conclusion, although SC devices showed the highest ON current, AJP samples exhibited the greatest amplification capability.

To clarify the relationship between fabrication method, film structure, and electrical response, atomic force microscopy images were acquired, revealing clear morphological differences between films deposited by aerosol jet printing and inkjet printing (Figure 3.15). Topographic analysis showed that AJP films exhibit a rougher surface compared to IJP samples, with a root-mean-square roughness of approximately 40.1 nm for AJP and about 4.6 nm for IJP devices. Previous reports on spin-coated PEDOT:PSS layers, where the roughness is near 5 nm for film thicknesses above 70 nm, show comparable results to the values observed in the inkjet-printed samples[230].

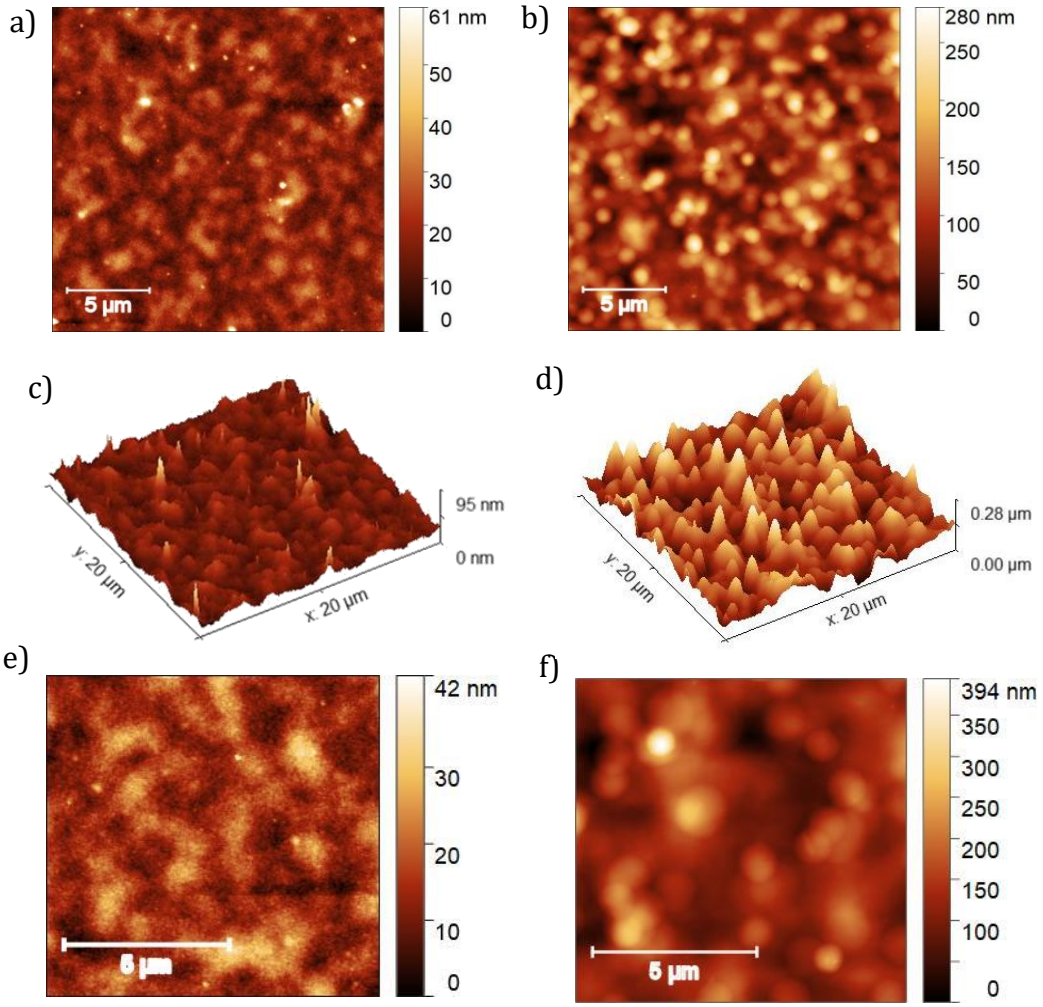

Figure 3.15 Topography images obtained via atomic force microscopy of inkjet-printed (a, c, e) and aerosol-jet-printed films (b, d, f). The images were processed using the software Gwyddion. Scan sizes are 20 µm (a, b, c, d), and 10 µm (e, f).

Phase contrast AFM images can provide information on the nanoscale distribution of PEDOT-rich and PSS-rich domains. Indeed, the phase lag between the cantilever oscillation and the driving signal originates from variations in energy dissipation occurring at the tip-sample interface, usually correlated to the materials components viscoelastic properties[231–233].

In tapping mode, the cantilever is driven close to its resonance frequency ω_0 and oscillates with a free amplitude A_0 when sufficiently distant from the surface. As the tip approaches the film, interactions with the sample reduce the oscillation amplitude to a setpoint value A, causing energy losses E_d during each oscillation cycle. The phase shift φ, also depending on the cantilever quality factor Q and its spring constant k, arises from this dissipative process[205,234].

$$E_d = \left(\sin\varphi - \left(\frac{A}{A_0}\right)\right)\frac{\pi k A A_0}{Q} \qquad 3.6$$

In heterogeneous or multi-component samples, differences in local mechanical response determine variations in energy dissipation, generating phase contrast. For polymer blends this contrast is commonly associated with phase separation between hard and soft regions[115,235].

Conventionally, a 90° phase shift between the excitation and the response is assigned when the free cantilever is excited at its fundamental resonance[236]. During image acquisition, small changes in the interaction regime between tip and sample could introduce great changes in the phase shift without necessarily corresponding to a significant variation of the material properties. For this reason, phase shift data are often converted into energy dissipation values using the expression that relates the phase lag to the energy lost by the cantilever during each oscillation cycle. Being related to the strength of tip-sample interactions, including viscoelastic losses, adhesion, and local mechanical response of the surface, the energy dissipation provides a more physically meaningful parameter than the phase angle alone.

Figure 3.16 shows topography images, phase contrast images, and energy dissipation maps, calculated from Equation 3.6 using amplitude and phase shift data acquired during 1 μm scans of IJP and AJP films, with Q = 530.27, k=33.58 N/m and A_0 = 24.5 nm. While the phase contrast image of the IJP sample (Figure 3.16 b) shows discrete, isolated regions within a matrix, the AJP film (Figure 3.16 e) displays phase patterns suggesting more elongated and oriented clusters. The interpretation of bright and dark contrast in AFM phase images has been inconsistent when distinguishing between hard and soft domains, as several works assigned bright regions to soft phases[232,233,235], while other studies

associated bright contrast to hard domains[237–240]. Concurrently, some authors found that phase contrast can be flipped when changing from moderate to hard tapping[235,237,238], coherently with the abovementioned dependency of the phase contrast on the tip-sample interaction regime and on the imaging conditions[235]. In this study, considering that A_0 = 24.5 nm, and considering that the tip does not strongly tap the surface, a mostly attractive regime can be assumed[236]. In this case, where the interaction is dominated by long-range forces such as van der Waals, capillary, and viscoelastic losses, materials that deform more easily or that have higher internal damping tend to dissipate more energy.

The energy dissipation map for the AJP sample (Figure 3.16 f) exhibits a clear contrast between a highly dissipative matrix, which can be assigned to the hydrophilic and softer PSS, and less dissipative domains, that could correspond to harder PEDOT enclosures having length of a few tens of nanometers[115,117]. These regions correspond to bright and dark contrast in the phase image, respectively (Figure 3.16 e). This phase segregation is less evident in the energy dissipation map of the IJP and the spin coated samples (Figure 3.16 c, i), where the less dissipative PEDOT is more finely dispersed in the PSS matrix. The energy profiles confirm the phase separation phenomenon indicated by the presence of two separate peaks in probability density (Figure 3.16 l).

Although several stiffer islands can be identified in the phase images, the dissipated energy map provides a more comprehensive description of the sample surface than the phase image alone.

From this analysis, it can be inferred that, compared to IJP, the AJP process not only contributes greatly to shape films morphology, but also influences PEDOT and PSS redistribution after annealing, favoring phase segregation and formation of oriented, highly conductive PEDOT crystals mediated by the conductivity enhancer ethylene glycol, which was present in the same amount in both IJP and AJP ink formulations[203,205,240].

Overall, the increased surface area of AJP films may facilitate ion penetration into the bulk of the channel, while the formation of oriented PEDOT domains may provide improved electronic pathways, while the PSS matrix provides percolation routes for ionic motion. In conclusion, the morphological features observed in AJP PEDOT:PSS films likely contribute to more efficient electrochemical doping of the channel, positively affecting the performance of the OECTs in which they are integrated.

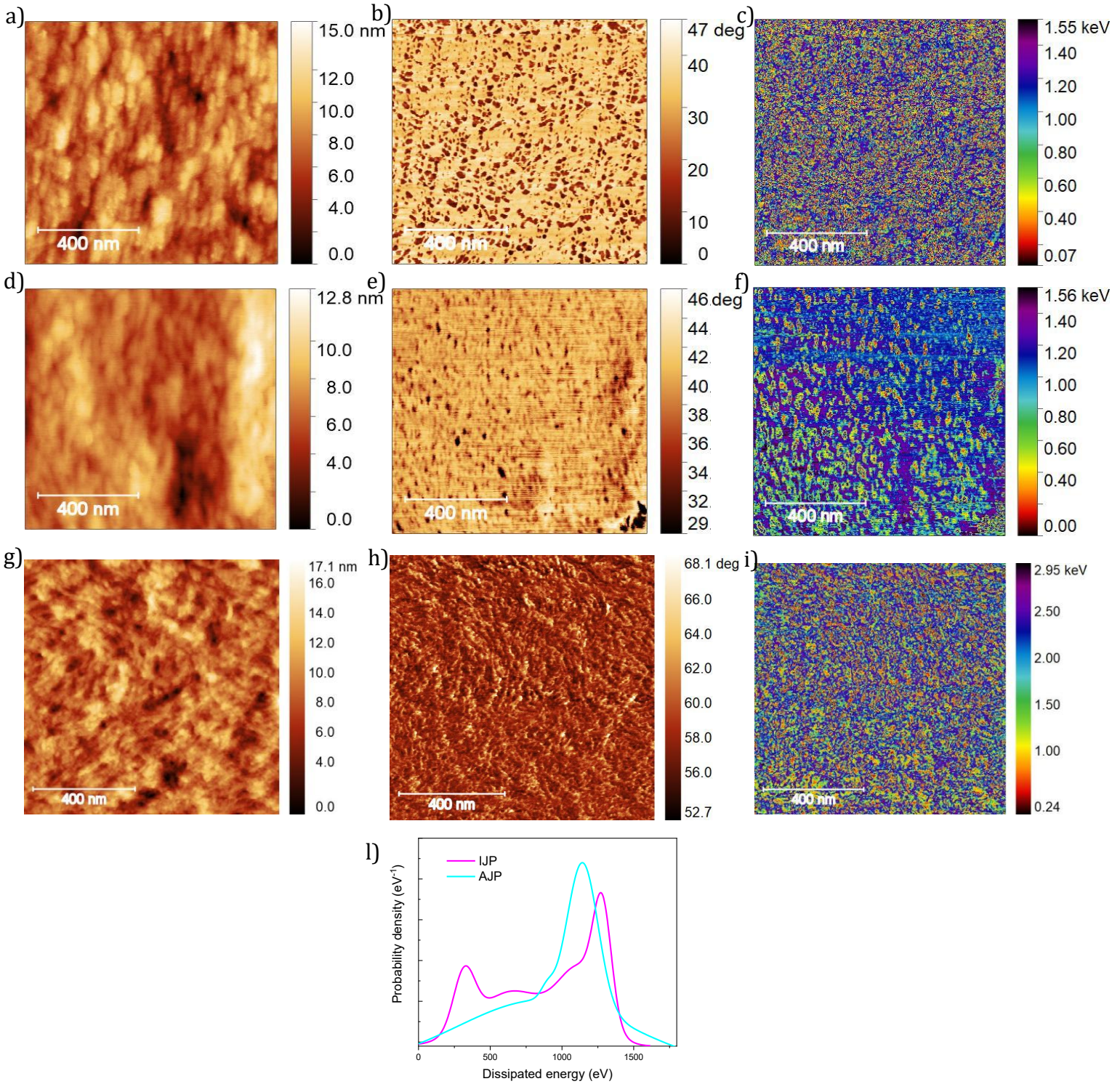

Figure 3.16 a, d, g) Topography images obtained via atomic force microscopy of inkjet-printed (a), aerosol-jet-printed films (d), and spin coated films (g) with a scan size of 1 µm. b, e, h) Phase images of inkjet-printed (b), aerosol-jet-printed films (e), and spin coated films (h) associated to the scans in a) and d), respectively. c, f, i) Energy loss maps calculated from measured signals according to Equation 3.6. l) Dissipated energy probability profiles of the AJP and IJP films.

1

Chapter 4

4 Printable OECTs on cellulose for POC sensing

Microfluidic technologies have played a key role in the evolution of point of care systems, enabling the manipulation of very small volumes of liquids and reducing reagent consumption. While traditionally lab on chip devices were mainly fabricated using silicon or elastomeric polymers such as PDMS, these approaches often involve complex processing steps and limited scalability. For this reason, porous substrates based on cellulose have attracted increasing attention as alternative platforms for portable diagnostics. Paper and nitrocellulose are inexpensive, lightweight, and biodegradable materials, and they intrinsically support fluid transport by capillary action, eliminating the need for external pumps.

Nitrocellulose membranes are widely used in LFAs, which represent one of the most successful examples of paper-based devices. Although LFAs are simple and robust, their sensitivity is often limited and the visual readout may be difficult to quantify, especially at low analyte concentration. For this reason, several studies have proposed the integration of electrochemical or electronic transducers with LFAs to obtain quantitative outputs and improved detection limits.

4.1 State of the art

One of the first demonstrations of an electrochemical lateral flow immunoassay was reported by Sinawang et al., who integrated a screen-printed gold electrode with a nitrocellulose strip for the detection of dengue NS1 antigen, showing that electrochemical readout could provide quantitative results within the same time scale of conventional LFAs[241]. Later works confirmed that electrochemical detection can significantly improve sensitivity, enabling the detection of clinically relevant biomarkers at concentrations below the visual limit of standard tests. For example, integrated electrochemical LFA platforms have been used for the detection of protein biomarkers, allergens, and bacterial targets[32,69,242,243]. In many cases, the electrochemical signal is obtained by measuring the current associated with redox reactions of mediators added during the assay (Figure 4.1a,b).

The growing interest in electronic LFAs has also motivated the exploration of organic and printed electronics as alternative transduction platforms.

Printed electrodes and conducting polymer devices have already been demonstrated on paper and flexible substrates[244]. As additive manufacturing methods advance, printing techniques such as screen printing, inkjet printing, aerosol jet printing, and dispense printing are accelerating the diffusion of organic transistors in sensing applications, allowing the direct deposition of conductive polymers, metallic inks, and dielectric layers on a wide range of substrates without the need for photolithography[142,245–248].

Dispense printing has recently developed from a simple direct-write strategy for PCB manufacturing into a convenient fabrication technique for flexible microelectronic devices and sensors[143,145,249]. Unlike inkjet or aerosol jet printing, which require low-viscosity inks and dedicated industrial equipment, dispense printers are usually compact bench-top systems operating by extrusion of highly viscous pastes through a nozzle, making it compatible with conductive silver inks, carbon pastes, polymer composites, and conducting polymer formulations. Vasquez *et al*. demonstrated high throughput prototyping of flexible electronic circuits using dispense printing of silver inks, producing functional devices on plastic substrates with rapid design iteration (Figure 4.1c)[145]. Similar results were reported in studies on dispense printing of silver flake inks on hydrophilic and hydrophobic surfaces, where the influence of substrate wettability on lines definition and electrical resistance was investigated, confirming that the technique can produce reliable conductive patterns on a wide range of materials, including flexible and porous supports[143]

Despite its lower resolution compared to inkjet and aerosol jet printing, dispense printing provides a high-throughput and cost-effective approach for the fabrication of organic electronic devices. In dispense printing, the larger nozzle diameters, designed to handle highly viscous pastes, enable the deposition of greater ink volumes per pass, resulting in faster film formation. This aspect is

particularly advantageous when working with porous substrates characterized by high absorption capacity. In such systems, inkjet printing typically requires a significantly higher number of deposited layers to achieve performance comparable to devices fabricated on smooth substrates. This is mainly due to the low-viscosity solvents employed in inkjet processes, which are rapidly absorbed by the porous matrix, leading to thinner and more dispersed films. A more detailed discussion of these aspects is provided in Appendix 1 of this thesis.

For these reasons, dispense printing is increasingly considered a practical approach for the realization of low-cost disposable sensors, paper-based electronics, and point-of-care devices, where simplicity of processing is more critical than ultra-high resolution[143,250–252].

Despite the progress achieved in printable organic electronics, the direct fabrication of OECTs on nitrocellulose membranes or on complete lateral flow strips had not been explored yet. The high porosity, roughness, and mechanical fragility of cellulose based materials can hinder the deposition of films and the control over device geometries. Nevertheless, integrating an organic transistor directly onto a nitrocellulose platform would allow the combination of a well-established capillary driven microfluidic platform with the amplification capability of OECTs, enabling quantitative readout of biochemical assays without the need for external microfluidic components.

In this chapter, the fabrication of a printable OECT on nitrocellulose is presented as a strategy to integrate an electronic sensing element into a cellulose based microfluidic platform[253]. The adopted architecture separates the sensing region from the active transistor area by means of hydrophobic barriers and a solid-state electrolyte layer, allowing the interaction with the analyte to occur

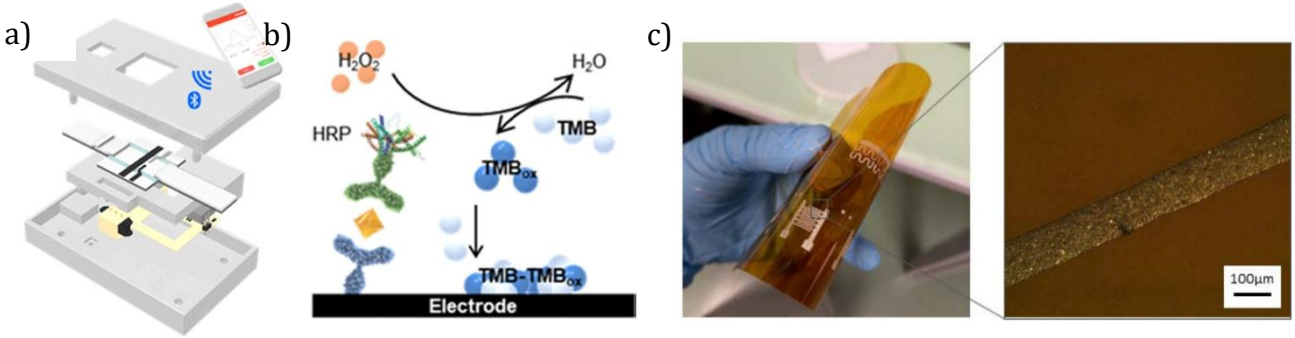

Figure 4.1 a) Schematic of an electrochemical LFA, able to connect to a smartphone for data transfer, and b) reaction mechanism using HRP-TMB as a redox couple for the detection of IL-6. Reprinted with permission from [242]. HRP, horseradish peroxidase. c) Interdigitated structures printed using the dispense printer Voltera V-One and a silver paste, on a flexible polyimide substrate. Reprinted from [145].

at an extended gate while preserving the stability of the PEDOT:PSS channel. This approach aims to combine the simplicity and low cost of LFAs with the sensitivity and signal amplification of organic transistors, providing a route toward scalable and affordable point of care sensing systems based on fully printable components.

4.2 Experimental

4.2.1 Materials

The silver ink Voltera Conductor 3 was purchased from Ventaja Tecnológica. PEDOT:PSS Clevios SV4 was purchased from Heraeus.

Kapton sheets, Whatman® FF170HP Din A nitrocellulose membrane sheets, N-isopropylacrylamide monomer, crosslinker N,N'-methylenebisacrylamide, photo-initiator 2-hydroxy-4'-(2-hydroxyethoxy)-2-methylpropiophenone, the ionic liquid 1-ethyl-3-methylimidazolium ethyl sulfate, dopamine hydrochloride, and all other chemicals were purchased from Sigma Aldrich and were used as received. Deionized water was obtained using a reverse osmosis (RO) purification system.

4.2.2 Solid state electrolyte (SSE) preparation

As reported by Weissbach et al.[131], the SSE precursor was prepared by mixing 1.0 mL of deionized water, 750.0 mg of N-isopropylacrylamide, 20.0 mg of crosslinker, 200.0 mg of photo-initiator, and 1.5 mL of ionic liquid. The precursor was stirred overnight at room temperature.

4.2.3 Device fabrication

After defining the device layout in CleWin, the silver electrodes and the PEDOT:PSS channel and gate structures were deposited using a Voltera V-One PCB printer. Source, drain, gate, and extended gate electrodes were first printed on the nitrocellulose substrate using a disposable nozzle with an internal diameter of 230 µm. The printed silver tracks were then thermally cured in an oven at 110 °C for 15 minutes to ensure proper conductivity and adhesion.

A dedicated cartridge was filled with PEDOT:PSS paste, and the printer settings were adjusted through a custom ink profile in the Voltera software in order to match the rheological properties of the material. The PEDOT:PSS features were printed in aligned printing mode directly on top of the silver layer using a 215 µm nozzle. Three successive layers were deposited to form the transistor channel, gate, and extended gate. The channel dimensions were L = 170 µm and W = 350 µm, the gate dimensions were L = 3500 µm and W = 2100 µm, and the extended gate dimensions were L = 5500 µm and W = 4000 µm. The distance between the channel and the gate was set to 0.5 mm (Figure 4.2).

After deposition, the samples were baked at 110 °C for 30 minutes to promote solvent evaporation and improve film stability. The silver interconnects were then passivated by depositing a 60 nm thick Al_2O_3 layer by electron beam evaporation using a Temescal FC-2000 system. The passivation layer was patterned through a custom Kapton mask produced by laser cutting (power 11%, frequency 1500 Hz), leaving the active areas exposed. Finally, 3 µL of SSE were drop-cast onto the channel and gate region inside the dry area, and the film was crosslinked by UV irradiation for 20 seconds.

The water-insoluble ink of a common permanent marker was used to define a hydrophobic barrier around the channel and gate, so to create a dry area unreachable by the liquid, thereby protecting the channel and gate from potential contamination by the sample.

4.2.4 Electrical and physical characterization

Electrical measurements were performed using a Keysight source/measure unit (SMU) under ambient conditions. Three cycles of transfer characteristics were acquired at a fixed drain voltage of -0.4 V, sweeping the voltage applied to the extended gate (VGS) from -0.6 V to 1.2 V, at a scan rate of 61.2 mV/s. Output characteristics were acquired at a gate voltage of -0.2 V, sweeping the drain voltage between 0 V and -0.6 V. The I_{ON}/I_{OFF} ratio and the transconductance of the OECTs were extracted from their transfer curves. g_m was normalized by dividing the values by the dimension factors Wd/L.

The scanning electron microscopy (SEM) images were acquired with a FEI Quanta 3D FEG dual-beam (SEM/FIB) using an accelerating voltage of 5 kV. A 50 nm Pt layer was sputtered on bare nitrocellulose before SEM imaging.

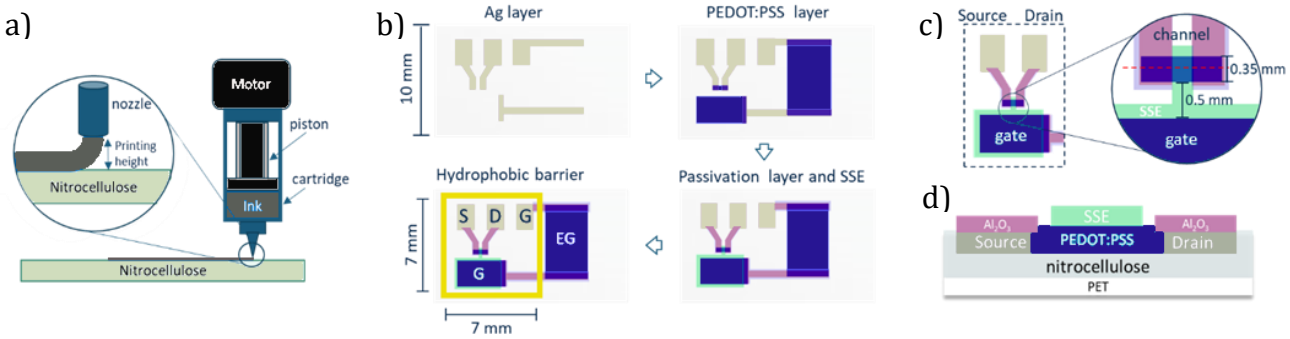

Figure 4.2 a) Overview of the dispense-printer modules. b) Schematics of the OECT fabrication steps on nitrocellulose: silver (grey) electrodes printing; PEDOT:PSS (blue) channel, gate and extended gate printing; Al_2O_3 (pink) and SSE (green) layers deposition; drawing of the hydrophobic barrier (yellow). The letters indicate source (S), drain (D), gate (G), and extended gate (EG). c) Detail of the OECT channel and its distance from the gate. The dashed red line indicates the cutting plane for the cross-sectional view shown in (d). d) Schematics of the cross-section of the OECT channel.

4.3 Results

4.3.1 Printing parameters optimization

In this section, the fabrication and characterization of the OECT on paper are presented. The device was directly printed on a piece of commercial nitrocellulose membrane with approximate dimensions of 1 × 1.5 cm^2 and a nominal thickness of about 200 µm (Figure 4.3). Nitrocellulose is widely used in rapid diagnostic tests because of its ability to immobilize biomolecules and its controlled porous structure, which supports efficient capillary flow. For this reason, it was selected as substrate with the goal of integrating an electronic sensing element into a passive microfluidic platform, while maintaining a simple and low-cost fabrication process for the transistor.

Device fabrication was carried out using a Voltera V-One dispensing printer, which allowed rapid and reproducible deposition of conductive inks without damaging the soft and porous substrate (Figure 4.3). The intrinsic roughness of nitrocellulose and its high porosity promoted good adhesion of both silver and PEDOT:PSS inks, making it unnecessary to introduce adhesion or planarization layers before printing. After thermal curing, the printed silver tracks showed a resistance per unit length of 3.71 ± 0.81 Ω/cm, which is comparable to the value

measured for the same ink printed on a smooth Kapton substrate (2.8 ± 0.38 Ω/cm), confirming that the porous support does not significantly degrade the electrical performance of the metal electrodes.

The channel, gate, and extended gate were arranged in a planar geometry and obtained by sequential deposition of three layers of PEDOT:PSS on top of the silver contacts (Figure5.2). The effective thickness of the conducting polymer inside the substrate was estimated from optical microscopy images of the device cross sections and resulted to be approximately 5 μm (Figure 4.3c). The cross-sectional analysis also revealed that the penetration of PEDOT:PSS into the membrane is not perfectly uniform. This behavior can be attributed to local variations in pore size and absorption properties of the cellulose matrix, which lead to different spreading and infiltration of the ink in different regions of the substrate. Since the morphology of the active layer strongly influences charge transport and ionic penetration, such inhomogeneity may contribute to the device-to-device variability observed in electrical measurements. One possible strategy to reduce this effect would be the deposition of preparative layer before printing PEDOT:PSS, in order to fill the pores and obtain a more uniform film. However, this solution would reduce the intrinsic microfluidic functionality of cellulose and could therefore be applied only in the dry region of the device, where capillary transport is not required.

The morphology of the bare nitrocellulose and of the printed PEDOT:PSS films was further investigated by SEM imaging (Figure 4.3d,e,f). The pristine substrate shows a fibrous network with pore diameters of the order of 10 μm, which allows liquid transport through the membrane (Figure 4.3d). After deposition of the first PEDOT:PSS layer, the polymer appears as a thin coating surrounding the cellulose fibers (Figure 4.3e), while the successive layers progressively fill the empty spaces and form a more continuous and interconnected conducting network (Figure 4.3f).

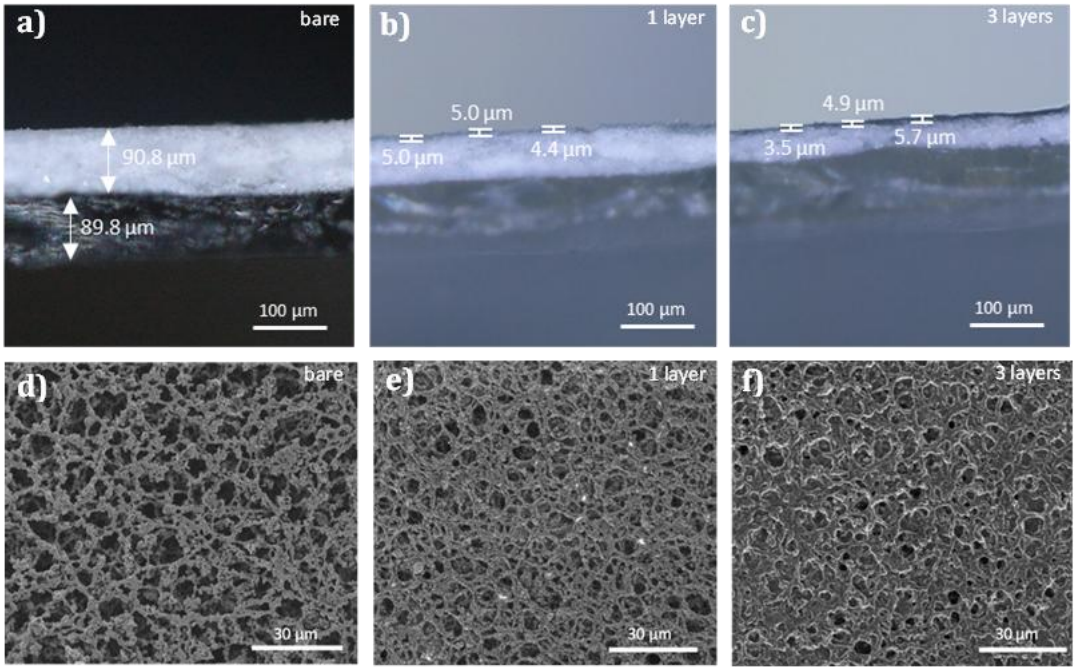

Figure 4.3 Top row: microscopy images of cross-sections of a) bare nitrocellulose, with its PET backing layer, b) one layer and c) three layers of PEDOT:PSS printed on nitrocellulose. The scale bar is 100 µm. Bottom row: SEM images of the surface of d) nitrocellulose metallized by 50 nm of sputtered Platinum, e) one layer and f) three layers of PEDOT:PSS printed on nitrocellulose. The scale bar is 30 µm.

This evolution of the film structure is consistent with the electrical characterization of the printed layers. The resistance of PEDOT:PSS tracks printed with one, two, and three layers was measured, showing a progressive increase in conductivity as the number of deposited layers increases (Table 4.1). Transfer characteristics of the transistors confirmed that devices fabricated with three PEDOT:PSS layers exhibit the highest transconductance (Figure 4.4), in agreement with previous reports on OECTs, where thicker channels generally provide larger volumetric capacitance and higher amplification. The final number of printed layers was therefore chosen as a compromise between high transconductance and acceptable switching speed, since thicker films, although more conductive, typically lead to slower response due to longer ionic diffusion paths[129,215].

Table 4.1 Resistance values of 1 layer, 2 layers and 3 layers of printed PEDOT:PSS channel and extended gate.

	1 layer	2 layers	3 layers
Channel	257 ± 83 Ω	82 ± 11 Ω	29 ± 3 Ω
Extended gate	10 ± 2 kΩ	6.6 ± 2.8 kΩ	0.9 ± 0.2 kΩ

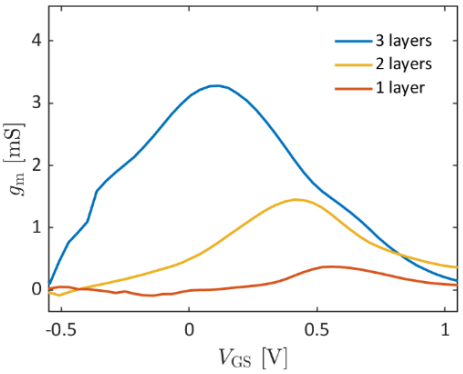

Figure 4.4 Transconductance of devices with 1 layer, 2 layers and 3 layers of printed PEDOT:PSS channel, gate, and extended gate.

4.3.2 Electrical stability

After deposition of the PEDOT:PSS layers, the printed silver tracks were passivated in order to avoid direct contact with the electrolyte and prevent degradation of the metal during operation. Aluminum oxide was selected as passivation material because it can be deposited uniformly at low thickness, is compatible with the nitrocellulose substrate, and can be patterned through a scalable electron-beam evaporation process. A Kapton foil was laser-cut to obtain a custom shadow mask, which was aligned on top of the printed devices to allow selective deposition of a 70 nm thick Al_2O_3 layer only on the electrode regions (Figure 4.2).

In electrolyte-gated biosensing transistors, contamination of the channel by the liquid sample is commonly prevented using microfluidic systems that confine the flow in dedicated channels[45,48]. An alternative approach consists in exploiting paper as a self-contained microfluidic platform, where liquid transport occurs by capillarity without external actuation. When combined with suitable surface treatments, paper can be patterned to obtain separated flow regions, providing a simple alternative to PDMS-based microfluidics. In the past, wax printing was widely used to create hydrophobic barriers on cellulose, but the

progressive disappearance of solid-ink printers has encouraged the development of simpler patterning methods[72,73]. In the platform described in this chapter, a standard permanent marker was used to draw a hydrophobic boundary that separates the extended gate from the channel and gate areas (Figure 4.2), following a low-cost approach. Results obtained with alternative materials for the hydrophobic barrier are reported in Appendix 2.

Inside the dry region defined by the permanent mark barrier, electrical coupling between gate and channel was ensured by the deposition of an SSE layer. This configuration isolates the channel from the liquid sample flowing through the nitrocellulose strip, preventing undesired interactions with the analyte while keeping the sensing region accessible. In addition, the localized deposition of the SSE reduces the exposure of the silver electrodes to the liquid phase, improving the stability of the electrical response.

The effectiveness of this configuration was evaluated by comparing device operation using 100 mM NaCl delivered through the strip with and without the hydrophobic barrier and the SSE (Figure 4.5). The transfer curves obtained in the two conditions show that the presence of the SSE greatly improves the stability of the device (Figure 4.5a). When only NaCl solution is used, the liquid spreads throughout the membrane and reaches the contact pads, leading to oxidation of the non-passivated silver and progressive degradation of the electrical response. In contrast, when the dry and wet regions are separated and the electrolyte is confined locally, the interaction between the solution and the metal contacts is minimized, resulting in a more stable behavior. To further evaluate the electrical stability, transfer characteristics were recorded for fifteen consecutive cycles in the presence of both the barrier and the SSE (Figure 4.5b). The variation per cycle was approximately 0.3% for the ON current and 0.5% for the OFF current, and after fifteen cycles the ON current remained about 95.7% of its initial value, in agreement with stability values reported for similar devices in the literature[254,255].

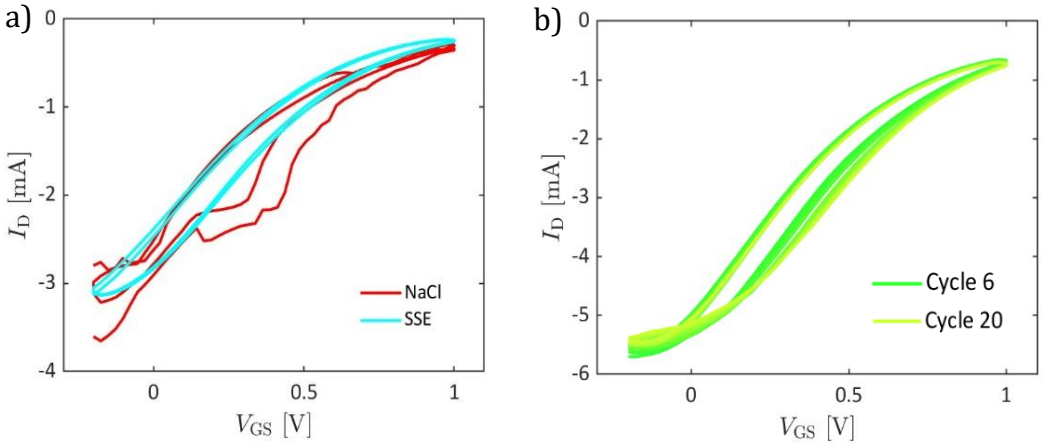

Figure 4.5 a) Comparison of three consecutive transfer curves recorded for a nitrocellulose based OECT at V_{DS} = -0.4 V, measured using either an SSE layer (blue curves) or a 100 mM NaCl solution (red curves) as the electrolyte. b) Device stability over 15 cycles of measures.

Long-term stability of the device components was also investigated under ambient storage conditions. The resistance of both the channel and the extended gate was measured six weeks after fabrication, showing no significant variation, indicating that the printed silver and PEDOT:PSS layers remain stable over time (Table 4.2). The hand-drawn hydrophobic barriers also preserved their functionality, effectively preventing liquid penetration in the dry region even after prolonged storage (Figure 4.6). However, the porous nature of cellulose gradually removes liquid from the SSE through capillary absorption, so that several hours after deposition the device can only operate in the ON state and cannot be fully switched off. This effect suggests that the introduction of a preparatory insulating layer in the dry region, able to partially fill the pores before electrolyte deposition, could improve long-term stability, although such treatment should be limited to the dry area to preserve the microfluidic properties of the strip.

Table 4.2. Resistance values for 3 layers of printed PEDOT:PSS channel and extended gate over time.

3 layers	t=0	t=2 weeks	t=6 weeks
Channel	29 ± 3 Ω	31 ± 4 Ω	35 ± 6 Ω
Extended gate	0.9 ± 0.2 kΩ	0.9 ± 0.2 kΩ	1 ± 0.1 kΩ

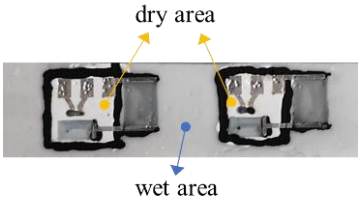

Figure 4.6 Picture of two printed devices, taken 6 weeks after fabrication. The nitrocellulose substrate was soaked with water to assess the stability and function of the hydrophobic barriers, which had been drawn with a black permanent marker immediately after printing.

4.3.3 OECT characterization

In the adopted wet-dry architecture, when a positive gate voltage is applied at the PEDOT:PSS extended gate in the wet zone, which is electrically connected to the gate in the dry zone, the channel OSC is reduced upon the injection of $[EMIM]^+$ ions from the ionic liquid contained in the SSE layer, a process facilitated by the presence of water in the matrix.

Electrical characterization was carried out by measuring transfer and output characteristics at a scan rate of 61.2 mV/s after depositing 50 µL of a 100 mM NaCl solution on the nitrocellulose strip before each measurement, allowing the liquid to reach the extended gate by capillary flow. From the transfer curves, the transconductance was calculated as the derivative of the drain current with respect to the gate voltage (Figure 4.7b). Since transconductance depends on the device geometry, the maximum value was normalized by the factor $d \cdot W/L$, where d is the thickness of the PEDOT:PSS layer inside the membrane and W and L are the channel width and length. After normalization, the maximum transconductance was found to be 95.9 ± 13.3 S·nm. The ON/OFF ratio, defined as the ratio between the absolute current at V_{GS} = -0.6 V and at V_{GS} = 1.2 V, was on the order of 10^2, comparable with values reported for similar printed OECTs.

To verify the compatibility of the device with lateral-flow operation, the influence of the distance between the sample deposition point and the extended gate was investigated, considering that in a typical strip the liquid travels several centimeters before reaching the sensing zone. Measurements performed by dropping the NaCl solution at distances of 0.5 cm and 1.5 cm from the extended gate showed only minor variations in the maximum transconductance, indicating that the capillary transport does not significantly affect the device response, although a slight dilution effect is observed for longer travel distances (Figure 4.7d).

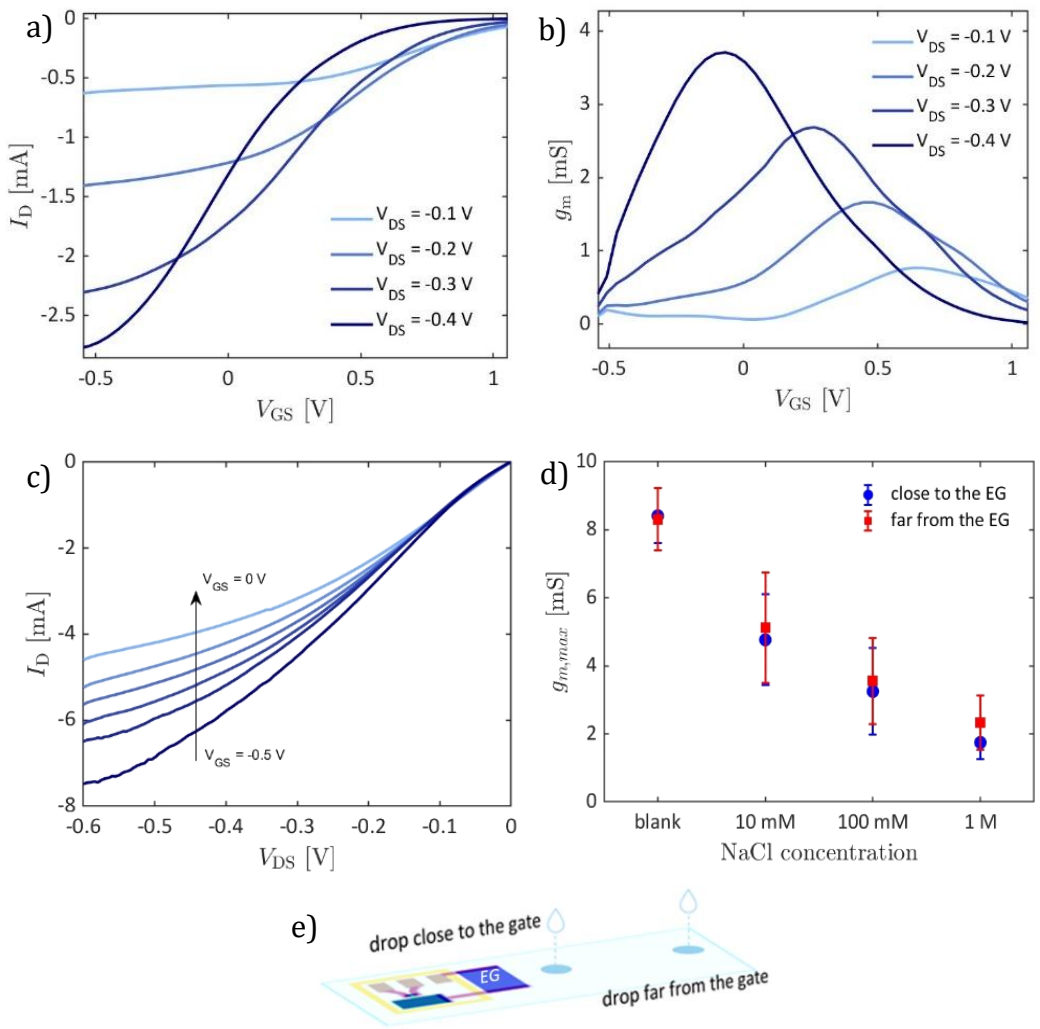

Figure 4.7 a) Transfer characteristics and b) corresponding transconductance of the device measured at different drain-source voltages, using an SSE layer on the channel and gate, while a drop of 100 mM NaCl solution was applied on the extended gate. c) Output characteristics of the same device recorded at different gate voltages. d) Comparison of the averaged maximum transconductance obtained from three devices when 50 µL of NaCl solution at different concentrations were deposited on the nitrocellulose strip at a distance of 0.5 cm (near) or 1.5 cm (far) from the extended gate. e) Schematic representation of the OECT printed on the nitrocellulose strip, illustrating the different positions used for sample deposition before the measurement.

4.3.4 Dopamine sensing

The sensing capability of the paper based OECT was evaluated using dopamine as model analyte. Dopamine (DA) is a neurotransmitter whose concentration in physiological fluids is typically in the nanomolar range. Recent studies have correlated altered dopamine levels to schizophrenia, Parkinson's disease, and attention-deficit hyperactivity disorder (ADHD) driving interest towards the development of highly sensitive dopamine sensors[256–258]. DA is also commonly used to test the performance of OECT-based sensors because it undergoes electrochemical oxidation under applied bias, allowing to detect electrical changes associated with the analyte concentration.

In the experiments, 50 µL of DA solution prepared in 100 mM NaCl were dropped at the far end of the strip, and transfer curves were recorded at a scan rate of 61.2 mV/s once the liquid reached the extended gate. After an initial stabilization period of approximately 5 minutes, the device response was evaluated by extracting the I_{ON}/I_{OFF} ratio and the maximum transconductance at different concentrations (Figure 4.8).

When a gate voltage is applied, DA is oxidized to dopaquinone, producing electrons and protons that modify the electrical potential at the extended gate. This change affects the effective voltage applied to the transistor, producing a variation in the drain current. Increasing DA concentration produced a progressive decrease in the I_{ON}/I_{OFF} ratio and in maximum transconductance, which can be attributed to progressive dedoping of the PEDOT:PSS extended gate caused by the reaction products of DA oxidation. The decrease in the doped fraction of PEDOT:PSS in the extended gate likely reduces the gating efficiency, resulting in a progressively lower peak in transconductance. The calibration curve obtained from the maximum transconductance values (Figure 4.8e) gave a limit of detection (LOD) of 0.01 mM, calculated using the 3σ method[259].

Additional measurements were performed in the presence of uric acid (UA) as interfering species. The potential corresponding to the transconductance maximum was shifted to higher values compared to DA, consistent with the higher oxidation potential of UA. However, when both molecules were present simultaneously, the device did not show clearly separated responses, indicating that in the present configuration the sensor is not selective.

Selectivity could be enhanced by decreasing the gate-voltage scan rate during transfer measurements. In the present work, a scan rate of 61.2 mV s^{-1} was selected as a compromise between analysis time and sensing performance, with the aim of maintaining a rapid assay compatible with point-of-care testing. Lower scan rates would provide additional time for ion transport and electrochemical equilibration within the PEDOT:PSS channel, increasing current modulation and improving signal resolution. Previous studies have shown that

slower voltage sweeps can enhance selectivity by allowing transconductance peaks associated with different electroactive species to be resolved within the same sample[260]. Although this would increase the measurement time by some minutes, the resulting improvements in sensitivity and specificity could

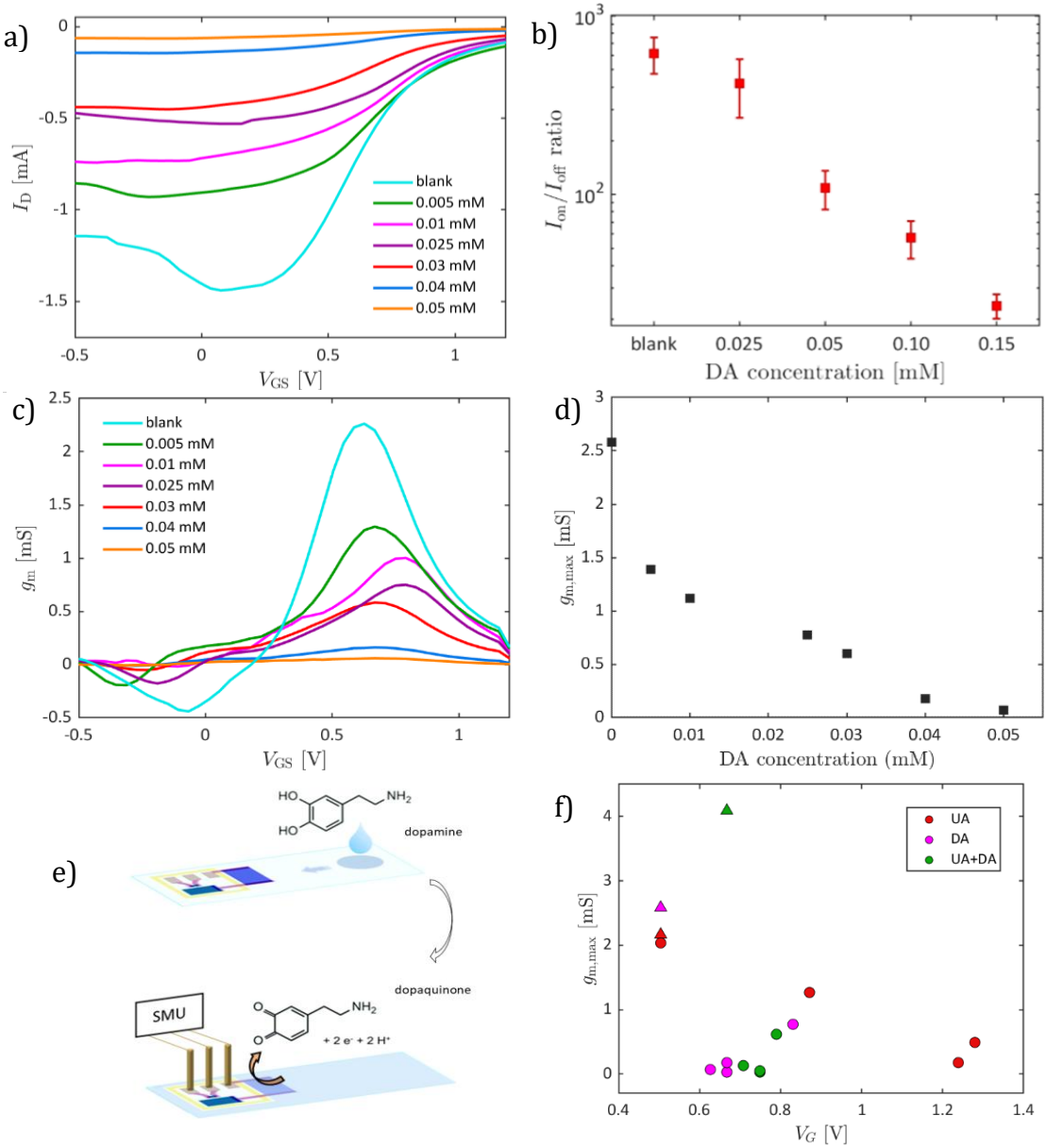

Figure 4.8 a) Transfer characteristics, b) I_{on}/I_{off} ratio averaged over three devices, and c) transconductance measured at different DA concentrations. d) Calibration plot obtained for DA from the extracted maximum transconductance. e) Schematic of the sensing mechanism. f) Maximum transconductance for devices tested with UA, DA, and mixed UA+DA solutions. UA and DA were individually tested at 0.025, 0.05, 0.1, and 0.15 mM. For UA+DA samples, UA concentration was fixed at 0.1 mM while DA concentration was varied (0.025, 0.05, 0.1, and 0.15 mM). Triangles indicate the blank for each series.

substantially expand the applicability of the proposed platform for low-concentration biomarker detection.

Overall, the sensing performance of fabricated devices suffers from variability in their initial electrical characteristics (Figure 4.13a), likely due to the intrinsic variations associated with the deposition of the PEDOT:PSS ink on a porous substrate. Part of the relatively high limit of detection observed in this work can be attributed to the variability of the initial electrical properties among different devices, which increases the standard deviation of blank measurements used for limit of detection calculation. Moreover, devices with lower maximum transconductance are inherently less sensitive, and they therefore show worse performances in DA sensing (Figure 4.13b). However, when considering the response of each device individually, a measurable variation is already observed between the blank and the lowest investigated dopamine concentration (0.005 mM), suggesting that the intrinsic sensitivity of the sensing architecture is higher than that indicated by the overall calibration obtained from multiple devices (Figure 4.13c). In addition to selecting devices with high maximum transconductance, a practical approach to compensate for these differences would consist of performing a preliminary measurement using a blank solution immediately before sample analysis. Besides providing the reference drain current for the specific device, this initial measurement would also allow stabilization of the electrochemical response. Similar conditioning procedures have been adopted in previous studies on OECT-based sensors, where preliminary measurement cycles are performed before analytical evaluation to obtain a stable baseline[48,261].

From a fabrication perspective, device reproducibility could be improved by optimizing the printing process and by introducing a preparatory layer in the dry region of the nitrocellulose substrate. Such a layer could partially fill the cellulose pores before PEDOT:PSS deposition, reducing variations in ink absorption, film thickness, and channel morphology due to local differences in nitrocellulose porosity and absorption properties, thus decreasing device-to-device variability and providing more reliable sensing responses.

In conclusion, the proposed platform could be improved through several complementary strategies. Improving fabrication reproducibility via the local printing of a preparatory layer before PEDOT:PSS deposition could allow the creation of a reliable calibration curve and the reduction of limit of detection. Sensitivity and specificity could also benefit from a reduction in the measurements scan rate, at the expense of the total test time. Lastly, printing of a bioink containing antibodies or enzymes to be physically adsorbed on the sensing extended gate could boost the sensitivity and specificity of the device towards specific analytes. By exploiting the ability of nitrocellulose to retain biomolecules,

the gate functionalization could represent a promising strategy for enhancing device performances without complex surface modifications steps usually required to functionalize traditional rigid substrates.

Table 4.3. Overview of the estimated costs per device.

Equipment	Supplier price (€)	Estimate cost per device (€)
Nitrocellulose	131 for 10 sheets	0.08
Silver ink	~ 90 for 2 ml	0.09
PEDOT:PSS ink	~ 300 for 100 g	0.02
Printing nozzle	22 for 25 nozzles	0.01
Permanent marker	1.5 per marker	0.03
SSE	12.14 for 2.5 ml	0.015
Kapton mask	~ 70 for 5 sheets	0.60
Al_2O_3 layer	~ 65 per run	0.25
	Total cost per device	~ 1.10

Overall, the presented results demonstrate that a fully printed OECT can operate on nitrocellulose and can be integrated into a capillary-driven strip, maintaining simple processing and low fabrication cost, as shown in Table 4.3, where an overview of the estimated costs per device is reported. A detailed breakdown of each entry is provided in the dedicated section of the Appendix.

The combination of dispense printing, localized electrolyte deposition, and separation between wet and dry regions enabled stable operation of the transistor on a porous substrate. The choice of materials and the fabrication process were optimized to achieve a cost per device on the order of a few euros, weighing the economic sustainability of the proposed system. This aspect is particularly important since the device is designed for single-use operation: as commonly observed in cellulose-based strips, residual analyte molecules remain trapped within the pores of the substrate after the measurement, preventing the restoration of the initial baseline and therefore limiting the possibility of reuse.

The geometrical dimensions of the device were optimized to grant comfortable use during sample deposition and measurement acquisition, while providing enough sensing electrode area for future potential functionalization. However, the Voltera V-One supports device miniaturization, as observed from tests on a PMMA substrate (Figure 4.9), potentially supporting further production cost reduction.

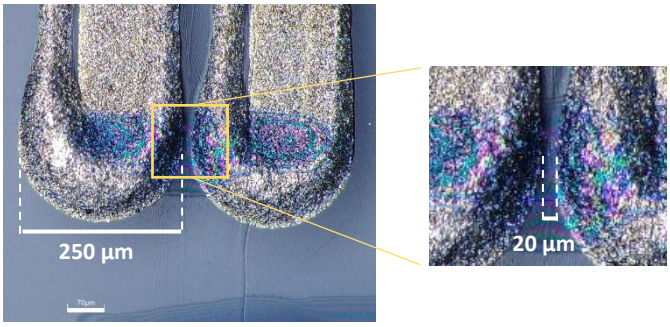

Figure 4.9 Microscopy image of silver dispense-printed source and drain, having maxi-mum width of about 250 µm and nominal distance from one another of 50 µm. Scale bar is 70 µm. The effective resulting channel length was about 20 µm, as shown in the inset of the inkjet-printed PEDOT:PSS channel.

4.4 Future perspective

The proposed architecture represents a starting point for the development of low-cost electronic lateral-flow platforms that combine the simplicity of paper-based assays with the analytical capabilities of organic transistors.

Further improvements in selectivity and sensitivity could be achieved by both working on the fabrication and on the functionalization and characterization of the devices. From the point of view of the fabrication process, laying a preparatory layer could help homogenizing the PEDOT:PSS layers printed on nitrocellulose, reducing the variability in channel properties among different devices and allowing to strive for high transconductance values. After the optimization of the printing process, introducing specific biomolecules via physical adsorption on the gate electrode, coupling the system with nanoparticle-based signal amplification strategies, and decreasing the scan rate could contribute to enhance both the sensitivity and the selectivity of the device. In particular, the immobilization of antibodies, enzymes, aptamers, or other biorecognition elements on the gate surface could enable selective detection of target analytes through specific binding events occurring directly on the nitrocellulose strip. In this configuration, molecular recognition at the sensing interface could be transduced into measurable variations of the transistor response, paving the way for quantitative and application-specific diagnostic tests.

Integration of nanomaterials like gold nanoparticles, commonly used in colorimetric LFAs, could contribute to the electrical signal amplification, as reported in previous studies on OECT-based sensors[262,263]. Such strategy could allow the combination of the traditional colorimetric output, resulting from the

agglomeration of nanoparticles, with an amplified electrical output, thus providing the user with a more immediate qualitative response, given by the colored control and test lines, together with the objective response from the transistor.

Additional developments may also focus on expanding the range of detectable targets, including pathogens, metabolites, and environmental contaminants, as well as on the integration of portable readout electronics for fully autonomous point-of-care operation. The low operating voltage and relatively high output currents of the device make it well suited for coupling with compact and battery-powered acquisition systems.

Future studies should also address the long-term stability and shelf life of the platform. Preliminary tests showed that the progressive evaporation of water from the solid-state electrolyte (SSE), together with its absorption by the cellulose substrate, leads to a gradual reduction in device performance (Figure 4.10). Water is a crucial component of the SSE, as it acts as a mediator for ion transport from the ionic liquid through the PEDOT:PSS channel. Its loss therefore limits efficient electrochemical modulation of the transistor. Possible strategies to overcome this issue include the optimization of the electrolyte formulation, the introduction of encapsulation layers, the use of less volatile humectants, and the engineering of barrier layers in the dry region to reduce water uptake by the porous substrate. Addressing these aspects will be essential for translating the proposed concept into practical disposable devices with adequate storage stability and reproducible operation.

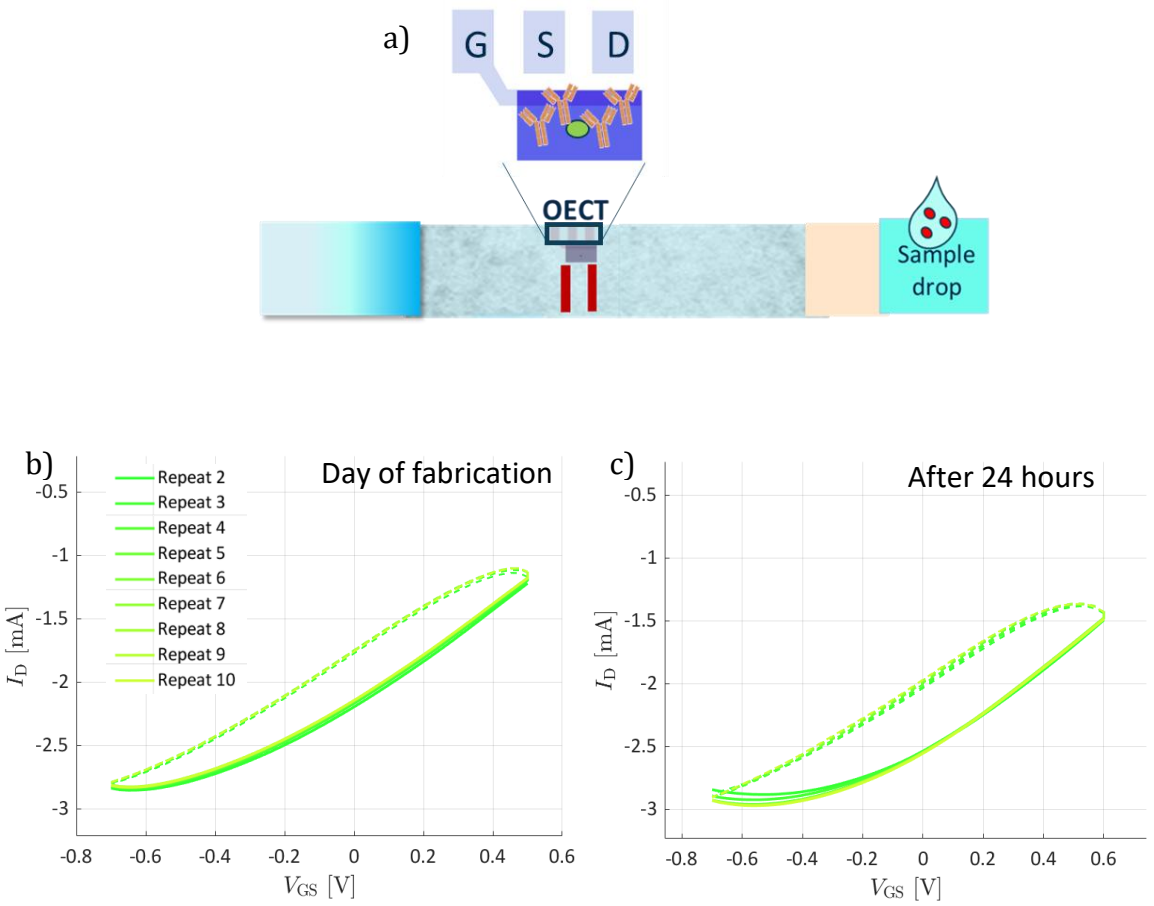

Figure 4.10 . a) Schematic of a printed OECT on a LFA strip with antibodies immobilized on the PEDOT:PSS gate. b, c) Transfer characteristics acquired over several cycles of measures of a printed OECT on cellulose on the day of fabrication (b) and after 24 hours (c).

4.5 Appendix 1: inkjet printing on porous substrates

To evaluate the feasibility of inkjet deposition of PEDOT:PSS on cellulose, the PEDOT:PSS channel and gate were printed using the piezoelectric drop-on-demand Jetlab®4 inkjet printer (Microfab Technologies) on previously dispense-printed silver electrodes. The ink formulation for PEDOT:PSS inkjet printing, previously described in Chapter 3, consisted of 76% v/v Clevios PH1000, 19% v/v ethylene glycol, 4% v/v dodecylbenzenesulfonic acid (DBSA), and 1% v/v

GOPS. The resulting OECTs had a channel length of 500 μm, a channel width of 300 μm, and gate dimensions of 4000 × 1500 μm^2 (Figure 4.11).

Figure 4.11a reports the effect of the number of inkjet-printed PEDOT:PSS layers on the performance of devices fabricated on nitrocellulose. While the two-layer and three-layer devices show similar performance, the one-layer device exhibits sensibly lower in modulus ON current (I_D at V_{GS}=-1V).

However, the ON current obtained with three layers of inkjet-printed PEDOT:PSS is approximately six times lower in absolute value than that achieved with three layers of dispense-printed PEDOT:PSS (Figure 4.7a). When comparing the performance of a two-layer device on nitrocellulose with that of an analogous device printed on poly(methyl methacrylate) (PMMA), it becomes evident that a significantly higher number of printed layers is required on nitrocellulose to reach performances comparable to those obtained on a smooth substrate (Figure 4.11b).

Overall, dispense printing of PEDOT:PSS proves to be more effective on porous substrates than inkjet printing. This can be attributed to the higher viscosity and higher ink volume delivered per deposition step, which help compensate for material dispersion within the branched pore network of the cellulose matrix. This dispersion effect observed with low viscosity, inkjet-printable inks is particularly evident when comparing the performance of films deposited on porous substrates with those fabricated on smooth surfaces.

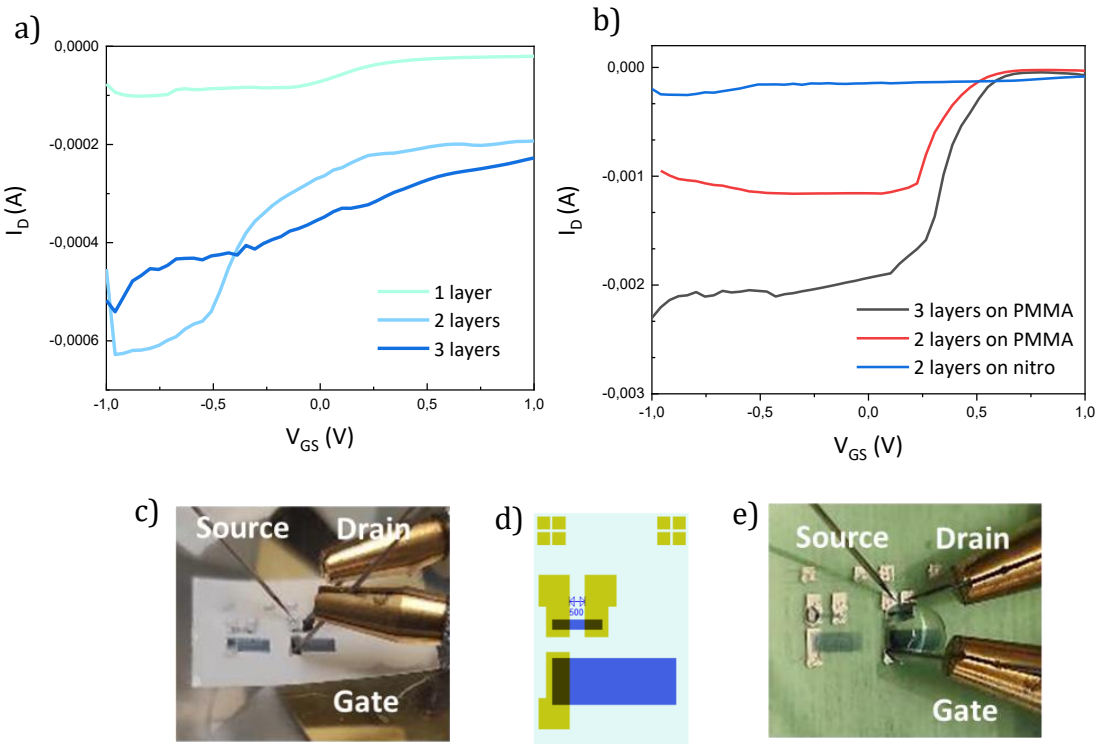

Figure 4.11 a) Forward transfer curves of printed OECTs on nitrocellulose having channel and gate constituted by 1, 2, or 3 layers of inkjet-printed PEDOT:PSS. b) Forward transfer curves of printed OECTs on nitrocellulose and on PMMA having channel and gate constituted by 2 or 3 layers of inkjet-printed PEDOT:PSS. c) Picture of the measure setup for the printed OECTs on nitrocellulose. d) Schematic of the printed OECTs architecture. e) Picture of the measure setup for the printed OECTs on PMMA.

4.6 Appendix 2: materials for hydrophobic barriers on paper

In the development of hydrophobic barriers for the separation of wet and dry regions and for the protection of silver electrodes from liquid media, alternative materials were explored prior to adopting a permanent marker as the final solution. Among these, beeswax and with parylene C were initially considered as a potential preparatory coating layer.

4.6.1 Experimental

The materials barrier function was tested after inkjet printing silver tracks, PEDOT:PSS channel and gate and SSE layer on top of the preparatory layers, using the Dimatix Materials Printer DMP-2800 with a standard Samba cartridge. The inkjet-printable silver ink was acquired by Novacentrix, and it was used as received. The ink formulation for PEDOT:PSS inkjet printing, previously described in Chapter 3, consisted of 76% v/v Clevios PH1000, 19% v/v ethylene glycol, 4% v/v dodecylbenzenesulfonic acid (DBSA), and 1% v/v GOPS. The resulting OECTs had a channel length of 300 μm, a channel width of 600 μm, and gate dimensions of 1500 × 1500 μm^2. The ink formulation for the SSE, previously described in Chapter 3, consisted of 1.0 mL of deionized water, 750.0 mg of N-isopropylacrylamide, 20.0 mg of crosslinker, 200.0 mg of photo-initiator, and 1.5 mL of ionic liquid, stirred overnight at room temperature.

4.6.2 Beeswax deposition

Beeswax is a natural, renewable material composed mainly of long-chain alkanes, fatty acids, and esters, widely used in coatings due to its hydrophobicity, biocompatibility, and low toxicity. In these experiments, beeswax was locally deposited to form a preparatory layer beneath inkjet-printed silver tracks by briefly heating it at approximately 60 °C using the tip of tweezers. However, the rapid solidification at room temperature made controlled and homogeneous deposition challenging, often resulting in non-uniform layers. Moreover, subsequent fabrication steps involving thermal curing of the silver and PEDOT:PSS inks led to partial remelting of the wax, introducing variability in the final device structure and posing a risk of interference with the conductive pathways.

Overall, the beeswax allowed to properly exploit the nitrocellulose capillarity for the transport of the liquid sample to the sensing gate, also providing good insulation of the channel and gate from the extended gate. Beeswax could be effectively employed as a hydrophobic barrier in dispense-printed devices rather than as a preparatory coating layer underneath inkjet-printed devices. However, its performance did not match that of the permanent marker in terms of reproducibility, stability, and ease of processing.

4.6.3 Parylene C deposition

Parylene C was also investigated as an alternative preparatory layer prior to inkjet printing of silver tracks. Parylene C, a poly(chloro-para-xylylene), is a

chemically inert, pinhole-free polymer commonly deposited via chemical vapor deposition (CVD) to form conformal thin films. It is widely used in microelectronics and biomedical applications as a dielectric layer, moisture barrier, and protective coating, as well as in photolithographic processes as a masking material due to its uniform coverage and chemical resistance. In this context, parylene C was considered for its potential to infiltrate and seal the pores of the nitrocellulose substrate, thereby reducing the dispersion of water-based silver inks and preventing direct contact between the conductive tracks and the liquid sample. However, practical limitations arose as the fragile and porous nature of nitrocellulose was incompatible with conventional masking approaches, based on adhesive tapes or films, for the regions intended to remain uncoated. As a result, the whole nitrocellulose strip became hydrophobic and lost its capability to adsorb and transport liquids by capillarity. This hindered selective deposition and limited the applicability of parylene C within the fabrication workflow.

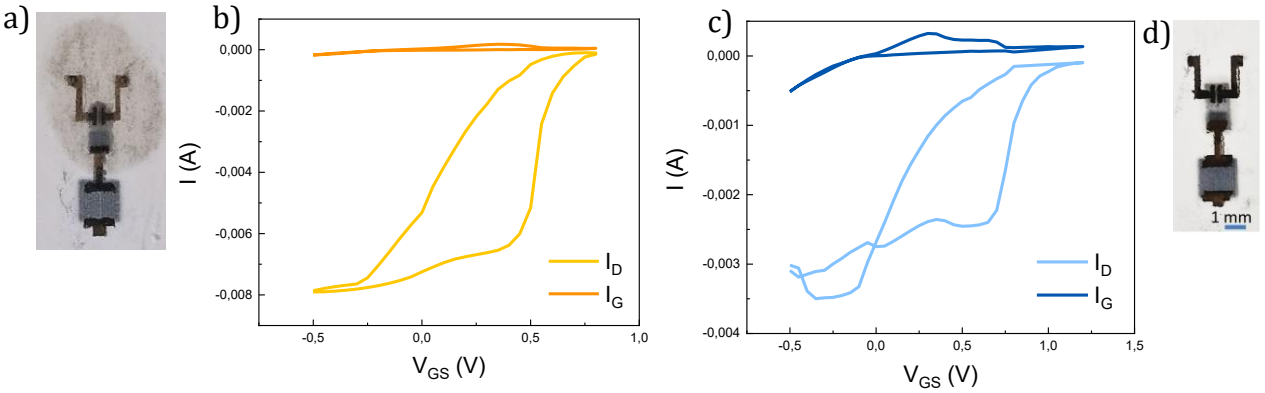

Figure 4.12 a) Picture and b) transfer curves of an OECT on nitrocellulose, fully inkjet-printed on a beeswax preparatory layer. c) Transfer curves and d) picture of an OECT on nitrocellulose, fully inkjet-printed on a parylene C preparatory layer.

4.7 Appendix 3: inter-device variability

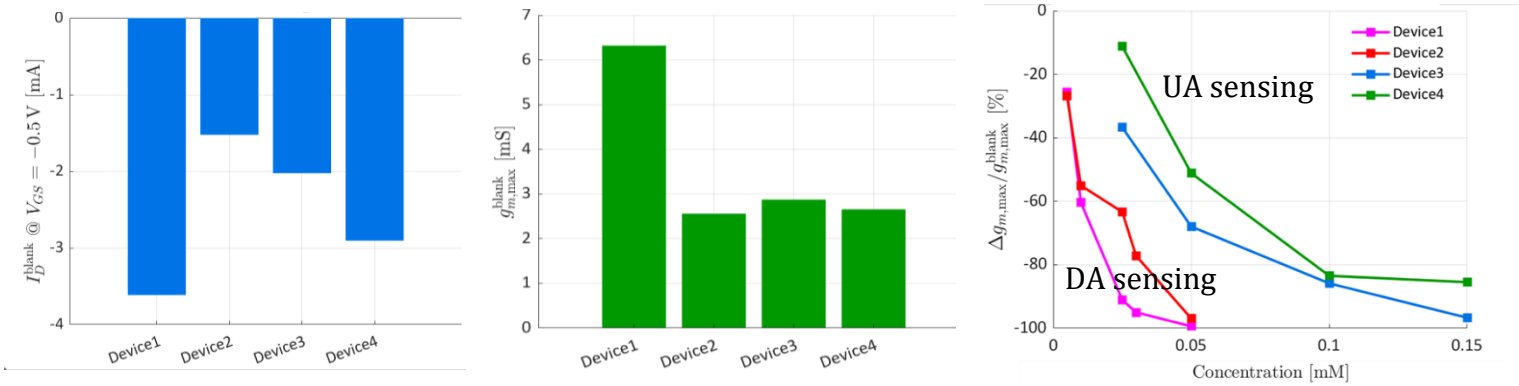

Figure 4.13. a) Drain current at V_{GS}=-0.5 V of 4 different devices. b) Maximum transconductance of the four devices in a), obtained from their forward transfer curves. c) Sensing response to DA (Device1 and Device2) and to UA (Device3 and Device4), calculated as $y = \frac{g_{m,max}^{conc} - g_{m,max}^{blank}}{g_{m,max}^{blank}}$.

Chapter 5

5 Conclusions

This thesis focused on the fabrication and characterization of PEDOT:PSS films, and on their integration in OECTs for point-of-care sensing applications.

The relationship between processing, morphology, and electrochemical behavior in inkjet-printed and aerosol-jet-printed PEDOT:PSS films integrated into OECTs was investigated in Chapter 3.

First, *in situ* Raman spectroscopy was used to monitor structural changes in inkjet-printed PEDOT:PSS during OECT operation. In the device with a bare gold gate, the PEDOT:PSS channel exhibited a progressive red shift of the C=C symmetric stretching band under positive gate bias, consistent with channel dedoping induced by cation injection from the electrolyte. When the gate bias was reversed, the band returned to its initial position, confirming the reversibility of the electrochemical process and in agreement with the expected operation of PEDOT:PSS-based OECTs.

In the device with PEDOT:PSS also deposited on the gate electrode, the Raman spectrum recorded under a 0.5 V gate bias exhibited a larger red shift of the C=C symmetric stretching band than that observed for the bare-gate device under the same conditions, providing direct evidence of the effect of higher gate capacitance on channel modulation. The Raman spectra acquired on the source and drain regions of the channel showed that the pristine material was already in an intermediate state, with coexistence of oxidized and neutral PEDOT fractions. Upon negative gate bias, the C=C stretching band shifted toward higher wavenumbers, indicating an increase in the oxidized PEDOT population, whereas positive gate bias produced a shift toward lower wavenumbers, associated with a larger contribution of reduced PEDOT species. Raman spectra acquired directly on the PEDOT:PSS-coated gate showed the opposite trend with respect to the channel, consistent with the fact that the conducting polymer gate is itself electrochemically active and undergoes redox modulation during gate bias application.

The Raman measurements performed on inkjet-printed PEDOT:PSS channels on nitrocellulose highlighted the potential influence of the substrate on the electrochemical behavior of the conducting polymer. While the pristine spectrum before measure was comparable to that recorded on glass, the spectrum

acquired after repeated operation cycles exhibited a red shift of the main C=C stretching band together with a reduction in intensity. These features suggest the presence of residual dedoping and possibly the onset of structural disorder or degradation. The porous cellulose matrix may promote ion retention and incomplete recovery of the initial oxidation state, which could hinder the reversibility of the film electrochemical modulation.

Overall, the Raman investigation confirmed that printed PEDOT:PSS films preserve the characteristic spectroscopic signatures reported in the literature for electrochemically modulated conducting polymers, while also revealing the important role of device architecture and substrate in determining the structural evolution of the material under bias. The results also emphasize that the interpretation of PEDOT:PSS Raman spectra remains complex and not univocal, since the observed shifts are influenced not only by benzoid-quinoid transitions but also by measure conditions and resonance effects.

Atomic force microscopy was employed to study the relationship between morphology and device performance of PEDOT:PSS channels deposited by inkjet printing, aerosol jet printing, and spin coating.

Electrical measurements showed that the deposition technique has a strong impact on OECT performance. Aerosol-jet-printed devices exhibited the fastest switching behavior, the highest I_{on}/I_{off} ratio, and the largest normalized transconductance, despite spin-coated devices showing the highest absolute ON current. Inkjet-printed devices displayed the lowest amplification capability among the three fabrication routes.

AFM analysis provided a structural explanation for these trends. Aerosol-jet-printed films showed a much higher surface roughness than inkjet-printed films, indicating a larger effective surface area. Phase images and dissipated energy maps further revealed that AJP films undergo a more pronounced phase segregation between PEDOT-rich and PSS-rich regions. In the AJP samples, elongated and oriented less dissipative domains, assigned to PEDOT-rich regions, were embedded in a more dissipative PSS-rich matrix. In contrast, the IJP films displayed a finer and more interconnected distribution of the insulating and the conducting phase. These observations suggest that aerosol jet printing promotes a redistribution of PEDOT and PSS during drying and annealing, favoring the formation of larger conductive domains. In AJP channel OECTs, the rougher morphology and enhanced phase segregation can facilitate ion access to the bulk of the channel while simultaneously providing more efficient electronic pathways through the PEDOT-rich phase. In this way, aerosol jet printing appears to optimize the balance between ionic and electronic transport, resulting in more efficient electrochemical modulation of the channel.

In Chapter 4, the design of a printable OECT on paper for integration into single-use LFAs was presented. For this sensing platform, the selection of materials, including a cellulose substrate, printed silver electrodes, and polymer-based gate architectures, together with a cost-effective fabrication technique, contributed to reducing fabrication costs while maintaining adequate device performance, leading to an estimated cost per device on the order of a few euros.

Among the explored fabrication techniques, dispense printing enabled the rapid prototyping and high-throughput manufacturing of low cost devices without the need for complex infrastructure. Although the passivation of the electrodes was achieved through a relatively expensive Al_2O_3 deposition via e-beam evaporation, its impact on costs can be mitigated in large-scale production, where fixed costs are distributed over a high number of devices.

The use of a solid-state electrolyte in the active area in combination with a hydrophobic barrier allowed a reliable separation between wet and dry regions of the device, essential to preserve channel stability, prevent undesired interactions with the analyte, and avoid contamination. While the use of hand-drawn barriers proved effective for prototyping, it introduces limitations in terms of industrialization and automation of the process. This could be addressed in future developments through automated patterning approaches and by optimizing specific inks for the definition of insulating regions.

The electrical characterization of the devices highlights their suitability for portable applications, thanks to low operating voltages and current levels in the milliampere range, which simplify signal acquisition and processing. When integrated into a capillary-driven nitrocellulose strip, the device exhibited stable operation and a Limit Of Detection of 0.01 mM for dopamine. Although this sensitivity does not yet reach the levels required for certain biomedical applications, the results validate the proposed architecture as a promising platform for the integration of OECTs into simple microfluidic systems. Improving device reproducibility upon fabrication optimization, striving for high maximum transconductance, reducing measurements scan rate, functionalizing the sensing gate with biomolecules, and coupling the device with nanoparticle-based amplification strategies could all contribute to lower the detection limit and achieve selectivity. Owing to its high surface area and direct exposure to the analyte, the extended gate offers a suitable interface for targeted sensing strategies.

Overall, the presented approach supports the development of scalable and affordable biosensing platforms based on printed electronics on paper substrates. The integration of OECTs into capillary-driven systems represents a promising direction toward the realization of fully integrated, low-cost point-of-care diagnostic devices.

Bibliography

(1) *Mapping the Landscape of Diagnostics for Sexually Transmitted Infections KEY FINDINGS AND RECOMMENDATIONS*.

(2) Land, K. J.; Boeras, D. I.; Chen, X. S.; Ramsay, A. R.; Peeling, R. W. REASSURED Diagnostics to Inform Disease Control Strategies, Strengthen Health Systems and Improve Patient Outcomes. *Nature Microbiology*. Nature Publishing Group January 1, 2019, pp 46–54. https://doi.org/10.1038/s41564-018-0295-3.

(3) Lee, S.; Bi, L.; Chen, H.; Lin, D.; Mei, R.; Wu, Y.; Chen, L.; Joo, S. W.; Choo, J. Recent Advances in Point-of-Care Testing of COVID-19. *Chemical Society Reviews*. Royal Society of Chemistry November 24, 2023, pp 8500–8530. https://doi.org/10.1039/d3cs00709j.

(4) Mannino, R. G.; Nehl, E. J.; Farmer, S.; Peagler, A. F.; Parsell, M. C.; Claveria, V.; Ku, D.; Gottfried, D. S.; Chen, H.; Lam, W. A.; Brand, O. *The Critical Role of Engineering in the Rapid Development of COVID-19 Diagnostics: Lessons from the RADx Tech Test Verification Core*; 2023. https://www.science.org.

(5) Budd, J.; Miller, B. S.; Weckman, N. E.; Cherkaoui, D.; Huang, D.; Decruz, A. T.; Fongwen, N.; Han, G. R.; Broto, M.; Estcourt, C. S.; Gibbs, J.; Pillay, D.; Sonnenberg, P.; Meurant, R.; Thomas, M. R.; Keegan, N.; Stevens, M. M.; Nastouli, E.; Topol, E. J.; Johnson, A. M.; Shahmanesh, M.; Ozcan, A.; Collins, J. J.; Fernandez Suarez, M.; Rodriguez, B.; Peeling, R. W.; McKendry, R. A. Lateral Flow Test Engineering and Lessons Learned from COVID-19. *Nature Reviews Bioengineering*. Springer Nature January 1, 2023, pp 13–31. https://doi.org/10.1038/s44222-022-00007-3.

(6) Kalyani, N.; Goel, S.; Jaiswal, S. On-site Sensing of Pesticides Using Point-of-care Biosensors: A Review. *Environmental Chemistry Letters*. Springer Science and Business Media Deutschland GmbH February 1, 2021, pp 345–354. https://doi.org/10.1007/s10311-020-01070-1.

(7) Baldi, P.; La Porta, N. Molecular Approaches for Low-Cost Point-of-Care Pathogen Detection in Agriculture and Forestry. *Frontiers in Plant*

Science. Frontiers Media S.A. October 28, 2020. https://doi.org/10.3389/fpls.2020.570862.

(8) Teixeira, S. C.; Gomes, N. O.; Calegaro, M. L.; Machado, S. A. S.; de Oliveira, T. V.; de Fátima Ferreira Soares, N.; Raymundo-Pereira, P. A. Sustainable Plant-Wearable Sensors for on-Site, Rapid Decentralized Detection of Pesticides toward Precision Agriculture and Food Safety. *Biomaterials Advances* **2023**, *155*. https://doi.org/10.1016/j.bioadv.2023.213676.

(9) Jafari, S.; Guercetti, J.; Geballa-Koukoula, A.; Tsagkaris, A. S.; Nelis, J. L. D.; Marco, M. P.; Salvador, J. P.; Gerssen, A.; Hajslova, J.; Elliott, C.; Campbell, K.; Migliorelli, D.; Burr, L.; Generelli, S.; Nielen, M. W. F.; Sturla, S. J. Assured Point-of-Need Food Safety Screening: A Critical Assessment of Portable Food Analyzers. *Foods*. MDPI June 1, 2021. https://doi.org/10.3390/foods10061399.

(10) Kakkar, S.; Gupta, P.; Kumar, N.; Kant, K. Progress in Fluorescence Biosensing and Food Safety towards Point-of-Detection (PoD) System. *Biosensors*. MDPI February 1, 2023. https://doi.org/10.3390/bios13020249.

(11) Tovar, R. M. *Bed-Side Agglutination Test for Rapid Diagnosis of Tularemia*; 1945.

(12) Penneys, R. Studies with the Millikan Oximeter at the Bedside of Patients with Cardiac and Pulmonary Disease. *Bull. Johns Hopkins Hosp.* **1952**, *90* (3), 192–200.

(13) Talbott, G. D.; King, W. A Bedside Method for Semiquantitative Sodium Analysis. *Stanford Med. Bull.* **1952**, *10* (2), 82–86.

(14) Talbott, G. D. A Bedside Laboratory Kit for Rapid Chemical Evaluation of the Patient. *Am. Pract. Dig. Treat.* **1954**, *5* (9), 724–728.

(15) Cretti, M.; Gloor, U.; Albrecht, R.; Bürgi, H. Blood Glucose Determination at the Bedside with Test Strips and Reflection Photometer: Comparison of 2 Instruments with a Standard Method. *Schweiz. Med. Wochenschr.* **1984**, *144,43*, 1492–1494.

(16) Streiff, F. Presentation of Device Intended for the Blood Group Compatibility Test at the Patient's Bedside. *Ann. Med. Nancy* **1965**, *4*, 778–783.

(17) Marks, V.; Dawson, A. Rapid-Stick-Method-for-Determining-Blood-Glucose-Concentration. *Br. Med. J.* **1965**, *1*, 293–294.

(18) Boyd, D. R.; Baker, R. J. Osmometry: A New Bedside Laboratory Aid for the Management of Surgical Patients. *Surgical Clinics of North America* **1971**, *51* (1), 241–250. https://doi.org/10.1016/S0039-6109(16)39345-8.

(19) Liu, X.; Zhu, X.; Kost, G. J.; Liu, J.; Huang, J.; Liu, X. The Creation of Point-of-Careology. *Point Care* **2019**, *18* (3), 77–84. https://doi.org/10.1097/POC.0000000000000191.

(20) Schnell, O.; Crocker, J. B.; Weng, J. Impact of HbA1c Testing at Point of Care on Diabetes Management. *Journal of Diabetes Science and Technology*. SAGE Publications Inc. May 1, 2017, pp 611–617. https://doi.org/10.1177/1932296816678263.

(21) Khor, S. M.; Choi, J.; Won, P.; Ko, S. H. Challenges and Strategies in Developing an Enzymatic Wearable Sweat Glucose Biosensor as a Practical Point-Of-Care Monitoring Tool for Type II Diabetes. *Nanomaterials*. MDPI January 1, 2022. https://doi.org/10.3390/nano12020221.

(22) Mandal, N.; Mitra, S.; Bandyopadhyay, D. Paper-Sensors for Point-of-Care Monitoring of Drinking Water Quality. *IEEE Sens. J.* **2019**, *19* (18), 7936–7941. https://doi.org/10.1109/JSEN.2019.2919269.

(23) Thwala, L. N.; Ndlovu, S. C.; Mpofu, K. T.; Lugongolo, M. Y.; Mthunzi-Kufa, P. Nanotechnology-Based Diagnostics for Diseases Prevalent in Developing Countries: Current Advances in Point-of-Care Tests. *Nanomaterials*. MDPI April 1, 2023. https://doi.org/10.3390/nano13071247.

(24) Hengel, B.; Causer, L.; Matthews, S.; Smith, K.; Andrewartha, K.; Badman, S.; Spaeth, B.; Tangey, A.; Cunningham, P.; Saha, A.; Phillips, E.; Ward, J.; Watts, C.; King, J.; Applegate, T.; Shephard, M.; Guy, R. A Decentralised Point-of-Care Testing Model to Address Inequities in the COVID-19 Response. *The Lancet Infectious Diseases*. Lancet Publishing Group July 1, 2021, pp e183–e190. https://doi.org/10.1016/S1473-3099(20)30859-8.

(25) Drain, P. K.; Hyle, E. P.; Noubary, F.; Freedberg, K. A.; Wilson, D.; Bishai, W. R.; Rodriguez, W.; Bassett, I. V. Diagnostic Point-of-Care Tests in Resource-Limited Settings. *The Lancet Infectious Diseases*. March 2014, pp 239–249. https://doi.org/10.1016/S1473-3099(13)70250-0.

(26) Huang, Y.; Cheng, Z.; Han, R.; Gao, X.; Qian, L.; Wen, Y.; Zhang, X.; Liu, G. Target-Induced Molecular-Switch on Triple-Helix DNA-Functionalized Carbon Nanotubes for Simultaneous Visual Detection of Nucleic Acids and Proteins. *Chem. Commun.* **2020**, *56* (88), 13657–13660. https://doi.org/10.1039/D0CC05986B.

(27) Kuralay, F.; Demirci, S.; Kiristi, M.; Oksuz, L.; Oksuz, A. U. Poly(3,4-Ethylenedioxythiophene) Coated Chitosan Modified Disposable Electrodes for DNA and DNA-Drug Interaction Sensing. *Colloids Surf. B Biointerfaces* **2014**, *123*, 825–830. https://doi.org/10.1016/j.colsurfb.2014.10.021.

(28) Shin, S. R.; Zhang, Y. S.; Kim, D. J.; Manbohi, A.; Avci, H.; Silvestri, A.; Aleman, J.; Hu, N.; Kilic, T.; Keung, W.; Righi, M.; Assawes, P.; Alhadrami, H. A.; Li, R. A.; Dokmeci, M. R.; Khademhosseini, A. Aptamer-Based Microfluidic Electrochemical Biosensor for Monitoring Cell-Secreted Trace Cardiac Biomarkers. *Anal. Chem.* **2016**, *88* (20), 10019–10027. https://doi.org/10.1021/acs.analchem.6b02028.

(29) Das, R.; Dhiman, A.; Kapil, A.; Bansal, V.; Sharma, T. K. Aptamer-Mediated Colorimetric and Electrochemical Detection of Pseudomonas Aeruginosa Utilizing Peroxidase-Mimic Activity of Gold NanoZyme. *Anal. Bioanal. Chem.* **2019**, *411* (6), 1229–1238. https://doi.org/10.1007/s00216-018-1555-z.

(30) Dalirirad, S.; Steckl, A. J. Lateral Flow Assay Using Aptamer-Based Sensing for on-Site Detection of Dopamine in Urine. *Anal. Biochem.* **2020**, *596*. https://doi.org/10.1016/j.ab.2020.113637.

(31) Cui, G.; Yoo, J. H.; Woo, B. W.; Kim, S. S.; Cha, S.; Nam, H. *Disposable Amperometric Glucose Sensor Electrode with Enzyme-Immobilized Nitrocellulose Strip*; 2001; Vol. 54. www.elsevier.com/locate/talanta.

(32) Nandhakumar, P.; Muñoz San Martín, C.; Arévalo, B.; Ding, S.; Lunker, M.; Vargas, E.; Djassemi, O.; Campuzano, S.; Wang, J. Redox Cycling Amplified Electrochemical Lateral-Flow Immunoassay: Toward Decentralized Sensitive Insulin Detection. *ACS Sens.* **2023**, *8* (10), 3892–3901. https://doi.org/10.1021/acssensors.3c01445.

(33) Adeniyi, K. O.; Oyinlola, K.; Achadu, O. J.; Menard, H.; Grillo, F.; Yang, Z.; Adegoke, O. Molecularly Imprinted Viral Protein Integrated Zn-Cu-In-Se-P Quantum Dots Superlattice for Quantitative Ratiometric Electrochemical Detection of SARS-CoV-2 Spike Protein in Saliva. *ACS Appl. Nano*

Mater. **2024**, *7* (15), 17630–17647. https://doi.org/10.1021/acsanm.4c02882.

(34) Tang, K.; Turner, C.; Case, L.; Mehrehjedy, A.; He, X.; Miao, W.; Guo, S. Organic Electrochemical Transistor with Molecularly Imprinted Polymer-Modified Gate for the Real-Time Selective Detection of Dopamine. *ACS Appl. Polym. Mater.* **2022**, *4* (4), 2337–2345. https://doi.org/10.1021/acsapm.1c01563.

(35) Sun, W.; Taylor, C. S.; Zhang, Y.; Gregory, D. A.; Tomeh, M. A.; Haycock, J. W.; Smith, P. J.; Wang, F.; Xia, Q.; Zhao, X. Cell Guidance on Peptide Micropatterned Silk Fibroin Scaffolds. *J. Colloid Interface Sci.* **2021**, *603*, 380–390. https://doi.org/10.1016/j.jcis.2021.06.086.

(36) Zhang, L.; Wang, G.; Wu, D.; Xiong, C.; Zheng, L.; Ding, Y.; Lu, H.; Zhang, G.; Qiu, L. Highly Selective and Sensitive Sensor Based on an Organic Electrochemical Transistor for the Detection of Ascorbic Acid. *Biosens. Bioelectron.* **2018**, *100*, 235–241. https://doi.org/10.1016/j.bios.2017.09.006.

(37) Sackmann, E. K.; Fulton, A. L.; Beebe, D. J. The Present and Future Role of Microfluidics in Biomedical Research. *Nature*. Nature Publishing Group 2014, pp 181–189. https://doi.org/10.1038/nature13118.

(38) Watkins, N. N.; Hassan, U.; Damhorst, G.; Ni, H. K.; Vaid, A.; Rodriguez, W.; Bashir, R. Microfluidic CD4+ and CD8+ T Lymphocyte Counters for Point-of-Care HIV Diagnostics Using Whole Blood. *Sci. Transl. Med.* **2013**, *5* (214). https://doi.org/10.1126/scitranslmed.3006870.

(39) Yang, S. M.; Lv, S.; Zhang, W.; Cui, Y. Microfluidic Point-of-Care (POC) Devices in Early Diagnosis: A Review of Opportunities and Challenges. *Sensors*. MDPI February 1, 2022. https://doi.org/10.3390/s22041620.

(40) Aryal, P.; Hefner, C.; Martinez, B.; Henry, C. S. Microfluidics in Environmental Analysis: Advancements, Challenges, and Future Prospects for Rapid and Efficient Monitoring. *Lab on a Chip*. Royal Society of Chemistry January 2, 2024, pp 1175–1206. https://doi.org/10.1039/d3lc00871a.

(41) Frey, N.; Sönmez, U. M.; Minden, J.; LeDuc, P. Microfluidics for Understanding Model Organisms. *Nature Communications*. Nature Research December 1, 2022. https://doi.org/10.1038/s41467-022-30814-6.

(42) Sameoto, D.; Wasay, A. Materials Selection and Manufacturing of Thermoplastic Elastomer Microfluidics. In *Microfluidics, BioMEMS, and Medical*

Microsystems XIII; SPIE, 2015; Vol. 9320, p 932001. https://doi.org/10.1117/12.2081291.

(43) Yang, K.; Peretz-Soroka, H.; Liu, Y.; Lin, F. Novel Developments in Mobile Sensing Based on the Integration of Microfluidic Devices and Smartphones. *Lab on a Chip*. Royal Society of Chemistry March 21, 2016, pp 943–958. https://doi.org/10.1039/c5lc01524c.

(44) Castiaux, A. D.; Currens, E. R.; Martin, R. S. Direct Embedding and Versatile Placement of Electrodes in 3D Printed Microfluidic-Devices. *Analyst* **2020**, *145* (9), 3274–3282. https://doi.org/10.1039/d0an00240b.

(45) Segantini, M.; Parmeggiani, M.; Ballesio, A.; Palmara, G.; Frascella, F.; Marasso, S. L.; Cocuzza, M. Design of a Portable Microfluidic Platform for EGOT-Based in Liquid Biosensing. *Sensors* **2022**, *22* (3). https://doi.org/10.3390/s22030969.

(46) Hiramoto, K.; Ino, K.; Nashimoto, Y.; Ito, K.; Shiku, H. Electric and Electrochemical Microfluidic Devices for Cell Analysis. *Frontiers in Chemistry*. Frontiers Media S.A. 2019. https://doi.org/10.3389/fchem.2019.00396.

(47) Licciardello, M.; Traldi, C.; Cicolini, M.; Bertana, V.; Marasso, S. L.; Cocuzza, M.; Tonda-Turo, C.; Ciardelli, G. A Miniaturized Multicellular Platform to Mimic the 3D Structure of the Alveolar-Capillary Barrier. *Front. Bioeng. Biotechnol.* **2024**, *12*. https://doi.org/10.3389/fbioe.2024.1346660.

(48) Babic, J.; Ballesio, A.; Frascella, F.; Napione, L.; Pagani, M.; Parmeggiani, M.; Marasso, S. L. A Contamination-Free Electrolyte-Gated Organic Transistors Platform for High-Accuracy Tumor Biomarker Detection. *Sensors and Actuators Reports* **2025**, *9*. https://doi.org/10.1016/j.snr.2025.100341.

(49) Hassan, S. U.; Tariq, A.; Noreen, Z.; Donia, A.; Zaidi, S. Z. J.; Bokhari, H.; Zhang, X. Capillary-Driven Flow Microfluidics Combined with Smartphone Detection: An Emerging Tool for Point-of-Care Diagnostics. *Diagnostics*. Multidisciplinary Digital Publishing Institute (MDPI) August 1, 2020. https://doi.org/10.3390/diagnostics10080509.

(50) G Oliver. On Bedside Urinary Tests. *The Lancet* **1883**.

(51) Arakawa, C. K.; DeForest, C. A. Chapter 19 - Polymer Design and Development. In *Biology and Engineering of Stem Cell Niches*; Vishwakarma, A., Karp, J. M., Eds.; Academic Press: Boston, 2017; pp 295–314.

https://doi.org/https://doi.org/10.1016/B978-0-12-802734-9.00019-6.

(52) Jesionowski, T.; Kuznowicz, M.; Jędrzak, A.; Rębiś, T. Sensing Materials: Biopolymeric Nanostructures. In *Encyclopedia of Sensors and Biosensors (First Edition)*; Narayan, R., Ed.; Elsevier: Oxford, 2023; pp 286–304. https://doi.org/https://doi.org/10.1016/B978-0-12-822548-6.00015-7.

(53) Moldoveanu, S. C. 4 - Analytical Pyrolysis of Polymeric Carbohydrates. In *Analytical Pyrolysis of Natural Organic Polymers (Second Edition)*; Moldoveanu, S. C., Ed.; Elsevier, 2021; Vol. 20, pp 111–269. https://doi.org/https://doi.org/10.1016/B978-0-12-818571-1.00004-2.

(54) Fridley, G. E.; Holstein, C. A.; Oza, S. B.; Yager, P. The Evolution of Nitrocellulose as a Material for Bioassays. *MRS Bull.* **2013**, *38* (4), 326–330. https://doi.org/10.1557/mrs.2013.60.

(55) Morris, E.; Pulham, C. R.; Morrison, C. A. Structure and Properties of Nitrocellulose: Approaching 200 Years of Research. *RSC Advances*. Royal Society of Chemistry November 2, 2023, pp 32321–32333. https://doi.org/10.1039/d3ra05457h.

(56) O'Farrell, B. Evolution in Lateral Flow–Based Immunoassay Systems. In *Lateral Flow Immunoassay*; Wong, R., Tse, H., Eds.; Humana Press: Totowa, NJ, 2009; pp 1–33. https://doi.org/10.1007/978-1-59745-240-3_1.

(57) Tonkinson, J. L.; Stillman, B. A. *NITROCELLULOSE: A TRIED AND TRUE POLYMER FINDS UTILITY AS A POST-GENOMIC SUBSTRATE*; 2002; Vol. 7.

(58) Budd, J.; Miller, B. S.; Weckman, N. E.; Cherkaoui, D.; Huang, D.; Decruz, A. T.; Fongwen, N.; Han, G.-R.; Broto, M.; Estcourt, C. S.; Gibbs, J.; Pillay, D.; Sonnenberg, P.; Meurant, R.; Thomas, M. R.; Keegan, N.; Stevens, M. M.; Nastouli, E.; Topol, E. J.; Johnson, A. M.; Shahmanesh, M.; Ozcan, A.; Collins, J. J.; Fernandez Suarez, M.; Rodriguez, B.; Peeling, R. W.; McKendry, R. A. Lateral Flow Test Engineering and Lessons Learned from COVID-19. *Nature Reviews Bioengineering* **2023**, *1* (1), 13–31. https://doi.org/10.1038/s44222-022-00007-3.

(59) Mayer, K. M.; Hafner, J. H. Localized Surface Plasmon Resonance Sensors. *Chemical Reviews*. June 8, 2011, pp 3828–3857. https://doi.org/10.1021/cr100313v.

(60) Napione, L. Integrated Nanomaterials and Nanotechnologies in Lateral Flow Tests for Personalized Medicine Applications. *Nanomaterials*. MDPI September 1, 2021. https://doi.org/10.3390/nano11092362.

(61) Mistry, D. A.; Wang, J. Y.; Moeser, M. E.; Starkey, T.; Lee, L. Y. W. A Systematic Review of the Sensitivity and Specificity of Lateral Flow Devices in the Detection of SARS-CoV-2. *BMC Infect. Dis.* **2021**, *21* (1). https://doi.org/10.1186/s12879-021-06528-3.

(62) Solin, K.; Beaumont, M.; Borghei, M.; Orelma, H.; Mertens, P.; Rojas, O. J. Immobilized Cellulose Nanospheres Enable Rapid Antigen Detection in Lateral Flow Immunoassays. *Cellulose* **2023**, *30* (4), 2353–2365. https://doi.org/10.1007/s10570-022-05038-y.

(63) Qiu, W.; Baryeh, K.; Takalkar, S.; Chen, W.; Liu, G. Carbon Nanotube-Based Lateral Flow Immunoassay for Ultrasensitive of Proteins: Application to the Determination of IgG. *MICROCHIMICA ACTA* **2019**, *186* (7). https://doi.org/10.1007/s00604-019-3508-4.

(64) Deng, Y.; Jiang, H.; Li, X.; Lv, X. Recent Advances in Sensitivity Enhancement for Lateral Flow Assay. *Microchimica Acta*. Springer November 1, 2021. https://doi.org/10.1007/s00604-021-05037-z.

(65) Liu, Y.; Zhan, L.; Qin, Z.; Sackrison, J.; Bischof, J. C. Ultrasensitive and Highly Specific Lateral Flow Assays for Point-of-Care Diagnosis. *ACS Nano*. American Chemical Society March 23, 2021, pp 3593–3611. https://doi.org/10.1021/acsnano.0c10035.

(66) Liu, Z.; Hua, Q.; Wang, J.; Liang, Z.; Li, J.; Wu, J.; Shen, X.; Lei, H.; Li, X. A Smartphone-Based Dual Detection Mode Device Integrated with Two Lateral Flow Immunoassays for Multiplex Mycotoxins in Cereals. *Biosens. Bioelectron.* **2020**, *158*, 112178. https://doi.org/10.1016/J.BIOS.2020.112178.

(67) Feng, J.; Xue, Y.; Wang, X.; Song, Q.; Wang, B.; Ren, X.; Zhang, L.; Liu, Z. Sensitive, Simultaneous and Quantitative Detection of Deoxynivalenol and Fumonisin B1 in the Water Environment Using Lateral Flow Immunoassay Integrated with Smartphone. *Science of The Total Environment* **2022**, *834*, 155354. https://doi.org/10.1016/J.SCITOTENV.2022.155354.

(68) Perju, A.; Wongkaew, N. Integrating High-Performing Electrochemical Transducers in Lateral Flow Assay. https://doi.org/10.1007/s00216-021-03301-y/Published.

(69) Akanda, M. R.; Joung, H. A.; Tamilavan, V.; Park, S.; Kim, S.; Hyun, M. H.; Kim, M. G.; Yang, H. An Interference-Free and Rapid Electrochemical Lateral-Flow Immunoassay for One-Step Ultrasensitive Detection with Serum. *Analyst* **2014**, *139* (6), 1420–1425. https://doi.org/10.1039/c3an02328a.

(70) Le Brun, G.; Calucho, E.; Hauwaert, M.; Moumneh, R.; Maroli, G.; Yunus, S.; Rosati, G.; Álvarez-Diduk, R.; Piper, A.; Merkoçi, A.; Raskin, J. P. Studying Ion Transport Dynamics in Electrochemical Measurements of Lateral Flow Assays. *Journal of Electroanalytical Chemistry* **2024**, *966*. https://doi.org/10.1016/j.jelechem.2024.118399.

(71) Martinez, A. W.; Phillips, S. T.; Butte, M. J.; Whitesides, G. M. Patterned Paper as a Platform for Inexpensive, Low-Volume, Portable Bioassays. *Angew. Chem. Int. Ed.* **2007**, *46* (8), 1318–1320. https://doi.org/10.1002/anie.200603817.

(72) Ruiz, R. A.; Gonzalez, J. L.; Vazquez-Alvarado, M.; Martinez, N. W.; Martinez, A. W. Beyond Wax Printing: Fabrication of Paper-Based Microfluidic Devices Using a Thermal Transfer Printer. *Anal. Chem.* **2022**, *94* (25), 8833–8837. https://doi.org/10.1021/acs.analchem.2c01534.

(73) Roller, R. M.; Lieberman, M. Beyond Wax Printing: The Future of Paper Analytical Device Fabrication. *Sens. Actuators B Chem.* **2023**, *392*. https://doi.org/10.1016/j.snb.2023.134059.

(74) Koivunen, R.; Jutila, E.; Bollström, R.; Gane, P. Hydrophobic Patterning of Functional Porous Pigment Coatings by Inkjet Printing. *Microfluid. Nanofluidics* **2016**, *20* (6). https://doi.org/10.1007/s10404-016-1747-9.

(75) Sitanurak, J.; Fukanaa, N.; Wongpakdeea, T.; Thepchuaya, Y.; Ratanawimarnwong, N.; Amornsakchai, T.; Nacapricha, D. T-Shirt Ink for One-Step Screen-Printing of Hydrophobic Barriers for 2D- and 3D-Microfluidic Paper-Based Analytical Devices. *Talanta* **2019**, *205*. https://doi.org/10.1016/j.talanta.2019.120113.

(76) Sun, J.; Cheng, C.; Liao, Y. Screen Printed Paper-Based Diagnostic Devices with Polymeric Inks.

(77) Anushka; Bandopadhyay, A.; Das, P. K. Paper Based Microfluidic Devices: A Review of Fabrication Techniques and Applications. *European Physical Journal: Special Topics*. Springer Science and Business Media Deutschland GmbH June 1, 2023, pp 781–815. https://doi.org/10.1140/epjs/s11734-022-00727-y.

(78) Martinez, A. W.; Phillips, S. T.; Whitesides, G. M.; Carrilho, E. Diagnostics for the Developing World: Microfluidic Paper-Based Analytical Devices. *Anal. Chem.* **2010**, *82* (1), 3–10. https://doi.org/10.1021/ac9013989.

(79) Makhinia, A.; Beni, V.; Andersson Ersman, P. Screen-Printed Piezoelectric Sensors on Tattoo Paper Combined with All-Printed High-Performance Organic Electrochemical Transistors for Electrophysiological Signal Monitoring. *ACS Applied Materials and Interfaces*. American Chemical Society November 13, 2023. https://doi.org/10.1021/acsami.3c10299.

(80) Dungchai, W.; Chailapakul, O.; Henry, C. S. Electrochemical Detection for Paper-Based Microfluidics. *Anal. Chem.* **2009**, *81* (14), 5821–5826. https://doi.org/10.1021/ac9007573.

(81) Colozza, N.; Caratelli, V.; Moscone, D.; Arduini, F. Origami Paper-Based Electrochemical (Bio)Sensors: State of the Art and Perspective. *Biosensors*. MDPI September 1, 2021. https://doi.org/10.3390/BIOS11090328.

(82) Liu, H.; Xiang, Y.; Lu, Y.; Crooks, R. M. Aptamer-Based Origami Paper Analytical Device for Electrochemical Detection of Adenosine. *Angew. Chem. Int. Ed.* **2012**, *51* (28), 6925–6928. https://doi.org/10.1002/anie.201202929.

(83) Wang, C. C.; Hennek, J. W.; Ainla, A.; Kumar, A. A.; Lan, W. J.; Im, J.; Smith, B. S.; Zhao, M.; Whitesides, G. M. A Paper-Based Pop-up Electrochemical Device for Analysis of Beta-Hydroxybutyrate. *Anal. Chem.* **2016**, *88* (12), 6326–6333. https://doi.org/10.1021/acs.analchem.6b00568.

(84) Choi, S. Papertronics and Paperfluidics: Toward Integrated and Intelligent Paper Systems. *Device* **2025**, *3* (12), 100997. https://doi.org/10.1016/j.device.2025.100997.

(85) Hideki Shirakawa, B.; Louis, E. J.; Macdiarmid, A. G.; W A N K Chiang, C. H.; HEEGERt, A. J. *Synthesis of Electrically Conducting Organic Polymers : Halogen Derivatives of Polyacetylene, (CH)*; 1977.

(86) Köhler, A.; Bässler, H. *Electronic Processes in Organic Semiconductors.*; Wiley-VCH ; John Wiley [distributor]: Weinheim, 2015; Vol. 66.

(87) Scharber, M. C.; Sariciftci, N. S. Low Band Gap Conjugated Semiconducting Polymers. *Advanced Materials Technologies*. John Wiley and Sons Inc April 1, 2021. https://doi.org/10.1002/admt.202000857.

(88) Heeger, A. J.; Kivelson, S.; Schrieffer, J. R.; Su, W.-P. *Solitons in Conducting Polymers*; 1988.

(89) Furukawa, Y.; Shimokawa, D. Polarons, Bipolarons, and Electrical Properties of Crystalline Conducting Polymers. *Bulletin of the Chemical Society of Japan*. Chemical Society of Japan 2023, pp 1243–1251. https://doi.org/10.1246/bcsj.20230175.

(90) Coropceanu, V.; Cornil, J.; da Silva Filho, D. A.; Olivier, Y.; Silbey, R.; Brédas, J. L. Charge Transport in Organic Semiconductors. *Chemical Reviews*. April 2007, pp 926–952. https://doi.org/10.1021/cr050140x.

(91) Shi, Y.; Zhou, Y.; Che, Z.; Shang, J.; Wang, Q.; Liu, F.; Zhou, Y. Degradation Phenomena and Degradation Mechanisms for Highly Conductive PEDOT:PSS Films. *Mater. Lett.* **2022**, *308*. https://doi.org/10.1016/j.matlet.2021.131106.

(92) Pasveer, W. F.; Cottaar, J.; Tanase, C.; Coehoorn, R.; Bobbert, P. A.; Blom, P. W. M.; De Leeuw, M.; Michels, M. A. J. Unified Description of Charge-Carrier Mobilities in Disordered Semiconducting Polymers. *Phys. Rev. Lett.* **2005**, *94* (20). https://doi.org/10.1103/PhysRevLett.94.206601.

(93) Miller, A.; Abrahams, E. *Impurity Conduction at Low Concentrations*.

(94) Salleo, A. Charge Transport in Polymeric Transistors. *materials today* **2007**, *10*.

(95) Hill, I. M.; Hernandez, V.; Xu, B.; Piceno, J. A.; Misiaszek, J.; Giglio, A.; Junez, E.; Chen, J.; Ashby, P. D.; Jordan, R. S.; Wang, Y. Imparting High Conductivity to 3D Printed PEDOT:PSS. *ACS Appl. Polym. Mater.* **2023**, *5* (6), 3989–3998. https://doi.org/10.1021/acsapm.3c00232.

(96) Kim, J. Y.; Jung, J. H.; Lee, D. E.; Joo, J. *Enhancement of Electrical Conductivity of Poly(3,4-Ethylenedioxythiophene)/Poly(4-Styrenesulfonate) by a Change of Solvents*.

(97) Ashizawa, S.; Horikawa, R.; Okuzaki, H. Effects of Solvent on Carrier Transport in Poly(3,4-Ethylenedioxythiophene)/Poly(4-Styrenesulfonate). In *Synthetic Metals*; 2005; Vol. 153, pp 5–8. https://doi.org/10.1016/j.synthmet.2005.07.214.

(98) Isaksson, J.; Kjäll, P.; Nilsson, D.; Robinson, N.; Berggren, M.; Richter-Dahlfors, A. Electronic Control of Ca2+ Signalling in Neuronal Cells Using an Organic Electronic Ion Pump. *Nat. Mater.* **2007**, *6* (9), 673–679. https://doi.org/10.1038/nmat1963.

(99) Ding, B.; Jo, I. Y.; Yoon, M. H.; Heeney, M. Designing Organic Mixed Ionic-Electronic Conductors with Low Environmental Footprint for Bioelectronics and Energy Storage. *Materials Science and Engineering R: Reports*. Elsevier Ltd June 1, 2025. https://doi.org/10.1016/j.mser.2025.100974.

(100) Marks, A.; Griggs, S.; Gasparini, N.; Moser, M. Organic Electrochemical Transistors: An Emerging Technology for Biosensing. *Advanced Materials Interfaces*. John Wiley and Sons Inc February 1, 2022. https://doi.org/10.1002/admi.202102039.

(101) Shen, H.; Abtahi, A.; Lussem, B.; Boudouris, B. W.; Mei, J. Device Engineering in Organic Electrochemical Transistors toward Multifunctional Applications. *ACS Appl. Electron. Mater.* **2021**, *3* (6), 2434–2448. https://doi.org/10.1021/acsaelm.1c00312.

(102) Li, L.; Yin, Y. J.; Hei, J. P.; Wan, X. J.; Li, M. L.; Cui, Y. Molecular Engineering of Aromatic Imides for Organic Secondary Batteries. *Small*. John Wiley and Sons Inc March 1, 2021. https://doi.org/10.1002/smll.202005752.

(103) Bhosale, M. E.; Chae, S.; Kim, J. M.; Choi, J. Y. Organic Small Molecules and Polymers as an Electrode Material for Rechargeable Lithium Ion Batteries. *Journal of Materials Chemistry A*. Royal Society of Chemistry 2018, pp 19885–19911. https://doi.org/10.1039/c8ta04906h.

(104) Song, Z.; Zhou, H. Towards Sustainable and Versatile Energy Storage Devices: An Overview of Organic Electrode Materials. *Energy and Environmental Science*. August 2013, pp 2280–2301. https://doi.org/10.1039/c3ee40709h.

(105) Paulsen, B. D.; Tybrandt, K.; Stavrinidou, E.; Rivnay, J. Organic Mixed Ionic–Electronic Conductors. *Nature Materials*. Nature Research January 1, 2020, pp 13–26. https://doi.org/10.1038/s41563-019-0435-z.

(106) Inal, S.; Malliaras, G. G.; Rivnay, J. Benchmarking Organic Mixed Conductors for Transistors. *Nat. Commun.* **2017**, *8* (1). https://doi.org/10.1038/s41467-017-01812-w.

(107) Gkoupidenis, P.; Zhang, Y.; Kleemann, H.; Ling, H.; Santoro, F.; Fabiano, S.; Salleo, A.; van de Burgt, Y. Organic Mixed Conductors for Bioinspired Electronics. *Nat. Rev. Mater.* **2024**, *9* (2), 134–149. https://doi.org/10.1038/s41578-023-00622-5.

(108) Keene, S. T.; Rao, A.; Malliaras, G. G. *The Relationship between Ionic-Electronic Coupling and Transport in Organic Mixed Conductors*; 2023. https://www.science.org.

(109) BAYER AG OP - DE 3813589 A OP - DE 3843412 A, EP 0339340 A2, 1989.

(110) Pingrey, B.; Hsieh, Y. Lo. In Situ Polymerized PEDOT Dispersions with Sulfated Cellulose Nanofibrils for 1D and 2D Conductors. *Mater. Adv.* **2023**, *4* (20), 4912–4920. https://doi.org/10.1039/d3ma00486d.

(111) Rahimzadeh, Z.; Naghib, S. M.; Zare, Y.; Rhee, K. Y. An Overview on the Synthesis and Recent Applications of Conducting Poly(3,4-Ethylenedioxythiophene) (PEDOT) in Industry and Biomedicine. *Journal of Materials Science*. Springer June 1, 2020, pp 7575–7611. https://doi.org/10.1007/s10853-020-04561-2.

(112) Rivnay, J.; Mannsfeld, S. C. B.; Miller, C. E.; Salleo, A.; Toney, M. F. Quantitative Determination of Organic Semiconductor Microstructure from the Molecular to Device Scale. *Chemical Reviews*. October 10, 2012, pp 5488–5519. https://doi.org/10.1021/cr3001109.

(113) Horii, T.; Hikawa, H.; Katsunuma, M.; Okuzaki, H. Synthesis of Highly Conductive PEDOT:PSS and Correlation with Hierarchical Structure. *Polymer (Guildf).* **2018**, *140*, 33–38. https://doi.org/10.1016/j.polymer.2018.02.034.

(114) Rivnay, J.; Inal, S.; Collins, B. A.; Sessolo, M.; Stavrinidou, E.; Strakosas, X.; Tassone, C.; Delongchamp, D. M.; Malliaras, G. G. Structural Control of Mixed Ionic and Electronic Transport in Conducting Polymers. *Nat. Commun.* **2016**, *7*. https://doi.org/10.1038/ncomms11287.

(115) Nardes, A. M.; Kemerink, M.; Janssen, R. A. J.; Bastiaansen, J. A. M.; Kiggen, N. M. M.; Langeveld, B. M. W.; Van Breemen, A. J. J. M.; De Kok, M. M. Microscopic Understanding of the Anisotropic Conductivity of PEDOT:PSS

Thin Films. *Advanced Materials* **2007**, *19* (9), 1196–1200. https://doi.org/10.1002/adma.200602575.

(116) Murakami, T.; Mori, Y.; Okuzaki, H. *Effect of Ethylene Glycol on Structure and Carrier Transport in Highly Conductive Poly(3,4-Ethylenedioxythiophene)/Poly(4-Styrenesulfonate)*.

(117) Lee, I.; Kim, G. W.; Yang, M.; Kim, T. S. Simultaneously Enhancing the Cohesion and Electrical Conductivity of PEDOT:PSS Conductive Polymer Films Using DMSO Additives. *ACS Appl. Mater. Interfaces* **2016**, *8* (1), 302–310. https://doi.org/10.1021/acsami.5b08753.

(118) Srivastava, A.; Sharma, R. K.; Sharma, D.; Kumari, P.; Agrawal, V. V.; Srivastava, S. K. Influence of Alcoholic Polar Surfactants on PEDOT:PSS for Enhanced Performance of Organic/Si Hybrid Solar Cell. *Surfaces and Interfaces* **2023**, *38*. https://doi.org/10.1016/j.surfin.2023.102822.

(119) Zhang, W.; Bi, X.; Zhao, X.; Zhao, Z.; Zhu, J.; Dai, S.; Lu, Y.; Yang, S. Isopropanol-Treated PEDOT:PSS as Electron Transport Layer in Polymer Solar Cells. *Org. Electron.* **2014**, *15* (12), 3445–3451. https://doi.org/10.1016/j.orgel.2014.09.026.

(120) Otero, T. F.; Martinez, J. G.; Hosaka, K.; Okuzaki, H. Electrochemical Characterization of PEDOT-PSS-Sorbitol Electrodes. Sorbitol Changes Cation to Anion Interchange during Reactions. *Journal of Electroanalytical Chemistry* **2011**, *657* (1–2), 23–27. https://doi.org/10.1016/j.jelechem.2011.02.017.

(121) Asri, N. A. N.; Amir, B.; Ramli, A. S.; Safian, M. F.; Zakaria, A.; Jani, N. A.; Mahat, M. M. The Effect of Ethylene Glycol Post-Treatment on the Electrical Conductivity of PEDOT: PSS Thin Films. In *Journal of Physics: Conference Series*; IOP Publishing Ltd, 2022; Vol. 2169. https://doi.org/10.1088/1742-6596/2169/1/012036.

(122) Nardes, A. M.; Janssen, R. A. J.; Kemerink, M. A Morphological Model for the Solvent-Enhanced Conductivity of PEDOT:PSS Thin Films. *Adv. Funct. Mater.* **2008**, *18* (6), 865–871. https://doi.org/10.1002/adfm.200700796.

(123) Lang, U.; Naujoks, N.; Dual, J. Mechanical Characterization of PEDOT:PSS Thin Films. *Synth. Met.* **2009**, *159* (5–6), 473–479. https://doi.org/10.1016/j.synthmet.2008.11.005.

(124) Guo, X.; Facchetti, A. The Journey of Conducting Polymers from Discovery to Application. *Nature Materials*. Nature Research September 1, 2020, pp 922–928. https://doi.org/10.1038/s41563-020-0778-5.

(125) White, H. S.; Kittlesen, G. P.; Wrighton, M. S. *Chemical Derivatization of an Array of Three Gold with Polypyrrole: Fabrication of a Molecule-Based Transistor*; 1984; Vol. 106.

(126) Bernards, D. A.; Malliaras, G. G. Steady-State and Transient Behavior of Organic Electrochemical Transistors. *Adv. Funct. Mater.* **2007**, *17* (17), 3538–3544. https://doi.org/10.1002/adfm.200601239.

(127) Ohayon, D.; Druet, V.; Inal, S. A Guide for the Characterization of Organic Electrochemical Transistors and Channel Materials. *Chemical Society Reviews*. Royal Society of Chemistry January 13, 2023, pp 1001–1023. https://doi.org/10.1039/d2cs00920j.

(128) Friedlein, J. T.; Rivnay, J.; Dunlap, D. H.; McCulloch, I.; Shaheen, S. E.; McLeod, R. R.; Malliaras, G. G. Influence of Disorder on Transfer Characteristics of Organic Electrochemical Transistors. *Appl. Phys. Lett.* **2017**, *111* (2). https://doi.org/10.1063/1.4993776.

(129) Friedlein, J. T.; McLeod, R. R.; Rivnay, J. Device Physics of Organic Electrochemical Transistors. *Organic Electronics*. Elsevier B.V. December 1, 2018, pp 398–414. https://doi.org/10.1016/j.orgel.2018.09.010.

(130) Yang, S. Y.; Cicoira, F.; Byrne, R.; Benito-Lopez, F.; Diamond, D.; Owens, R. M.; Malliaras, G. G. Electrochemical Transistors with Ionic Liquids for Enzymatic Sensing. *Chemical Communications* **2010**, *46* (42), 7972–7974. https://doi.org/10.1039/c0cc02064h.

(131) Weissbach, A.; Bongartz, L. M.; Cucchi, M.; Tseng, H.; Leo, K.; Kleemann, H. Photopatternable Solid Electrolyte for Integrable Organic Electrochemical Transistors: Operation and Hysteresis. *J. Mater. Chem. C Mater.* **2022**, *10* (7), 2656–2662. https://doi.org/10.1039/d1tc04230k.

(132) Cho, J. H.; Lee, J.; He, Y.; Kim, B.; Lodge, T. P.; Frisbie, C. D. High-Capacitance Ion Gel Gate Dielectrics with Faster Polarization Response Times for Organic Thin Film Transistors. *Advanced Materials* **2008**, *20* (4), 686–690. https://doi.org/10.1002/adma.200701069.

(133) Meier, T.; Yoon, Y.; Teuerle, L.; Solgi, A.; Leo, K.; Kleemann, H. A Hybrid Process for Integration of Organic Electrochemical Transistors for High

Uniformity & Reliability. *MRS Commun.* **2024**, *14* (2), 149–157. https://doi.org/10.1557/s43579-023-00498-0.

(134) Melianas, A.; Quill, T. J.; LeCroy, G.; Tuchman, Y.; Loo, H.; Keene, S. T.; Giovannitti, A.; Lee, H. R.; Maria, I. P.; McCulloch, I.; Salleo, A. *Temperature-Resilient Solid-State Organic Artificial Synapses for Neuromorphic Computing*; 2020. https://www.science.org.

(135) Chen, J.; Fang, Y.; Feng, J.; Shi, X.; Li, J.; Wang, S.; Zhang, S.; Peng, H.; Sun, X. Fast-Response Fiber Organic Electrochemical Transistor with Vertical Channel Design for Electrophysiological Monitoring. *J. Mater. Chem. B* **2024**, *12* (37), 9206–9212. https://doi.org/10.1039/d4tb01426j.

(136) Tarabella, G.; Villani, M.; Calestani, D.; Mosca, R.; Iannotta, S.; Zappettini, A.; Coppedè, N. A Single Cotton Fiber Organic Electrochemical Transistor for Liquid Electrolyte Saline Sensing. *J. Mater. Chem.* **2012**, *22* (45), 23830–23834. https://doi.org/10.1039/c2jm34898e.

(137) Lee, S. K.; Cho, Y. W.; Lee, J. S.; Jung, Y. R.; Oh, S. H.; Sun, J. Y.; Kim, S. B.; Joo, Y. C. Nanofiber Channel Organic Electrochemical Transistors for Low-Power Neuromorphic Computing and Wide-Bandwidth Sensing Platforms. *Advanced Science* **2021**, *8* (10). https://doi.org/10.1002/advs.202001544.

(138) Yang, H.; Peng, X.; Liu, J. Nanofiber OECT Biosensors via Electrospinning: Boosting Stability and Sensitivity with Ultralow Material Use. *IEEE Sens. J.* **2025**. https://doi.org/10.1109/JSEN.2025.3643389.

(139) Zhou, Q.; Teng, W.; Jin, Y.; Sun, L.; Hu, P.; Li, H.; Wang, L.; Wang, J. Highly-Conductive PEDOT:PSS Hydrogel Framework Based Hybrid Fiber with High Volumetric Capacitance and Excellent Rate Capability. *Electrochim. Acta* **2020**, *334*. https://doi.org/10.1016/j.electacta.2019.135530.

(140) Rinaldi, G.; Vurro, D.; Cicolini, M.; Babic, J.; Liboà, A.; Tarabella, G.; D'Angelo, P.; Marasso, S. L.; Cocuzza, M.; Vigna, L.; Pirri, F. C.; Parmeggiani, M. PEDOT:PSS Deposition in OECTs: Inkjet Printing, Aerosol Jet Printing and Spin Coating. *Micro and Nano Engineering* **2024**, *24*, 100272. https://doi.org/https://doi.org/10.1016/j.mne.2024.100272.

(141) Chortos, A. Extrusion 3D Printing of Conjugated Polymers. *Journal of Polymer Science*. John Wiley and Sons Inc January 2, 2022, pp 486–503. https://doi.org/10.1002/pol.20210609.

(142) Khan, S.; Ali, S.; Khan, A.; Wang, B.; Bermak, A. Printing Sensors on Biocompatible Substrates for Selective Detection of Glucose. *IEEE Sens. J.* **2021**, *21* (4), 4167–4175. https://doi.org/10.1109/JSEN.2020.3032539.

(143) Idris, M. K.; Grau, G. Dispense Printing of Silver Flake Inks on Hydrophilic and Hydrophobic Surfaces. *Adv. Eng. Mater.* **2024**. https://doi.org/10.1002/adem.202401302.

(144) Wang, X.; Plog, J.; Lichade, K. M.; Yarin, A. L.; Pan, Y. Three-Dimensional Printing of Highly Conducting PEDOT: PSS-Based Polymers. *J. Manuf. Sci. Eng.* **2023**, *145* (1). https://doi.org/10.1115/1.4055850.

(145) Vasquez, S.; Petrelli, M.; Angeli, M. C.; Costa, J.; Avancini, E.; Cantarella, G.; Munzenrieder, N.; Lugli, P.; Petti, L. Cost-Effective, Mask-Less, and High-Throughput Prototyping of Flexible Hybrid Electronic Devices Using Dispense Printing and Conductive Silver Ink. In *2021 5th IEEE Electron Devices Technology and Manufacturing Conference, EDTM 2021*; Institute of Electrical and Electronics Engineers Inc., 2021. https://doi.org/10.1109/EDTM50988.2021.9420858.

(146) Diacci, C.; Lee, J. W.; Janson, P.; Dufil, G.; Méhes, G.; Berggren, M.; Simon, D. T.; Stavrinidou, E. Real-Time Monitoring of Glucose Export from Isolated Chloroplasts Using an Organic Electrochemical Transistor. *Adv. Mater. Technol.* **2020**, *5* (3). https://doi.org/10.1002/admt.201900262.

(147) Pappa, A. M.; Curto, V. F.; Braendlein, M.; Strakosas, X.; Donahue, M. J.; Fiocchi, M.; Malliaras, G. G.; Owens, R. M. Organic Transistor Arrays Integrated with Finger-Powered Microfluidics for Multianalyte Saliva Testing. *Adv. Healthc. Mater.* **2016**, *5* (17), 2295–2302. https://doi.org/10.1002/adhm.201600494.

(148) Bortolotti, C.; Ottomaniello, A.; Parlanti, P.; Mattoli, V.; Natali, D.; Aliverti, A.; Kyndiah, A.; Caironi, M. Sensing of Chloride Ions in Sweat by Means of Printed Extended-Gate Organic Electrochemical Transistors. *Adv. Funct. Mater.* **2025**. https://doi.org/10.1002/adfm.202511675.

(149) Fan, J.; Parr, S.; Kang, S.; Gupta, M. Point-of-Care (POC) SARS-CoV-2 Antigen Detection Using Functionalized Aerosol Jet-Printed Organic Electrochemical Transistors (OECTs). *Nanoscale* **2023**, *15* (11), 5476–5485. https://doi.org/10.1039/d2nr06485e.

(150) Colucci, R.; Koutsouras, D. A.; Morsbach, S.; Gkoupidenis, P.; Blom, P. W. M.; Kraft, U. Organic Electrochemical Transistor-Based Immunosensors

for SARS-CoV-2 Detection. *ACS Appl. Electron. Mater.* **2024**, *6* (4), 2739–2748. https://doi.org/10.1021/acsaelm.4c00260.

(151) Moudgil, A.; Hou, K.; Li, T.; Leong, W. L. Biocompatible Solid-State Ion-Sensitive Organic Electrochemical Transistor for Physiological Multi-Ions Sensing. *Adv. Mater. Technol.* **2023**, *8* (18). https://doi.org/10.1002/admt.202300605.

(152) Clua Estivill, M.; Ait Yazza, A.; Blondeau, P.; Andrade, F. J. Ion-Selective Organic Electrochemical Transistors for the Determination of Potassium in Clinical Samples. *Sens. Actuators B Chem.* **2024**, *401*. https://doi.org/10.1016/j.snb.2023.135027.

(153) Zhang, L.; Khayour, S.; Ren, G.; He, S.; Wang, J.; Yu, L.; Song, Y.; Zhu, C.; Kang, X.; Zhang, Y.; Gong, Z.; Gao, K.; Wang, J.; Sheng, H.; Lu, G.; Yu, H. D. Proton-Penetrable Nafion-Induced Phase Separation in Organic Semiconductors for High-Performance Organic Electrochemical Transistors. *J. Mater. Chem. C Mater.* **2023**, *11* (22), 7272–7282. https://doi.org/10.1039/d3tc01194a.

(154) Nguyen, T. D.; Trung, T. Q.; Lee, Y.; Lee, N. E. Stretchable and Stable Electrolyte-Gated Organic Electrochemical Transistor Synapse with a Nafion Membrane for Enhanced Synaptic Properties. *Adv. Eng. Mater.* **2022**, *24* (4). https://doi.org/10.1002/adem.202100918.

(155) Song, Y.; Zhang, H.; Mukhopadhyaya, T.; Hall, A. S.; Katz, H. E. Sensitive Organic Electrochemical Transistor Biosensors: Comparing Single and Dual Gate Functionalization and Different COOH-Functionalized Bioreceptor Layers. *Biosens. Bioelectron.* **2022**, *216*. https://doi.org/10.1016/j.bios.2022.114691.

(156) Bossard-Giannesini, L.; Cardenas, L.; Cruguel, H.; Demessence, A.; Loffreda, D.; Pluchery, O. How Far the Chemistry of Self-Assembled Monolayers on Gold Surfaces Affects Their Work Function? *Nanoscale* **2023**, *15* (42), 17113–17123. https://doi.org/10.1039/d3nr03172a.

(157) Aftab, S.; Zhou, J.; Cheng, Y.; Zhao, D.; Chen, H.; Huang, W. Functional Gate Modification for OECT-Based Sensors. *Materials Today Chemistry*. Elsevier Ltd September 1, 2025. https://doi.org/10.1016/j.mtchem.2025.102933.

(158) Di Franco, C.; Macchia, E.; Sarcina, L.; Ditaranto, N.; Khaliq, A.; Torsi, L.; Scamarcio, G. Extended Work Function Shift of Large-Area

Biofunctionalized Surfaces Triggered by a Few Single-Molecule Affinity Binding Events. *Adv. Mater. Interfaces* **2023**, *10* (6). https://doi.org/10.1002/admi.202201829.

(159) Guo, K.; Wustoni, S.; Koklu, A.; Díaz-Galicia, E.; Moser, M.; Hama, A.; Alqahtani, A. A.; Ahmad, A. N.; Alhamlan, F. S.; Shuaib, M.; Pain, A.; McCulloch, I.; Arold, S. T.; Grünberg, R.; Inal, S. Rapid Single-Molecule Detection of COVID-19 and MERS Antigens via Nanobody-Functionalized Organic Electrochemical Transistors. *Nat. Biomed. Eng.* **2021**, *5* (7), 666–677. https://doi.org/10.1038/s41551-021-00734-9.

(160) Fenoy, G. E.; Azzaroni, O.; Knoll, W.; Marmisollé, W. A. Functionalization Strategies of PEDOT and PEDOT:PSS Films for Organic Bioelectronics Applications. *Chemosensors*. Multidisciplinary Digital Publishing Institute (MDPI) August 1, 2021. https://doi.org/10.3390/chemosensors9080212.

(161) Wang, N.; Yang, A.; Fu, Y.; Li, Y.; Yan, F. Functionalized Organic Thin Film Transistors for Biosensing. *Acc. Chem. Res.* **2019**, *52* (2), 277–287. https://doi.org/10.1021/acs.accounts.8b00448.

(162) Burtscher, B.; Diacci, C.; Makhinia, A.; Savvakis, M.; Gabrielsson, E. O.; Veith, L.; Liu, X.; Strakosas, X.; Simon, D. T. Functionalization of PEDOT:PSS for Aptamer-Based Sensing of IL6 Using Organic Electrochemical Transistors. *npj Biosensing* **2024**, *1* (1). https://doi.org/10.1038/s44328-024-00007-w.

(163) Shan, C.; Yang, H.; Han, D.; Zhang, Q.; Ivaska, A.; Niu, L. Electrochemical Determination of NADH and Ethanol Based on Ionic Liquid-Functionalized Graphene. *Biosens. Bioelectron.* **2010**, *25* (6), 1504–1508. https://doi.org/10.1016/j.bios.2009.11.009.

(164) Abdelhamid, H. N.; Khan, M. S.; Wu, H. F. Design, Characterization and Applications of New Ionic Liquid Matrices for Multifunctional Analysis of Biomolecules: A Novel Strategy for Pathogenic Bacteria Biosensing. *Anal. Chim. Acta* **2014**, *823*, 51–60. https://doi.org/10.1016/j.aca.2014.03.026.

(165) Shiddiky, M. J. A.; Torriero, A. A. J. Application of Ionic Liquids in Electrochemical Sensing Systems. *Biosensors and Bioelectronics*. January 15, 2011, pp 1775–1787. https://doi.org/10.1016/j.bios.2010.08.064.

(166) Carda-Broch, S.; Berthod, A.; Armstrong, D. W. Ionic Matrices for Matrix-Assisted Laser Desorption/Ionization Time-of-Flight Detection of DNA Oligomers. *Rapid Communications in Mass Spectrometry* **2003**, *17* (6), 553–560. https://doi.org/10.1002/rcm.931.

(167) Liu, Y.; Shi, L.; Wang, M.; Li, Z.; Liu, H.; Li, J. A Novel Room Temperature Ionic Liquid Sol-Gel Matrix for Amperometric Biosensor Application. *Green Chemistry* **2005**, *7* (9), 655–658. https://doi.org/10.1039/b504689k.

(168) Khodagholy, D.; Curto, V. F.; Fraser, K. J.; Gurfinkel, M.; Byrne, R.; Diamond, D.; Malliaras, G. G.; Benito-Lopez, F.; Owens, R. M. Organic Electrochemical Transistor Incorporating an Ionogel as a Solid State Electrolyte for Lactate Sensing. *J. Mater. Chem.* **2012**, *22* (10), 4440–4443. https://doi.org/10.1039/c2jm15716k.

(169) Bihar, E.; Deng, Y.; Miyake, T.; Saadaoui, M.; Malliaras, G. G.; Rolandi, M. A Disposable Paper Breathalyzer with an Alcohol Sensing Organic Electrochemical Transistor. *Sci. Rep.* **2016**, *6*. https://doi.org/10.1038/srep27582.

(170) Wang, N.; Yang, A.; Fu, Y.; Li, Y.; Yan, F. Functionalized Organic Thin Film Transistors for Biosensing. *Acc. Chem. Res.* **2019**, *52* (2), 277–287. https://doi.org/10.1021/acs.accounts.8b00448.

(171) Koklu, A.; Wustoni, S.; Musteata, V. E.; Ohayon, D.; Moser, M.; McCulloch, I.; Nunes, S. P.; Inal, S. Microfluidic Integrated Organic Electrochemical Transistor with a Nanoporous Membrane for Amyloid-β Detection. *ACS Nano* **2021**, *15* (5), 8130–8141. https://doi.org/10.1021/acsnano.0c09893.

(172) Koklu, A.; Ohayon, D.; Wustoni, S.; Druet, V.; Saleh, A.; Inal, S. Organic Bioelectronic Devices for Metabolite Sensing. *Chemical Reviews*. American Chemical Society February 23, 2022, pp 4581–4635. https://doi.org/10.1021/acs.chemrev.1c00395.

(173) Mckinley, G. H.; Renardy, M. *Wolfgang von Ohnesorge*; 2011.

(174) Jang, D.; Kim, D.; Moon, J. Influence of Fluid Physical Properties on Ink-Jet Printability. *Langmuir* **2009**, *25* (5), 2629–2635. https://doi.org/10.1021/la900059m.

(175) Derby, B. Inkjet Printing of Functional and Structural Materials: Fluid Property Requirements, Feature Stability, and Resolution. *Annu. Rev. Mater. Res.* **2010**, *40*, 395–414. https://doi.org/10.1146/annurev-matsci-070909-104502.

(176) Kamyshny, A.; Magdassi, S. Conductive Nanomaterials for Printed Electronics. *Small*. Wiley-VCH Verlag September 10, 2014, pp 3515–3535. https://doi.org/10.1002/smll.201303000.

(177) Yang, Y.; Chang, S.-C.; Bharathan, J.; Liu, J. *Organic/Polymeric Electroluminescent Devices Processed by Hybrid Ink-Jet Printing*.

(178) Sirringhaus, H.; Kawase, T.; Friend, R. H.; Shimoda, T.; Inbasekaran, M.; Wu, W.; Woo, E. P. High-Resolution Inkjet Printing of All-Polymer Transistor.

(179) Shimoda, T.; Kanbe, S.; Kobayashi, H.; Seki, S.; Kiguchi, H.; Yudasaka, I.; Kimura, M.; Miyashita, S.; Friend, R. H.; Burroughes, J. H.; Towns, C. R. 26.3: Multicolor Pixel Patterning of Light-Emitting Polymers by Ink-Jet Printing. *SID Symposium Digest of Technical Papers* **1999**, *30* (1), 376–379. https://doi.org/10.1889/1.1834036.

(180) Cummins, G.; Desmulliez, M. P. Y. Inkjet Printing of Conductive Materials: A Review. *Circuit World*. 2012, pp 193–213. https://doi.org/10.1108/03056121211280413.

(181) Titkov, A. I.; Bukhanets, O. G.; Gadirov, R. M.; Yukhin, Y. M.; Lyakhov, N. Z. Conductive Inks for Inkjet Printing Based on Composition of Nanoparticles and Organic Silver Salt. *Inorganic Materials: Applied Research* **2015**, *6* (4), 375–381. https://doi.org/10.1134/S2075113315040243.

(182) Buga, C.; C Viana, J. Optimization of Print Quality of Inkjet Printed PEDOT:PSS Patterns. *Flexible and Printed Electronics* **2022**, *7* (4). https://doi.org/10.1088/2058-8585/ac931e.

(183) Kommeren, S.; Coenen, M. J. J.; Eggenhuisen, T. M.; Slaats, T. M. W. L.; Gorter, H.; Groen, P. Combining Solvents and Surfactants for Inkjet Printing PEDOT:PSS on P3HT/PCBM in Organic Solar Cells. *Org. Electron.* **2018**, *61*, 282–288. https://doi.org/10.1016/j.orgel.2018.06.004.

(184) Jun, H. Y.; Kim, S. J.; Choi, C. H. Ink Formulation and Printing Parameters for Inkjet Printing of Two Dimensional Materials: A Mini Review.

Nanomaterials. MDPI December 1, 2021. https://doi.org/10.3390/nano11123441.

(185) Antonopoulou, E.; Harlen, O. G.; Rump, M.; Segers, T.; Walkley, M. A. Effect of Surfactants on Jet Break-up in Drop-on-Demand Inkjet Printing. *Physics of Fluids* **2021**, *33* (7). https://doi.org/10.1063/5.0056803.

(186) Chen, G.; Gu, Y.; Tsang, H.; Hines, D. R.; Das, S. The Effect of Droplet Sizes on Overspray in Aerosol-Jet Printing. *Adv. Eng. Mater.* **2018**, *20* (8). https://doi.org/10.1002/adem.201701084.

(187) Hong, K.; Kim, Y. H.; Kim, S. H.; Xie, W.; Xu, W. D.; Kim, C. H.; Frisbie, C. D. Aerosol Jet Printed, Sub-2 v Complementary Circuits Constructed from P- and N-Type Electrolyte Gated Transistors. *Advanced Materials* **2014**, *26* (41), 7032–7037. https://doi.org/10.1002/adma.201401330.

(188) Yi, H.; Liu, Y.; Cao, H.; Luo, J.; Dong, X.; An, J.; Chua, C. K. Material and Process Integrated Innovations in Aerosol Jet Printing: A Review. *Materials Today*. Elsevier B.V. December 1, 2025, pp 431–458. https://doi.org/10.1016/j.mattod.2025.11.001.

(189) Qin, W.; Li, S.; Wei, S.; Qi, S.; Zhang, W.; Kang, T.; Li, Y. Direct Manufacturing Technology for High-Precision Follow-the-Shape Circuits on Complex, Hard, Curved Surfaces. *Adv. Mater. Technol.* **2023**, *8* (17). https://doi.org/10.1002/admt.202300295.

(190) Zhang, Y.; Zhu, T.; Jiao, J.; Song, S.; Wang, Z.; Wang, Z. Experimental and Numerical Investigation on the Aerosol Micro-Jet 3D Printing of Flexible Electronic Devices. *Materials* **2023**, *16* (22). https://doi.org/10.3390/ma16227099.

(191) Islam, M. S.; Zorman, C. A.; Cao, C. Parametric Optimization of PEDOT:PSS Aerosol Jet Printing for Enhanced Line Morphology in Flexible Electronics. *Adv. Electron. Mater.* **2025**. https://doi.org/10.1002/aelm.202500535.

(192) Tarabella, G.; Vurro, D.; Lai, S.; D'Angelo, P.; Ascari, L.; Iannotta, S. Aerosol Jet Printing of PEDOT:PSS for Large Area Flexible Electronics. *Flexible and Printed Electronics* **2020**, *5* (1). https://doi.org/10.1088/2058-8585/ab61c4.

(193) Singh, A.; Katiyar, M.; Garg, A. Understanding the Formation of PEDOT:PSS Films by Ink-Jet Printing for Organic Solar Cell Applications. *RSC Adv.* **2015**, *5* (96), 78677–78685. https://doi.org/10.1039/c5ra11032g.

(194) Ferraro, J. R. *Introductory Raman Spectroscopy*; Elsevier, 2003.

(195) Kong, M.; Garriga, M.; Reparaz, J. S.; Alonso, M. I. Advanced Optical Characterization of PEDOT:PSS by Combining Spectroscopic Ellipsometry and Raman Scattering. *ACS Omega* **2022**, *7* (43), 39429–39436. https://doi.org/10.1021/acsomega.2c05945.

(196) Mansour, A. E.; Valencia, A. M.; Lungwitz, D.; Wegner, B.; Tanaka, N.; Shoji, Y.; Fukushima, T.; Opitz, A.; Cocchi, C.; Koch, N. Understanding the Evolution of the Raman Spectra of Molecularly P-Doped Poly(3-Hexylthiophene-2,5-Diyl): Signatures of Polarons and Bipolarons. *Physical Chemistry Chemical Physics* **2022**, *24* (5), 3109–3118. https://doi.org/10.1039/d1cp04985b.

(197) Chen, A. X.; Esparza, G. L.; Simon, I.; Dunfield, S. P.; Qie, Y.; Bunch, J. A.; Blau, R.; Lim, A.; Zhang, H.; Brew, S. E.; O'Neill, F. M.; Fenning, D. P.; Lipomi, D. J. Effect of Additives on the Surface Morphology, Energetics, and Contact Resistance of PEDOT:PSS. *ACS Appl. Mater. Interfaces* **2023**, *15* (31), 38143–38153. https://doi.org/10.1021/acsami.3c08341.

(198) Gerrard, D. L.; Graves, P. R.; Louden, D.; Turrell, G. *Practical Raman Spectroscopy*; Springer-Verlag, 1989.

(199) Smith, E.; Dent, G. *Modern Raman Spectroscopy: A Practical Approach*; John Wiley & Sons, 2019.

(200) Tran-Van, F.; Garreau, S.; Louarn, G.; Froyer, G.; Chevrot, C. Fully Undoped and Soluble Oligo(3,4-Ethylenedioxythiophene)s: Spectroscopic Study and Electrochemical Characterization. *J. Mater. Chem.* **2001**, *11* (5), 1378–1382. https://doi.org/10.1039/b100033k.

(201) Yi, Z.; Zhao, Y.; Li, P.; Ho, K.; Blozowski, N.; Walker, G.; Jaffer, S.; Tjong, J.; Sain, M.; Lu, Z. The Effect of Tannic Acids on the Electrical Conductivity of PEDOT:PSS Films. *Appl. Surf. Sci.* **2018**, *448*, 583–588. https://doi.org/10.1016/j.apsusc.2018.04.168.

(202) Garreau, S.; Louarn, G.; Buisson, J. P.; Froyer, G.; Lefrant, S. In Situ Spectroelectrochemical Raman Studies of Poly(3,4-Ethylenedioxythiophene)

(PEDT). *Macromolecules* **1999**, *32* (20), 6807–6812. https://doi.org/10.1021/ma9905674.

(203) Chen, A. X.; Esparza, G. L.; Simon, I.; Dunfield, S. P.; Qie, Y.; Bunch, J. A.; Blau, R.; Lim, A.; Zhang, H.; Brew, S. E.; O'Neill, F. M.; Fenning, D. P.; Lipomi, D. J. Effect of Additives on the Surface Morphology, Energetics, and Contact Resistance of PEDOT:PSS. *ACS Appl. Mater. Interfaces* **2023**, *15* (31), 38143–38153. https://doi.org/10.1021/acsami.3c08341.

(204) Snaith, H. J.; Kenrick, H.; Chiesa, M.; Friend, R. H. Morphological and Electronic Consequences of Modifications to the Polymer Anode "PEDOT:PSS." *Polymer (Guildf).* **2005**, *46* (8), 2573–2578. https://doi.org/10.1016/j.polymer.2005.01.077.

(205) Donoval, M.; Micjan, M.; Novota, M.; Nevrela, J.; Kovacova, S.; Pavuk, M.; Juhasz, P.; Jagelka, M.; Kovac, J.; Jakabovic, J.; Cigan, M.; Weis, M. Relation between Secondary Doping and Phase Separation in PEDOT:PSS Films. *Appl. Surf. Sci.* **2017**, *395*, 86–91. https://doi.org/10.1016/j.apsusc.2016.05.076.

(206) Braga, P.; Ricci, D. *Atomic Force Microscopy in Biomedical Research*; 2011. www.springer.com/series/7651.

(207) Hutter, J. L.; Bechhoefer, J. Calibration of Atomic-Force Microscope Tips. *Review of Scientific Instruments* **1993**, *64* (7), 1868–1873. https://doi.org/10.1063/1.1143970.

(208) Yu, T. Y. T.; Chou, T. Y.; Naenen, V.; Zhang, B.; Baysal, H. E.; Bulut, B.; Rosenthal, M.; Molina-Lopez, F. Unleashing the Potential of Raman Spectroscopy to Estimate PEDOT:PSS Doping Level and Crystalline Morphology. *Advanced Science* **2025**. https://doi.org/10.1002/advs.202513726.

(209) Wada, Y.; Enokida, I.; Yamamoto, J.; Furukawa, Y. Raman Imaging of Carrier Distribution in the Channel of an Ionic Liquid-Gated Transistor Fabricated with Regioregular Poly(3-Hexylthiophene). *Spectrochim. Acta A Mol. Biomol. Spectrosc.* **2018**, *197*, 166–169. https://doi.org/10.1016/j.saa.2018.01.043.

(210) Romero, M.; Mombrú, D.; Pignanelli, F.; Faccio, R.; Mombrú, Á. W. Mixed Ionic-Electronic Transport for PEDOT:PSS-Based Zero-Gated Organic Electrochemical Transistors Using Impedance Spectroscopy and Micro-Raman Imaging. *ACS Appl. Electron. Mater.* **2023**, *5* (9), 4863–4874. https://doi.org/10.1021/acsaelm.3c00655.

(211) Sakamoto, S.; Okumura, M.; Zhao, Z.; Furukawa, Y. Raman Spectral Changes of PEDOT-PSS in Polymer Light-Emitting Diodes upon Operation. *Chem. Phys. Lett.* **2005**, *412* (4–6), 395–398. https://doi.org/10.1016/j.cplett.2005.07.040.

(212) Segantini, M.; Ballesio, A.; Palmara, G.; Zaccagnini, P.; Frascella, F.; Garzone, G.; Marasso, S. L.; Cocuzza, M.; Parmeggiani, M. Investigation and Modeling of the Electrical Bias Stress in Electrolyte-Gated Organic Transistors. *Adv. Electron. Mater.* **2022**, *8* (7). https://doi.org/10.1002/aelm.202101332.

(213) Chang, S. H.; Chiang, C. H.; Kao, F. S.; Tien, C. L.; Wu, C. G. Unraveling the Enhanced Electrical Conductivity of PEDOT:PSS Thin Films for ITO-Free Organic Photovoltaics. *IEEE Photonics J.* **2014**, *6* (4). https://doi.org/10.1109/JPHOT.2014.2331254.

(214) Volkov, A. V.; Wijeratne, K.; Mitraka, E.; Ail, U.; Zhao, D.; Tybrandt, K.; Andreasen, J. W.; Berggren, M.; Crispin, X.; Zozoulenko, I. V. Understanding the Capacitance of PEDOT:PSS. *Adv. Funct. Mater.* **2017**, *27* (28). https://doi.org/10.1002/adfm.201700329.

(215) Rivnay, J.; Inal, S.; Salleo, A.; Owens, R. M.; Berggren, M.; Malliaras, G. G. Organic Electrochemical Transistors. *Nature Reviews Materials*. Nature Publishing Group January 16, 2018. https://doi.org/10.1038/natrevmats.2017.86.

(216) Tan, E.; Pappa, A. M.; Pitsalidis, C.; Nightingale, J.; Wood, S.; Castro, F. A.; Owens, R. M.; Kim, J. S. A Highly Sensitive Molecular Structural Probe Applied to in Situ Biosensing of Metabolites Using PEDOT:PSS. *Biotechnol. Bioeng.* **2020**, *117* (1), 291–299. https://doi.org/10.1002/bit.27187.

(217) Garreau, S.; Louarn, G.; Buisson, J. P.; Froyer, G.; Lefrant, S. In Situ Spectroelectrochemical Raman Studies of Poly(3,4-Ethylenedioxythiophene) (PEDT). *Macromolecules* **1999**, *32* (20), 6807–6812. https://doi.org/10.1021/ma9905674.

(218) Weissbach, A.; Cucchi, M.; Tseng, H.; Leo, K.; Kleemann, H. Unraveling the Electrochemical Electrode Coupling in Integrated Organic Electrochemical Transistors. *Adv. Funct. Mater.* **2023**, *33* (46). https://doi.org/10.1002/adfm.202302205.

(219) Tamburri, E.; Orlanducci, S.; Toschi, F.; Terranova, M. L.; Passeri, D. Growth Mechanisms, Morphology, and Electroactivity of PEDOT Layers

Produced by Electrochemical Routes in Aqueous Medium. *Synth. Met.* **2009**, *159* (5–6), 406–414. https://doi.org/10.1016/j.synthmet.2008.10.014.

(220) Tan, E.; Pappa, A. M.; Pitsalidis, C.; Nightingale, J.; Wood, S.; Castro, F. A.; Owens, R. M.; Kim, J. S. A Highly Sensitive Molecular Structural Probe Applied to in Situ Biosensing of Metabolites Using PEDOT:PSS. *Biotechnol. Bioeng.* **2020**, *117* (1), 291–299. https://doi.org/10.1002/bit.27187.

(221) Xu, H.; Zhao, X.; Yang, G.; Ji, X.; Zhang, X.; Li, L.; Wu, B.; Ouyang, X.; Ni, Y.; Chen, L.; Hu, H. C. Modification of PEDOT:PSS towards High-Efficiency OLED Electrode via Synergistic Effect of Carboxy and Phenol Groups from Biomass Derivatives. *Chemical Engineering Journal* **2022**, *430*. https://doi.org/10.1016/j.cej.2021.133014.

(222) Mitraka, E.; Jafari, M. J.; Vagin, M.; Liu, X.; Fahlman, M.; Ederth, T.; Berggren, M.; Jonsson, M. P.; Crispin, X. Oxygen-Induced Doping on Reduced PEDOT. *J. Mater. Chem. A Mater.* **2017**, *5* (9), 4404–4412. https://doi.org/10.1039/c6ta10521a.

(223) Kim, S.; Kim, H. S.; Park, Y. D. Doped PEDOT:PSS Electrodes, Patterned through Wettability Control, and Their Effects on the Electrical Properties of Polymer Thin Film Transistors. *Org. Electron.* **2016**, *30*, 296–301. https://doi.org/10.1016/j.orgel.2016.01.001.

(224) Sánchez Vergara, M. E.; Jimenez Correa, O.; Ballinas-Indilí, R.; Cosme, I.; Álvarez Bada, J. R.; Álvarez-Toledano, C. Innovative Application of Salophen Derivatives in Organic Electronics as a Composite Film with a Poly(3,4-Ethylenedioxythiophene)-Poly(Styrenesulfonate) Matrix. *Polymers (Basel).* **2024**, *16* (18). https://doi.org/10.3390/polym16182622.

(225) Ouyang, J.; Chu, C. W.; Chen, F. C.; Xu, Q.; Yang, Y. High-Conductivity Poly(3,4-Ethylenedioxythiophene):Poly(Styrene Sulfonate) Film and Its Application in Polymer Optoelectronic Devices. *Adv. Funct. Mater.* **2005**, *15* (2), 203–208. https://doi.org/10.1002/adfm.200400016.

(226) Bontapalle, S.; Varughese, S. Understanding the Mechanism of Ageing and a Method to Improve the Ageing Resistance of Conducting PEDOT:PSS Films. *Polym. Degrad. Stab.* **2020**, *171*. https://doi.org/10.1016/j.polymdegradstab.2019.109025.

(227) Suchand Sangeeth, C. S.; Jaiswal, M.; Menon, R. Correlation of Morphology and Charge Transport in Poly(3,4- Ethylenedioxythiophene)-

Polystyrenesulfonic Acid (PEDOT-PSS) Films. *Journal of Physics Condensed Matter* **2009**, *21* (7). https://doi.org/10.1088/0953-8984/21/7/072101.

(228) Wei, Q.; Mukaida, M.; Naitoh, Y.; Ishida, T. Morphological Change and Mobility Enhancement in PEDOT:PSS by Adding Co-Solvents. *Advanced Materials* **2013**, *25* (20), 2831–2836. https://doi.org/10.1002/adma.201205158.

(229) Garnett, E.; Ginley, D. *ELECTRICAL AND MORPHOLOGICAL PROPERTIES OF INKJET PRINTED PEDOT/PSS FILMS*. http://www.scied.science.doe.gov.

(230) D'Angelo, P.; Tarabella, G.; Romeo, A.; Marasso, S. L.; Verna, A.; Cocuzza, M.; Peruzzi, C.; Vurro, D.; Iannotta, S. PEDOT:PSS Morphostructure and Ion-to-Electron Transduction and Amplification Mechanisms in Organic Electrochemical Transistors. *Materials* **2018**, *12* (1). https://doi.org/10.3390/ma12010009.

(231) Scott, W. W.; Bhushan, B. Use of Phase Imaging in Atomic Force Microscopy for Measurement of Viscoelastic Contrast in Polymer Nanocomposites and Molecularly Thick Lubricant Films. *Ultramicroscopy* **2003**, *97* (1–4), 151–169. https://doi.org/10.1016/S0304-3991(03)00040-8.

(232) Magonov, S. N.; Elings, V.; Whangbo, M.-H. Phase Imaging and Stiffness in Tapping-Mode Atomic Force Microscopy. *Surface Science Letters* **1997**.

(233) Stocker, W.; Beckmann, rg; Stadler, R.; Rabe, rgen P. *Surface Reconstruction of the Lamellar Morphology in a Symmetric Poly(Styrene-Block-Butadiene-Block-Methyl Methacrylate) Triblock Copolymer: A Tapping Mode Scanning Force Microscope Study*; 1996.

(234) Torre, B.; Bertoni, G.; Fragouli, D.; Falqui, A.; Salerno, M.; Diaspro, A.; Cingolani, R.; Athanassiou, A. Magnetic Force Microscopy and Energy Loss Imaging of Superparamagnetic Iron Oxide Nanoparticles. *Sci. Rep.* **2011**, *1*. https://doi.org/10.1038/srep00202.

(235) Raghavan, D.; Gu, X.; Nguyen, T.; VanLandingham, M.; Karim, A. Mapping Polymer Heterogeneity Using Atomic Force Microscopy Phase Imaging and Nanoscale Indentation. *Macromolecules* **2000**, *33* (7), 2573–2583. https://doi.org/10.1021/ma991206r.

(236) Martínez, N. F.; García, R. Measuring Phase Shifts and Energy Dissipation with Amplitude Modulation Atomic Force Microscopy. *Nanotechnology* **2006**, *17* (7). https://doi.org/10.1088/0957-4484/17/7/S11.

(237) Bar, G.; Thomann, Y.; Whangbo, M.-H. *Characterization of the Morphologies and Nanostructures of Blends of Poly(Styrene)-Block-Poly(Ethene-Co-but-1-Ene)-Block-Poly(Styrene) with Isotactic and Atactic Polypropylenes by Tapping-Mode Atomic Force Microscopy*; 1998.

(238) Sauer, B. B.; Mclean, R. S.; Thomas, R. R. *Tapping Mode AFM Studies of Nano-Phases on Fluorine-Containing Polyester Coatings and Octadecyltrichlorosilane Monolayers*; 1998.

(239) Magonov, S. N.; Elings, V.; Papkov, V. S. *AFM Study of Thermotropic Structural Transitions in Poly(Diethylsiloxane)*; 1997; Vol. 38.

(240) Gueye, M. N.; Carella, A.; Faure-Vincent, J.; Demadrille, R.; Simonato, J. P. Progress in Understanding Structure and Transport Properties of PEDOT-Based Materials: A Critical Review. *Progress in Materials Science*. Elsevier Ltd February 1, 2020. https://doi.org/10.1016/j.pmatsci.2019.100616.

(241) Sinawang, P. D.; Rai, V.; Ionescu, R. E.; Marks, R. S. Electrochemical Lateral Flow Immunosensor for Detection and Quantification of Dengue NS1 Protein. *Biosens. Bioelectron.* **2016**, *77*, 400–408. https://doi.org/10.1016/j.bios.2015.09.048.

(242) Ying, X.; Fu, W.; Zhu, L.; Sun, T.; Qi Min and Zhou, L.; Wang, Y.; Wang, J.; Su, B.; Zhang, J. Electrochemical Lateral Flow Immunoassay with Built-In Electrodes for Ultrasensitive and Wireless Detection of Inflammatory Biomarkers. *Anal. Chem.* **2024**, *96* (26), 10630–10638. https://doi.org/10.1021/acs.analchem.4c01224.

(243) Abarintos, V.; Piper, A.; Merkoci, A. Electrochemical Lateral Flow Assays: A New Frontier for Rapid and Quantitative Biosensing. *Current Opinion in Electrochemistry*. Elsevier B.V. December 1, 2025. https://doi.org/10.1016/j.coelec.2025.101750.

(244) Siegel, A. C.; Phillips, S. T.; Dickey, M. D.; Lu, N.; Suo, Z.; Whitesides, G. M. Foldable Printed Circuit Boards on Paper Substrates. *Adv. Funct. Mater.* **2010**, *20* (1), 28–35. https://doi.org/10.1002/adfm.200901363.

(245) Cruz, S. M. F.; Rocha, L. A.; Viana, J. C. Printing Technologies on Flexible Substrates for Printed Electronics. In *Flexible Electronics*; InTech, 2018. https://doi.org/10.5772/intechopen.76161.

(246) Pecunia, V.; Petti, L.; Andrews, J. B.; Ollearo, R.; Gelinck, G. H.; Nasrollahi, B.; Jailani, J. M.; Li, N.; Kim, J. H.; Ng, T. N.; Feng, H.; Chen, Z.; Guo, Y.; Shen, L.; Lhuillier, E.; Kuo, L.; Sangwan, V. K.; Hersam, M. C.; Fraboni, B.; Basiricò, L.; Ciavatti, A.; Wu, H.; Niu, G.; Tang, J.; Yang, G.; Kim, D.; Dremann, D.; Jurchescu, O. D.; Bederak, D.; Shulga, A. G.; Costa, P.; Perinka, N.; Lanceros-Mendez, S.; Chortos, A.; Khuje, S.; Yu, J.; Ren, S.; Mascia, A.; Concas, M.; Cosseddu, P.; Young, R. J.; Yokota, T.; Somoya, T.; Jeon, S. J.; Zhao, N.; Li, Y.; Shukla, D.; Wu, S.; Zhu, Y.; Takei, K.; Huang, Y.; Spiece, J.; Gehring, P.; Persaud, K.; Llobet, E.; Krik, S.; Vasquez, S.; Costa Angeli, M. A.; Lugli, P.; Fabbri, B.; Spagnoli, E.; Rossi, A.; Occhipinti, L. G.; Tang, C.; Yi, W.; Ravenscroft, D.; Kandukuri, T. R.; Abideen, Z. U.; Azimi, Z.; Tricoli, A.; Rivadeneyra, A.; Rojas, S.; Gaiardo, A.; Valt, M.; Galstyan, V.; Zappa, D.; Comini, E.; Noël, V.; Mattana, G.; Piro, B.; Strand, E.; Bihar, E.; Whiting, G. L.; Shkodra, B.; Petrelli, M.; Moro, G.; Raucci, A.; Miglione, A.; Cinti, S.; Casson, A. J.; Wang, Z.; Bird, D.; Batchelor, J. C.; Xing, L.; Johnson, L. S. J.; Alwattar, A. A.; Kyndiah, A.; Viola, F. A.; Caironi, M.; Albarghouthi, F. M.; Smith, B. N.; Franklin, A. D.; Pal, A.; Banerjee, K.; Johnson, Z. T.; Claussen, J. C.; Moudgil, A.; Leong, W. L. Roadmap on Printable Electronic Materials for Next-Generation Sensors. *Nano Futures*. Institute of Physics September 1, 2024. https://doi.org/10.1088/2399-1984/ad36ff.

(247) Bihar, E.; Corzo, D.; Hidalgo, T. C.; Rosas-Villalva, D.; Salama, K. N.; Inal, S.; Baran, D. Fully Inkjet-Printed, Ultrathin and Conformable Organic Photovoltaics as Power Source Based on Cross-Linked PEDOT:PSS Electrodes. *Adv. Mater. Technol.* **2020**, *5* (8). https://doi.org/10.1002/admt.202000226.

(248) Quero, R. F.; Fracassi da Silva, J. A.; de Jesus, D. P. How Is 3D Printing Revolutionizing the Design and Fabrication of Analytical Microfluidic Devices? *Brazilian Journal of Analytical Chemistry*. Visao Fokka Communication Agency 2025, pp 14–17. https://doi.org/10.30744/brjac.2179-3425.letter.N46.

(249) Abera, B. D.; Falco, A.; Ibba, P.; Cantarella, G.; Petti, L.; Lugli, P. Development of Flexible Dispense-Printed Electrochemical Immunosensor for Aflatoxin M1 Detection in Milk. *Sensors (Switzerland)* **2019**, *19* (18). https://doi.org/10.3390/s19183912.

(250) Ahmad, M.; Costa Angeli, M. A.; Ibba, P.; Vasquez, S.; Shkodra, B.; Lugli, P.; Petti, L. Paper-Based Printed Antenna: Investigation of Process-Induced and Climatic-Induced Performance Variability. *Adv. Eng. Mater.* **2023**, *25* (16). https://doi.org/10.1002/adem.202201703.

(251) Vasquez, S.; Ibba, P.; Altana, A.; Costa Angeli, M. A.; Rivadeneyra, A.; Lugli, P.; Petti, L. Paper-Based Impedimetric Sensor for on-Plant Humidity and Transpiration Monitoring. In *2023 IEEE Conference on AgriFood Electronics, CAFE 2023 - Proceedings*; Institute of Electrical and Electronics Engineers Inc., 2023; pp 182–186. https://doi.org/10.1109/CAFE58535.2023.10291980.

(252) Vasquez, S.; Shkodra, B.; Rivadeneyra, A.; Angeli, M. A. C.; Altana, A.; Allara, C.; Ibba, P.; Lugli, P.; Petti, L. Fully Printed Low-Cost Ammonia Gas Sensor on Paper Substrate. In *Proceedings of IEEE Sensors*; Institute of Electrical and Electronics Engineers Inc., 2024. https://doi.org/10.1109/SENSORS60989.2024.10785124.

(253) Cicolini, M.; Solgi, A.; Vigna, L.; Ballesio, A.; Marasso, S.; Cocuzza, M.; Kleemann, H.; Frascella, F.; Napione, L. A Printable OECT for Simple Integration in Nitrocellulose-Based Assays. *ACS Sens.* **2025**. https://doi.org/10.1021/acssensors.5c01893.

(254) Tang, K.; Miao, W.; Guo, S. Crosslinked PEDOT:PSS Organic Electrochemical Transistors on Interdigitated Electrodes with Improved Stability. *ACS Appl. Polym. Mater.* **2021**, *3* (3), 1436–1444. https://doi.org/10.1021/acsapm.0c01292.

(255) Keene, S. T.; Gatecliff, L. W.; Bidinger, S. L.; Moser, M.; McCulloch, I.; Malliaras, G. G. Stable Operating Windows for Polythiophene Organic Electrochemical Transistors. *MRS Commun.* **2024**, *14* (2), 158–166. https://doi.org/10.1557/s43579-023-00511-6.

(256) Latif, S.; Jahangeer, M.; Maknoon Razia, D.; Ashiq, M.; Ghaffar, A.; Akram, M.; El Allam, A.; Bouyahya, A.; Garipova, L.; Ali Shariati, M.; Thiruvengadam, M.; Azam Ansari, M. Dopamine in Parkinson's Disease. *Clinica Chimica Acta* **2021**, *522*, 114–126. https://doi.org/https://doi.org/10.1016/j.cca.2021.08.009.

(257) Meiser, J.; Weindl, D.; Hiller, K. *Complexity of Dopamine Metabolism*; 2013; Vol. 11. http://www.biosignaling.com/content/11/1/34.

(258) Tang, H.; Lin, P.; Chan, H. L. W.; Yan, F. Highly Sensitive Dopamine Biosensors Based on Organic Electrochemical Transistors. *Biosens. Bioelectron.* **2011**, *26* (11), 4559–4563. https://doi.org/10.1016/j.bios.2011.05.025.

(259) Limit of Detection. **2025**. https://doi.org/doi:10.1351/goldbook.L03540.

(260) Gualandi, I.; Tonelli, D.; Mariani, F.; Scavetta, E.; Marzocchi, M.; Fraboni, B. Selective Detection of Dopamine with an All PEDOT:PSS Organic Electrochemical Transistor. *Sci. Rep.* **2016**, *6*. https://doi.org/10.1038/srep35419.

(261) Barra, M.; Tomaiuolo, G.; Villella, V. R.; Esposito, S.; Liboà, A.; D'Angelo, P.; Marasso, S. L.; Cocuzza, M.; Bertana, V.; Camilli, E.; Preziosi, V. Organic Electrochemical Transistor Immuno-Sensors for Spike Protein Early Detection. *Biosensors (Basel).* **2023**, *13* (7). https://doi.org/10.3390/bios13070739.

(262) Ho, P. Y.; Ditzer, O.; Solgi, A.; Zhang, H.; Thümmler, R.; Al-Hussein, M.; Kleemann, H.; Sun, N.; Lissel, F. S. -C. Boosting OECT Performance with PEGylated Gold Nanoparticles in Hydrophobic Channels. *Adv. Funct. Mater.* **2024**. https://doi.org/10.1002/adfm.202412559.

(263) Kim, D. J.; Lee, N. E.; Park, J. S.; Park, I. J.; Kim, J. G.; Cho, H. J. Organic Electrochemical Transistor Based Immunosensor for Prostate Specific Antigen (PSA) Detection Using Gold Nanoparticles for Signal Amplification. *Biosens. Bioelectron.* **2010**, *25* (11), 2477–2482. https://doi.org/10.1016/j.bios.2010.04.013.

(264) Rodríguez, C. F.; Andrade-Pérez, V.; Vargas, M. C.; Mantilla-Orozco, A.; Osma, J. F.; Reyes, L. H.; Cruz, J. C. Breaking the Clean Room Barrier: Exploring Low-Cost Alternatives for Microfluidic Devices. *Frontiers in Bioengineering and Biotechnology*. Frontiers Media S.A. 2023. https://doi.org/10.3389/fbioe.2023.1176557.

(265) Bhamla, M. S.; Benson, B.; Chai, C.; Katsikis, G.; Johri, A.; Prakash, M. Hand-Powered Ultralow-Cost Paper Centrifuge. *Nat. Biomed. Eng.* **2017**, *1* (1). https://doi.org/10.1038/s41551-016-0009.

(266) Parolo, C.; Sena-Torralba, A.; Bergua, J. F.; Calucho, E.; Fuentes-Chust, C.; Hu, L.; Rivas, L.; Álvarez-Diduk, R.; Nguyen, E. P.; Cinti, S.; Quesada-González, D.; Merkoçi, A. Tutorial: Design and Fabrication of Nanoparticle-Based Lateral-Flow Immunoassays. *Nature Protocols*. Nature Research

December 1, 2020, pp 3788–3816. https://doi.org/10.1038/s41596-020-0357-x.

(267) Rivnay, J.; Owens, R. M.; Malliaras, G. G. The Rise of Organic Bioelectronics. *Chemistry of Materials*. January 14, 2014, pp 679–685. https://doi.org/10.1021/cm4022003.

(268) Zeglio, E.; Inganäs, O. Active Materials for Organic Electrochemical Transistors. *Advanced Materials*. Wiley-VCH Verlag November 2, 2018. https://doi.org/10.1002/adma.201800941.

(269) Welton, T. Ionic Liquids: A Brief History. *Biophysical Reviews*. Springer Verlag June 1, 2018, pp 691–706. https://doi.org/10.1007/s12551-018-0419-2.

(270) Bai, L.; Elósegui, C. G.; Li, W.; Yu, P.; Fei, J.; Mao, L. Biological Applications of Organic Electrochemical Transistors: Electrochemical Biosensors and Electrophysiology Recording. *Frontiers in Chemistry*. Frontiers Media S.A. 2019. https://doi.org/10.3389/fchem.2019.00313.

(271) Fu, Y.; Wang, N.; Yang, A.; Law, H. K. wai; Li, L.; Yan, F. Highly Sensitive Detection of Protein Biomarkers with Organic Electrochemical Transistors. *Advanced Materials* **2017**, *29* (41). https://doi.org/10.1002/adma.201703787.

(272) Agarwala, S.; Goh, G. L.; Yeong, W. Y. Optimizing Aerosol Jet Printing Process of Silver Ink for Printed Electronics. In *IOP Conference Series: Materials Science and Engineering*; Institute of Physics Publishing, 2017; Vol. 191. https://doi.org/10.1088/1757-899X/191/1/012027.